Abstract

Targeted Nucleic Acid Delivery to the Endothelium

Melanie Lynn Reschke Horwitz

2022

The human endothelium extends throughout nearly all tissues in the body, and has an estimated total surface area of up to seven thousand square meters [1]. This expansive monolayer of endothelial cells (ECs) serves as the interface between materials circulating in the bloodstream and the internal tissues of the body. Even in its quiescent state, the endothelium is actively signaling and reacting in order to support the basic functions of the vascular system – transporting oxygen, nutrients, and waste. A closer look reveals that the cells that make up this endothelial lining are diverse in their phenotypes and functions, dependent on the organ or tissue in which they reside. When activated under inflammatory conditions or in other disease states, endothelial cells further differentiate themselves through expression of surface antigens. Being a large, easily accessible surface that interfaces with almost all other tissues in the body, and consisting of distinctly identifiable subcategories as well as some universal characteristics, the endothelium is an attractive therapeutic target. Of particular interest in this dissertation is applying gene therapies to treat or prevent inflammation.

We describe a polymeric delivery system for nucleic acids that can be modulated by exchanging polymer end-groups and conjugating cell surface targeting molecules to the delivery vehicle. We show that conjugating EC targeting antibodies to the surface of a cationic poly(amine-co-ester) (PACE) nucleic acid delivery vehicle enhances its transfection efficiency in cultured human ECs. This can enable delivery of gene therapies to ECs, either *in vitro* as cellular components of an engineered vascular graft, *ex vivo* in donated human organs for transplantation, or for targeting the endothelium *in vivo*. In the work presented here we apply the EC-targeted polymeric delivery vehicle to deliver siRNA against IL-15, a cytokine

involved the activation of T cells during acute inflammation.

Our work with transplant-declined human organs motivated the development of a new digital pathology tool for color-based quantification of histologic specimens, which we have applied to quantify vascular assembly in engineered grafts as well as vascular pathologies in human and animal tissue samples. We demonstrate the benefits of an automated program for color-based detection of pathological features in histologic specimens, in particular in a setting in which large numbers of images are generated.

We propose further investigations into the antibody-targeted PACE polyplex delivery platform including a broader exploration of targeting in different cell types *in vitro* and *in vivo*. The work described in this dissertation aims to advance the therapeutic potential of targeted nanocarriers for treating pathologies in the endothelium.

Targeted Nucleic Acid Delivery to the Endothelium

A Dissertation
Presented to the Faculty of the Graduate School
of
Yale University
in Candidacy for the Degree of
Doctor of Philosophy

by
Melanie Lynn Reschke Horwitz

Dissertation Director: W. Mark Saltzman

May 2022

© 2022 by Melanie Lynn Reschke Horwitz

All rights reserved.

Contents

List of Figures

List of Tables

Acknowledgments

I could not have reached this milestone without the immense support I've received from so many people in my life over the past six years.

I want to thank my advisor, Dr. W. Mark Saltzman. I'm so grateful for your mentorship and support throughout my Ph.D. work. With your guidance, navigating the challenges that have arisen in my research has made me a better scientist. I also want to thank my thesis committee members, Dr. Karla Neugebauer and Dr. Anthony Koleske. I always came away from our meetings with new ideas and renewed motiviation. You really helped me focus and chart my path forward.

I have been fortunate to collaborate with amazing and inspiring scientists while here at Yale. Dr. Jordan Pober, Dr. Gregory Tietjen, and Dr. William Chang, the feedback and advice you have given me over the years has been invaluable for my progress on my research projects as well as for helping me develop a deeper understanding of the field. My more collaborative projects have also been some of my favorite projects, in large part due to the people who I have had the opportunity to work closely with, including Jenna DiRito, Tania Baltazar, Douglas Wu, Jon Merola, Claire Albert, Laura Bracaglia, Alexandra Piotrowski-Daspit, Hee Won Suh, Alexandra Suberi, and Taras Lysyy. Thank you also to Gwendolyn Davis-Arrington for always helping me obtain cells and tissues for my experiments over the course of many years.

To all members of the Saltzman Lab who I have worked alongside - Gina Buzzelli, Fan Yang, Claire Albert, Laura Bracaglia, Teresa Lee, Alexandra Piotrowski-Daspit, Jinal

Pothupitiya, Owen Richfield, Kwangsoo Shin, Hee Won Suh, Yazhe Wang, Emily Deschenes, Julian Grundler, Alex Josowitz, Minsoo Khang, Jungsoo Chang, Anna Lynn, Elias Quijano, Eric Song, Lexi Suberi, Ju Hyun Lee, Chad Binns, David Eaton, Madalina Ene, Zhaozhong Jiang, Tushar Agarwal, Jenny Cui, Molly Grun, Yuhang Jiang, Amy Kauffman, Chun-Yu Lin, Hanna Mandl, Zoe Moscato, Kay Nakazawa, Adele Ricciardi, Young-Eun Seo, Yongheng Wang and Douglas Wu - I couldn't ask for a better group of people to work with. A special thank you to Deanna Lomax, I'm always happy to see you and have an opportunity to take a break from the day to chat and catch up. I have had the opportunity to work with several bright and motivated undergraduate students - Natalie Plebanek, Victoria Vera, and Mikayla Labissiere. Thank you for helping motivate me to become a better researcher and mentor.

I am so grateful for my cohort of fellow MB&B classmates and the supportive community that we have - its been amazing to see what we have all accomplished since our first year! In addition to coursework and research, I've learned so much from my peers and colleagues through various organizations - Business of Biotech, Science in the News, Flipped Science Fair, and more - it's inspiring to see the energy my classmates and colleagues bring to these organizations.

I would not be here without important mentors that helped me along during the earliest days of my career as a scientist: my professors at Macalester College including my advisors Dr. Kathryn Splan and Dr. Lin Aanonsen, my P.I. at Weill Cornell, Dr. Anthony Sauve, and the incredible leadership and research team at EpiBone including Dr. Sarindr Bhumiratana, Dr. Nina Tandon, Dr. Mike Lamprecht, and Dr. Olivia Beane.

My friends and family have been there to support me throughout my Ph.D. I am so lucky to have lifelong relationships with wonderful friends new and old, going all the way back to grade school. All of my KBT, 'cooler reunion', Macalester, NYC, and Madison friends. I cannot thank you each enough for being my friend through so many years, with many more to come. When things seem overwhelming, you help me return to what is most important in life.

Thank you to my parents, Jill and Wayne Reschke, for helping me grow into the person I am today. I cannot express how grateful I am for all that you have done and continue to do to support me. Paul, Kevin, Jenna, and Lilu, I look up to all of you so much. The times when we've had an opportunity to all get together have been some of the most restorative experiences that have kept me going over the past several years. Thank you to Sherri and Michael Horwitz for welcoming me into your family. I have felt so at home with you and Alec and Christina and the whole family. Thank you to all of my cousins, aunts, uncles, and grandparents - it is truly incredible to have so many people in my life who will always share in my joy and support me through my challenges. I'd also like to honor and remember loved ones who we have lost during the past 6 years. Thank you for your endless love and support.

More than anything I am so grateful to have an amazing partner in my life, Jesse Horwitz. You've always believed in me and all that I could accomplish. There were more than a few occasions during my Ph.D. where you provided the spark that kept me going or brought me back into focus - I could not have done this without your support.

Chapter 1

Introduction and Background

1.1 The Vascular Endothelium as a Therapeutic Target

1.1.1 Homeostatic Functions and Properties of the Endothelium

The endothelium lines the luminal surface of vessels throughout the vascular system and has an active and essential role in its functioning. The primary functions of the vascular system are to deliver nutrients and oxygen to tissue throughout the body, clear cellular and metabolic waste products, and to participate in immune surveillance, which is discussed further in Section 1.1.2 [2, 3]. The vascular system is not uniform, but rather is made up of vessels of varying sizes and cellular compositions that reflect their function [4, 5].

Throughout this branching vasculature, the endothelium lining the lumen of all vessels is comprised of a single layer of endothelial cells (ECs). ECs carry out the functions of the circulatory system at a cellular and molecular level. Even when the endothelium is considered to be at rest, ECs are actively engaged in maintaining this quiescent state [6, 7]. Anti-coagulating factors produced and regulated by ECs maintain blood fluidity [8, 9]. ECs also regulate blood flow by producing vasodilators that act on smooth muscle cells [2] and control vessel wall permeability [6, 10].

In addition to these universal EC functions, organ-specific ECs carry out distinct functions. Just as the vessels comprising the vascular system are varied in structure and function, so too are the endothelial cells lining its walls [5, 11]. Importantly, ECs are the point of exchange between materials in the bloodstream and the extravascular tissues. This contributes to the unique EC phenotypes seen in different parts of the body; different organs necessitate different degrees or types of exchange with the circulatory system. For example, the brain endothelium forms the blood brain barrier (BBB) where ECs express tight junctions (**Figure 1.1A**). Materials passing across the endothelium must be selectively transported through the ECs rather than passing through gaps or fenestrations. Conversely, in tissues where greater exchange across the endothelium is needed, there are spaces between endothelial cells through which macromolecules can pass (**Figure 1.1B-C**) [6]. The heterogeneity in EC phenotypes throughout the circulatory system has implications for the feasibility of using functionalized nanocarriers to actively target drug or nucleic acid delivery to the endothelium [12]; targeting is discussed further in Section 1.3.

The human endothelium can be studied *in vitro* and in animal models by isolating ECs from human tissues. Attention must be paid to the tissue source, as ECs from different organs present unique phenotypes and protein expression profiles, and form microvasculature in different patterns [13]. Furthermore, isolated ECs may not maintain these properties once cultured *in vitro*. Throughout this dissertation we use primary human umbilical vein endothelial cells (HUVEC) as an *in vitro* endothelium model.

1.1.2 Role of Endothelial Cells in Immune Surveillance

Along with transporting nutrients and waste, two of the most critical roles of endothelial cells are to maintain a state of quiescence under homeostatic conditions, and to recruit and activate leukocytes under acute inflammation. ECs actively maintain a quiescent state by sequestering P-selectin, which helps tether leukocytes to the EC surface, in Weibel-Palade

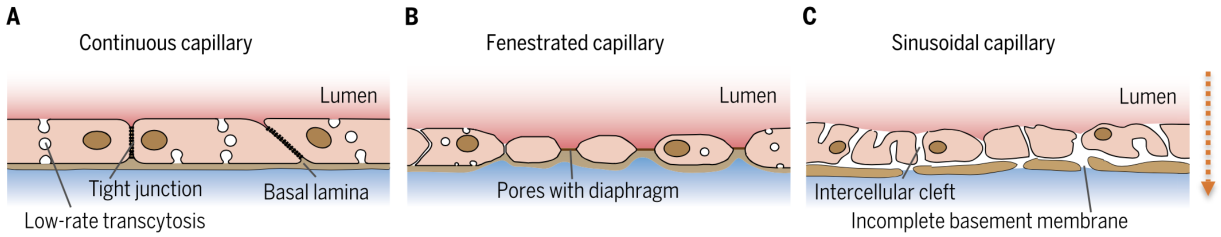

Figure 1.1: Heterogeneity of capillary endothelium. From Augustin et al., 2017. [11]

bodies and suppressing expression of other adhesion molecules such as E-selectin and L-selectin, which have similar roles in binding leukocytes [2]. Upon cytokine stimulation of ECs, P-selectin is released to the cell surface, and expression of E-selectin and L-selectin is upregulated [14]. Being fixed in place, EC interactions with leukocytes are critical for the recruitment of circulating T cells to the site of inflammation [15].

Inflammation can occur in response to T cells interacting with the presentation of an antigenic peptide on the surface of an antigen-presenting cell (APC), such as a macrophage, dendritic cell or B cell [16]. T cell activation is dependent on a direct interaction between the APC and the T cell receptor. While the professional APCs above present antigens to T cells in circulation, non-professional APCs, including ECs, can also present antigens through similar mechanisms [16, 17, 18, 19]. This often occurs as a result of a viral or bacterial infection, and the infected cells present the foreign antigen. As described further in Section 1.1.3, antigen presentation by ECs within an allograft can lead to inflammation and acute graft rejection.

Once activated, CD4^{+} helper T cells release cytokines and bind to APC surface receptors to stimulate and guide the inflammatory response. CD8^{+} cytotoxic T cells (T$_{\mathrm{C}}$), once activated, release cytotoxins including perforin, which permeabilizes the cell membrane, and granzyme B, which activates caspase-driven apoptosis [20]. T$_{\mathrm{C}}$ cells can then invade through the endothelial layer and damage the parenchyma [21].

In this dissertation we investigate the role of interleukin (IL)-15 surface presentation

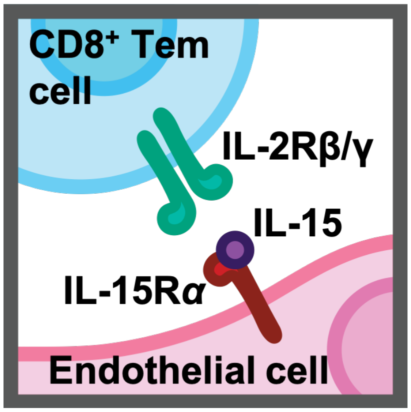

Figure 1.2: Trans-presentation of IL-15 in complex with IL-15Rα.

on ECs in the recruitment, activation, and proliferation of leukocytes. IL-15 binds tightly to its receptor, IL-15Rα, and can activate CD8$^+$ effector memory T (T_{EM}) cells via trans-presentation to IL-2Rβ/γ receptors (**Figure 1.2**) [22, 23, 24]. Human ECs primed with interferon (IFN)-γ then activated by complement express on their surface IL-15 in complex with IL-15Rα [25]. This boosts the responses of allogeneic CD8$^+$ T_{EM} cells which express IL-2Rβ/γ on the CD8$^+$ T_{EM} cell surface. Preventing this interaction with a blocking antibody limits CD8$^+$ T_{EM} cell activation, suggesting that reducing IL-15 expression is a useful target for preventing immune-mediated damage to transplanted allografts [25, 26]. In Chapter 2, we use siRNA against IL-15 to knock down this cytokine in human ECs.

1.1.3 Endothelium in Solid Organ Transplantation & Engineered Vascular Grafts

The immune surveillance role of the endothelium presents a challenge in the context of solid organ transplantation. The endothelium of an allograft is the initial point of contact and exchange with the host circulation. By presenting antigens that are alloreactive to the recipient, grafted ECs can elicit a strong immune response by mechanisms described in Section 1.1.2, which can ultimately lead to acute rejection of the graft [17]. Transplant recipients are often treated with immunosuppressants to reduce the risk of graft rejection; however, these treatments weaken the immune system overall and leave the graft recipients vulnerable to infections.

Even considering the immunogenic properties of allogenic ECs, the viability of a graft post-implantation relies on a functional and perfused graft endothelium that integrates with the host circulatory system. As described in Section 1.1.1, vascular networks, including microvasculature, are essential for carrying oxygen and nutrients and eliminating waste products throughout a tissue. Damage or dysfunction of the endothelium in a graft can be detrimental to the transplantation outcome. Graft endotheliopathies may be pre-existing in the donor or may arise during procurement, cold storage, or reperfusion after transplant. Microvasculature is particularly susceptible to damage and dysfunction as the small capillaries can easily become occluded.

Despite these challenges, transplantation from a living or deceased donor is the most effective treatment for end-stage organ diseases. The gap between the number of solid organ transplants occurring each year and the number of patients on the transplantation waiting list indicates an unmet clinical need for transplantable organs [27, 28]. Three strategies to overcome this shortage are being investigated and deployed as complementary approaches.

First, a reduction in the demand for transplantable organs may be achieved through preventative care and improved treatments of existing conditions, such as diabetes and hypertension [29]. Of relevance to the work described in this dissertation, examples of therapies that target the endothelium specifically are discussed in Section 1.1.4.

Second, *ex vivo* treatment of donor organs between procurement and implantation may increase the pool of transplantable organs by improving the health and predicted outcome of marginal organs that may have otherwise been discarded. A high discard rate of organs from higher-risk donors is a major contributor to the shortage of transplantable organs [30]. Direct access to treat the endothelium of a donor organ can be reached using *ex vivo* normothermic machine perfusion (NMP). This enables delivery of fibrinolytic agents, anti-inflammatory drugs, or gene therapies that alter the expression of genes involved in antigen presentation and T cell attachment and activation. An otherwise marginal organ may be considered to be suitable for transplantation following *ex vivo* treatment to clear vascular obstructions or suppress the immunogenicity of the allograft [31]. In Chapter 3 we describe a digital pathology tool for quantitative analysis of biopsies that we developed and have used to evaluate biopsies taken from human organs following NMP [32]. The efficiency of therapeutic delivery to the endothelium during the short window between procurement and transplantation can be increased with the use of nanocarriers targeted to EC surface antigens. Targeting approaches and examples of endothelium-targeted vehicles are discussed in Section 1.3.

A third strategy aims to increase the availability of graft tissue through the engineering of functional tissues from cultured cellular components. A significant barrier to engineering larger tissues or whole organs is the need for an integrated microvascular network in the graft in order to support the survival of tissues thicker than 400 um [33, 34]. Microvascular networks can be assembled from human cells in the lab by manipulating cultured endothelial cells [35]. By incorporating ECs along with other tissue-specific cell types comprising a graft, a functional endothelium that supports the graft following implantation can be achieved. Engineered tissues that incorporate channels for fluid transport or EC-lined microvessels have better viability *in vitro* and following implantation *in vivo*, compared with identical grafts made without channels or ECs [36]. Printing tissues using bio-inks containing different cell types, substrates, and growth factors has enabled precise construction of 3D vascularized tissue grafts [37, 38, 39, 40].

Prior to assembly into a graft with multiple cell types, each cell type can be individually pre-treated to optimize the functionality and other properties of that tissue component. For off-the-shelf tissue engineered grafts, the endothelial cell source will likely be allogenic to the recipient, and thus introduces the risk of acute rejection. Gene therapies or other anti-inflammatory treatments can be applied to ECs prior to graft assembly to generate tissues that are less immunogenic. A strategy for modulating expression of the cytokine IL-15 in ECs is investigated in Chapter 2. Treatments aimed at improving the assembly of ECs into microvascular networks, such as growth factors or miRNAs, can also be delivered to cells during graft construction.

1.1.4 Treating the Endothelium

The endothelium serves unique specialized functions throughout different organ systems in the body, however its ubiquity throughout all tissues makes it a useful and accessible target for therapeutics aimed at treating a wide range of conditions. As described above, the endothelium plays a critical role in inflammatory responses, making ECs a useful therapeutic target for preventing or reducing inflammation [17]. ECs also have an active role in vascular diseases such as atherosclerosis, thrombosis, and ischemia-reperfusion injury, in which the therapeutic target is primarily in the vascular lumen. The endothelium also has a critical role in the outcome of diseases that affect other tissues in the body, including cancer and respiratory diseases, in which the ECs or extravascular tissues are treated.

Many therapeutics that target the vascular lumen are used to clear obstructions in the vasculature that can lead to ischemia. These obstructions can be caused by a build-up of plaque (atherosclerosis) or by blood clotting (thrombosis), and are commonly treated with anticoagulants such as thrombomodulin (TM), tissue plasminogen activator (tPA) [31, 41]. Reactive oxygen species (ROS) can build up in the endothelium as a result of inflammation or ischemia-reperfusion injury. Enzymes that quench ROS such as catalase and superoxide dismutase can be administered to protect ECs against oxidative stress [12]. For several of these treatments, there have been promising results demonstrating delivery of the therapeutic agent in delivery vehicles designed to target ECs, which is discussed further in Section 1.3.

In addition to treatments for vascular diseases, treating certain vascular beds can also be motivated by diseases in the surrounding tissues. In many forms of cancerous tumors, the surrounding microvasculature becomes angiogenic and ECs develop abnormal morphologies that can contribute to intravasation and metastasis of cancerous cells [42]. Treating tumor vascular beds to either inhibit angiogenesis or normalize the growth of vascular structures has been found to be an effective strategy for treating tumors [42, 43, 44].

Pulmonary vascular beds can also be a therapeutic target [45, 46, 47]. In the ongoing COVID-19 pandemic, infection with the SARS-CoV-2 virus can cause inflammation in the lungs leading to acute respiratory distress syndrome (ARDS). One indicator of severe illness due to Sars-CoV-2 infection has been found to be damage to the pulmonary endothelium. Lung endothelial cells can amplify inflammation through expression of leukocyte adhesion molecules [48]. Therapeutics that act on the lung endothelium may help treat or prevent severe cases of COVID-19 [49, 50, 51, 52, 53, 54, 55, 56].

Another highly regulated surface of exchange between the blood stream and extravascular tissue is in the brain, where the endothelium is part of the blood brain barrier (BBB). Treatments aimed at the brain endothelium may be employed not only for the treatment of the endothelium itself, but also as a way of creating an entry point for drug delivery to the brain [57]. Using delivery vehicles functionalized with a ligands that bind to specific receptors on ECs in the BBB can promote transcytosis of the delivery vehicle and cargo [58, 59, 60, 61], although there appears to be a limit to the extent that this approach can shift the balance of NP biodistribution to the peripheral tissues and the brain: generally, less than 1% of the injected dose goes to the brain [62]. Cell-specific targeting strategies are discussed in Section 1.3.

1.2 Nucleic Acid Delivery to the Endothelium

1.2.1 Therapeutics Targeting messenger RNA

Modulating mRNA is a powerful way of reaching ‘undruggable’ protein targets. In this section we focus on two oligonucleotide-based therapies: small interfering RNA (siRNA), which modulates mRNA levels through the RNA interference (RNAi) pathway, and antisense oligonucleotides (ASOs) which modulate splicing or block translation [63].

RNA interference (RNAi) is a mechanism in eukaryotic cells that silences gene expression by sequence-specific cleavage of mRNA, which blocks translation. RNAi is initiated by the presence of double stranded RNA (dsRNA) in the cytoplasm, which endogenously, can arise from either microRNA (miRNA) or small interfering RNA (siRNA) pathways [64]. The dsRNA is cleaved into short (21 – 26 bp) dsRNA molecules, then one strand is assembled into the RNA-induced silencing complex (RISC). This guides binding to the complementary target mRNA sequence, which is then cleaved by endonucleases in RISC (**Figure 1.3**) [64].

Synthetic siRNA can be delivered to cells or tissues to silence protein expression [65]. It is widely used as a research tool, and is now gaining momentum as a therapeutic agent [66, 67, 68]. Twenty years after RNAi was first discovered in Caenorhabditis elegans by Fire and Mello and colleagues, the first siRNA drug, patisiran, achieved FDA approval in 2018 [69, 70]. Since 2018, three additional siRNA drugs have been approved by the FDA – givosiran, lumasiran and inclisiran – and dozens more are in clinical trials [70, 63].

ASOs are single stranded chemically modified oligonucleotides (12 – 30 nucleotides in length) that bind to sequence-specific mRNA, pre-mRNA, or miRNA targets by Watson-Crick base pairing [71]. ASOs can be designed to target mRNA in a variety of ways to either elevate or reduce translation. ASOs can block translation by binding to a target sequence on mRNA, block miRNA-mediated suppression by binding to a target sequence on miRNA, or modulate splicing (exon skipping or exon inclusion) by binding to a target sequence on pre-mRNA. ASOs can also be designed to promote cleavage of pre-mRNA or mRNA by RNAse H1 or argonaute 2 [71].

ASOs predate siRNAs as a therapeutic technology. Therapeutic applications of ASOs were first proposed in 1978. The first ASO drug, fomivirsen, was approved by the FDA in 1998, the same year in which the RNA interference pathway was discovered [63]. There are currently nine FDA-approved ASO therapies. The approval of nusinersen in 2016 to treat spinal muscular atrophy (SMA) represented a breakthrough in treatment for SMA and in the development and commercialization of ASO therapeutics. Nusinersen promotes inclusion of exon 7 in survival motor neuron 2 (SMN2) by binding to intron 7, which increases the

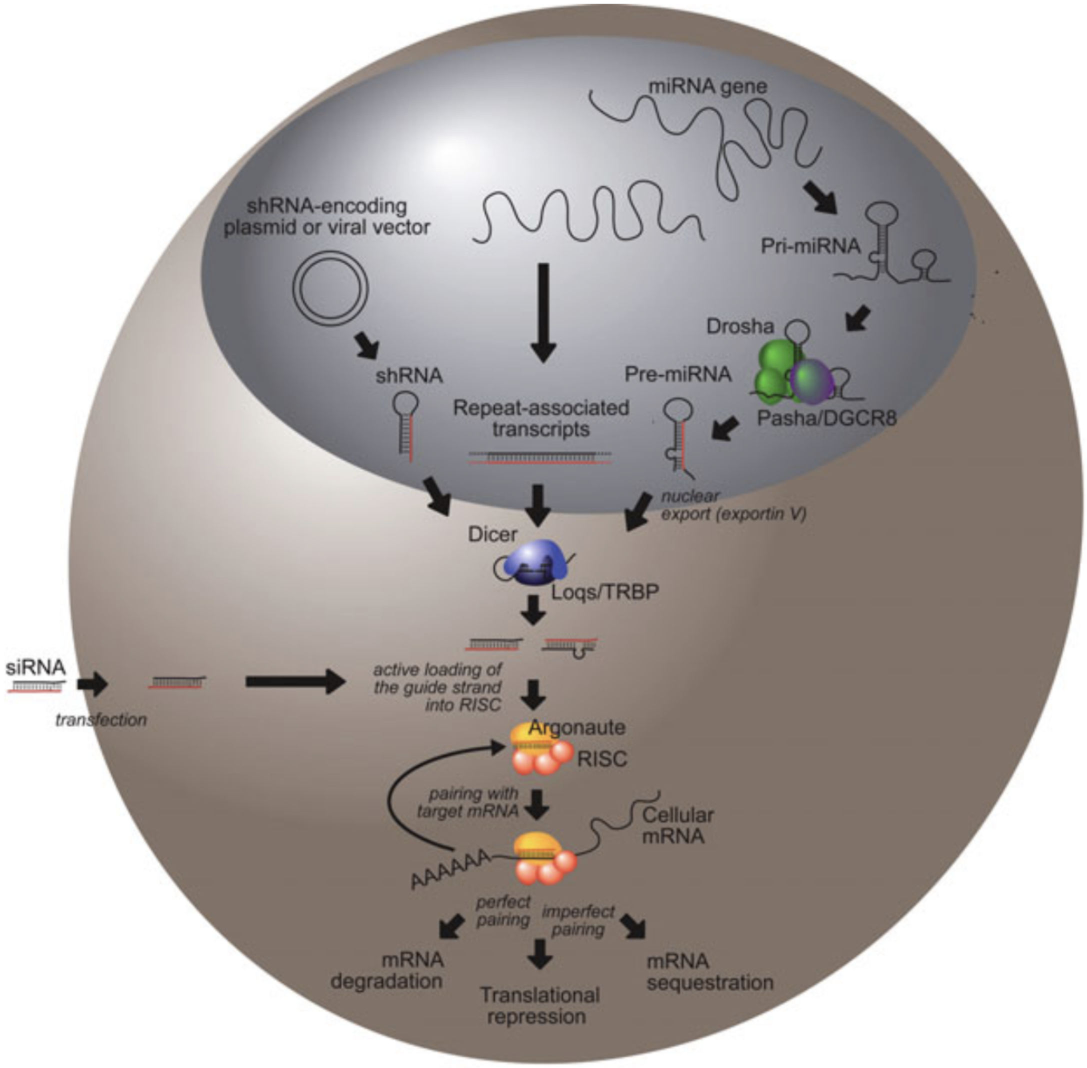

Figure 1.3: RNA interference pathway. From Giacca, M., 2011. [64]

production of fully functional SMN protein mRNA [71].

Both ASO and siRNA therapeutics are powerful because they can theoretically be designed to silence any gene. Targeting therapeutics at the protein level through small molecule-protein interactions requires more structural precision in the development of the drug, compared to designing complementary base pairing interactions to target mRNA or pre-mRNA sequences [70]. With siRNA drugs, RISC complexes can turn over to cleave multiple target mRNA strands so that gene silencing is propagated and has a prolonged effect [72]. Once inside the target cell silencing effects can be sustained for several weeks in non-dividing cells, however in rapidly dividing cells the siRNA may be diluted below an effective dose within 7 days [73]. An important advantage of ASO therapies is the ability to modulate splicing and target different steps of RNA processing.

The primary hurdle in designing nucleic acid therapies is in designing a suitable delivery approach that protects the oligonucleotide cargo from degradation, enables efficient uptake into cells, and delivers a sustained gene silencing effect in the relevant organ. Strategies for encapsulating and delivering nucleic acids are described throughout the remainder of Chapter 1. In Chapter 2, we use siRNA to silence human IL-15 expression in HUVECs, a target chosen for its role in CD8$^+$ T cell activation as described in Section 1.1.2.

1.2.2 Nucleic Acid Delivery Challenges and Approaches

There are a number of barriers that must be overcome for broader clinical usage of nucleic acid therapies. The bioavailability of naked oligonucleotides is limited by their size and negative charge, renal clearance, and susceptibility to degradation by nucleases which are present throughout tissues [70].

Oligonucleotides can be protected from degradation by encapsulation in nano-scale delivery vehicles (**Figure 1.4**). Viral vectors [74], lipid nanoparticles (LNPs) [75, 76, 77] and cationic polymers are commonly used as nucleic acid delivery vehicles. Polymeric vehicles for nucleic acid delivery are discussed further in Section 1.2.3. Bioconjugation of siRNA to stabilizing molecules such as cell penetrating peptides, aptamers, or lipids can also help protect ASOs or siRNAs from degradation [78, 63]. Delivery vehicles and conjugate molecules can also be designed to enhance cellular uptake, deliver to specific tissues, or optimize for efficient intracellular trafficking (**Figure 1.4**). The three FDA approved siRNA drugs and several phase 3 siRNA drugs are delivered either in LNPs or conjugated to a receptor targeted molecule N-acetylgalactoasamine (GalNAc) [70]. Backbone modifications to ASO drugs are used to protect the oligonucleotide from degradation while preserving RNA binding and RNAse H1 activation. Most commonly these include phosphorothioate (PS) linkages and

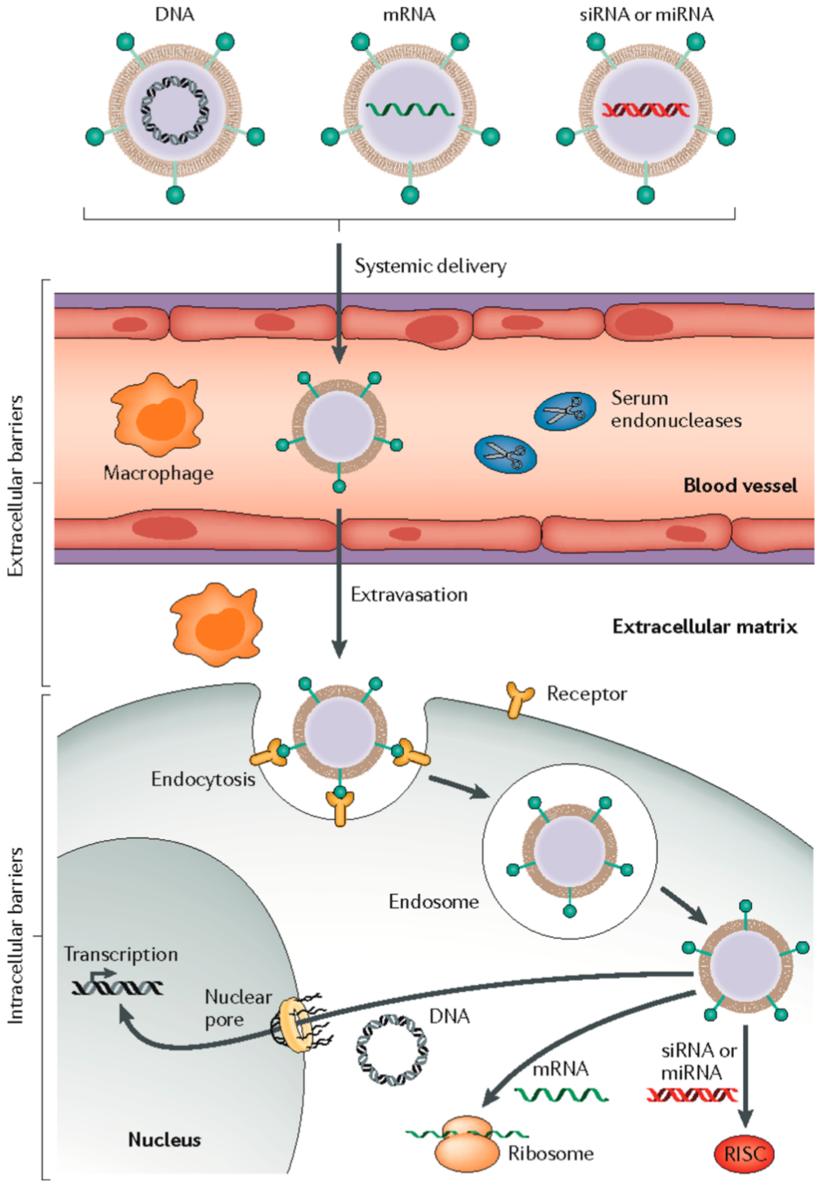

Figure 1.4: Extracelular and intracellular barriers to siRNA delivery. From Chen et al., 2019. [79].

the replacement of ribofuranose rings with morpholino rings to create phosphorodiamidate morpholino oligomers (PMOs) [63].

While delivery vehicles and bioconjugates can prolong the bioavailability of siRNA, they are still subject to renal clearance (for drugs or vehicles <10 nm in diameter) and clearance by phagocytic cells in the liver and spleen [68, 80]. In one study, selective siRNA delivery to the renal glomerular basement membrane (GBM) was achieved due to filtration of nanoparticles

(10 - 100 nm in diameter) through endothelial fenestrations (≈100 nm) in the glomerulus, and subsequent disassembly of the nanoparticles in the proteoglycan-rich GBM, where released siRNA was able to pass through the smaller pores of the GBM [81]. Accumulation of nanoparticles in the liver has been taken advantage of to deliver siRNA to treat inflammation [82] or alcoholic liver disease and fibrosis [83] in the liver. A novel approach using *in vivo* self-assembly of siRNA vehicles has recently been described in which liver cells are programmed to synthesize and package siRNAs into secretory exosomes for delivery to other tissues in the body, so that the liver does not need to be avoided but is rather the first destination in this therapeutic approach [84]. siRNA can also be delivered locally using nanocarriers to enhance sustained release and prolong gene silencing at the delivery site [85].

Delivery vehicles vastly improve the effectiveness of oligonucleotide therapeutics compared to administering free nucleic acid. Controlling certain properties of nanomedicines such as size, shape, charge density, and stealth coatings can help overcome rapid clearance and protect siRNA from enzymatic degradation [86, 87]. Targeting based on morphological properties of the target tissue (for example, fenestrated or sinusoidal endothelia) or by affinity-based targeting approaches can also help siRNA nanomedicines reach the relevant cells [12, 88].

1.2.3 Polymeric Delivery Vehicles for Nucleic Acids

Nucleic acid delivery vehicles fall in to one of two categories, viral and non-viral. Viral vectors are currently the predominant delivery method for clinical nucleic acid delivery applications. Around 70% of nucleic acid therapies currently in clinical trials around the world use viral vectors [89]. Non-viral lipid-based vectors have been developed as an alternative to viral vectors due to safety concerns regarding the immunogenicity of viral proteins [77]. Biodegradable polymeric delivery vehicles represent further innovation toward producing biocompatible nanocarriers with low immunogenicity [90, 91].

Polymeric delivery vehicles are a large and versatile category of delivery materials that are highly customizable. Physical and chemical properties of polymers can be easily modified to design vehicles for a broader range of types and sizes of nucleic acid cargos than can be delivered with viral vectors [91]. Cationic polymers are used for gene delivery because they efficiently condense nucleic acid cargos due to electrostatic interactions [79, 89]. Polycations often contain amine groups which give the polymer a positive charge. Diethylaminomethyl (DEAE) dextran was one of the earliest cationic polymers to be used for gene delivery, however it is highly cytotoxic [89, 92]. Other polycations that are commonly used today – including polylysines, polyethylenimines (PEI), poly(2-N-(dimethylaminoethyl) methacrylate) (PDMAEMA), and polyamidoamine (PAMAM) – have improved transfection efficiency over earlier methods, however the cytotoxicity of these polymers remains as a major limitation [89, 90].

In order to efficiently encapsulate nucleic acids an excess of polymer is typically used when formulating polycation delivery vehicles, resulting in particles with a net positive charge. This positive charge also promotes interaction with the cell surface, which contributes to the efficient transfection seen with cationic polymers. However, cationic polymers can disrupt the cell membrane and cause mitochondrial and lysosomal damage [93]. This can be overcome by introducing other polymer blocks that reduce the charge density [94].

Poly(beta-amino ester)s (PBAEs) are biodegradable tertiary-amine containing polymers [95]. The structure of PBAEs can be finely tuned to control hydrophobicity and other properties of the polymer [96]. The use of PBAEs for transfecting endothelial cells has been thoroughly investigated [35, 96, 97, 98]. From a large library of PBAE polymers generated using high-throughput combinatorial chemistry, polymers exhibited cell-type specific transfection efficiencies [98]. There was a high correlation in transfection performance between different types of endothelial cells, whereas there was little correlation between either EC type and an epithelial cell line. Additional non-viral vectors that have been investigated for nucleic acid delivery to the endothelium are shown in Figure 5 [96].

In Chapter 2 we investigate a family of biodegradable poly(amine-co-ester) (PACE) polymers for delivery of siRNA to the endothelium. PACEs are synthesized by copolymerization of an amino-diol, a diester, and a lactone, generating a mildly cationic polymer with tunable properties that can form solid nanoparticles or polyplexes with nucleic acid cargos [99, 100]. Like PBAEs, PACEs can been synthesized with different monomer compositions and chemical end groups [100, 101]. In Chapter 2 we explore chemical modifications to PACE that enhance nucleic acid loading and transfection in ECs. We also conjugate a thiol-reactive group to PACE, which we use to bind EC-targeting antibodies to the surface of PACE polyplexes.

1.3 Targeted Delivery to the Endothelium

1.3.1 Methods of Targeting

Nanomedicines can efficiently deliver imaging agents and therapeutic doses of drugs and nucleic acids to the desired tissue [102]. Vehicles designed specifically for nucleic acid delivery are described in Section 1.2.3. Doxil®, a liposome-encapsulated chemotherapy drug, was the first nanomedicine to reach FDA approval in 1995 [103]. In the nearly three decades that followed, many nanomedicines have reached the clinic including one of the first siRNA drugs described in Section 1.2.1 [70]. In addition to promoting stability and enabling sustained cargo release, nanocarriers of many kinds can be modified to target specific cells or tissues. However, despite numerous reports demonstrating the benefits of cell specific targeting of delivery vehicles, there are currently no targeted nanomedicines approved by the FDA [104].

Tissue- or cell-specific targeting can be achieved using passive targeting, ‘active’ or affinity-based targeting, or a combination of both. Passive targeting approaches make use of nanocarrier properties such as material composition, size, shape, or surface charge to promote accumulation in certain tissues (**Figure 1.5**) [86, 87, 105, 106].

Affinity-based targeting approaches, sometimes referred to as ‘active’ targeting, make use of ligand receptor interactions to promote accumulation of delivery vehicles in specific tissues

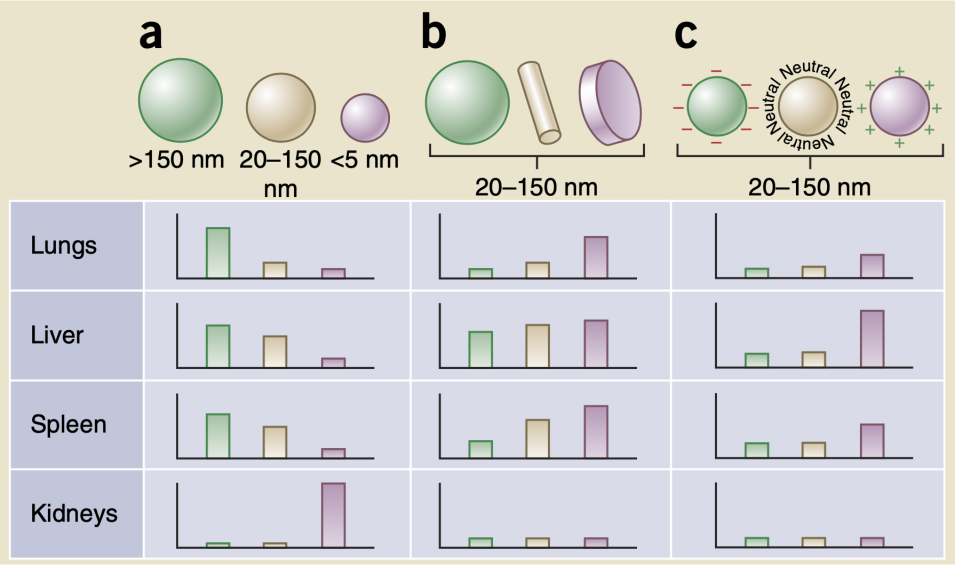

Figure 1.5: Effect of size (a), shape (b), and charge (c) on nanoparticle distribution. From Blanco et al., 2015. [86].

or cell types (**Figure 1.6**) [68, 107]. Ligands are typically attached to the surface of a delivery vehicle either through electrostatic interactions, covalent linkages via click chemistry or thiol coupling, biotin-avidin binding interactions, or nucleic acid hybridization, among others (**Figure 1.7**) [108]. These interactions and reactions can be used to conjugate a variety of nanocarriers (viral vectors, LNPs, polymers). Monoclonal antibodies are commonly used for targeting, however many different kinds of ligands can be conjugated to delivery vehicles to achieve similar effects. Arginine-glycine-aspartic acid (RGD) containing peptides bind to integrins and are widely used for enhancing cellular uptake of particles, along with other cell adhesive peptides [109, 110, 111, 112]. Applications of RGD peptides for targeting tumor microvasculature are described in Section 1.3.3. Hyaluronic acid (HA) conjugated to PEI has been used to target liver sinusoidal endothelial cells (LSECs), which express HA receptors [113]. Nucleic acid aptamers can also be developed to target specific cell surface molecules [114, 115]. More nuanced details of individual targeting ligands have also been investigated; one study found that using multiple ligands targeting distinct adjacent epitopes on a single target molecule (CD31) enhanced nanoparticle binding to ECs [116].

A third method of targeting nanocarriers is through ‘biomimetic camouflage’ approaches;

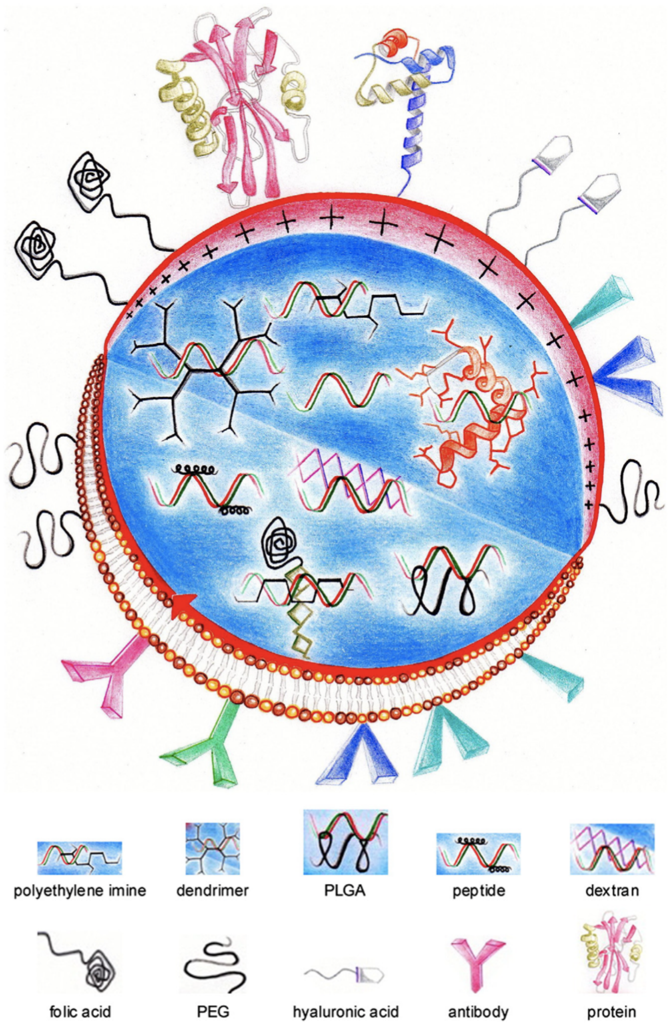

Figure 1.6: Modalities for targeted siRNA delivery vehicles. From Lorenzer et al., 2015. [68].

lipid membranes either derived from or designed to mimic other cell types, such as circulating leukocytes, are used to encapsulate drugs. These vehicles effectively evade clearance from immune cells, and they interact with and deliver cargo to inflamed endothelial cells via leukocyte receptor interactions [117]. Two or more targeting approaches can be combined; in one study, inflamed endothelium was targeted by generating ICAM-1 antibody-targeted neutrophil derived nanovesicles [118].

In Chapter 2 we investigate new formulations of poly(amine-co-ester) (PACE) polyplexes that target siRNA delivery to endothelial cells. We make use of some properties of

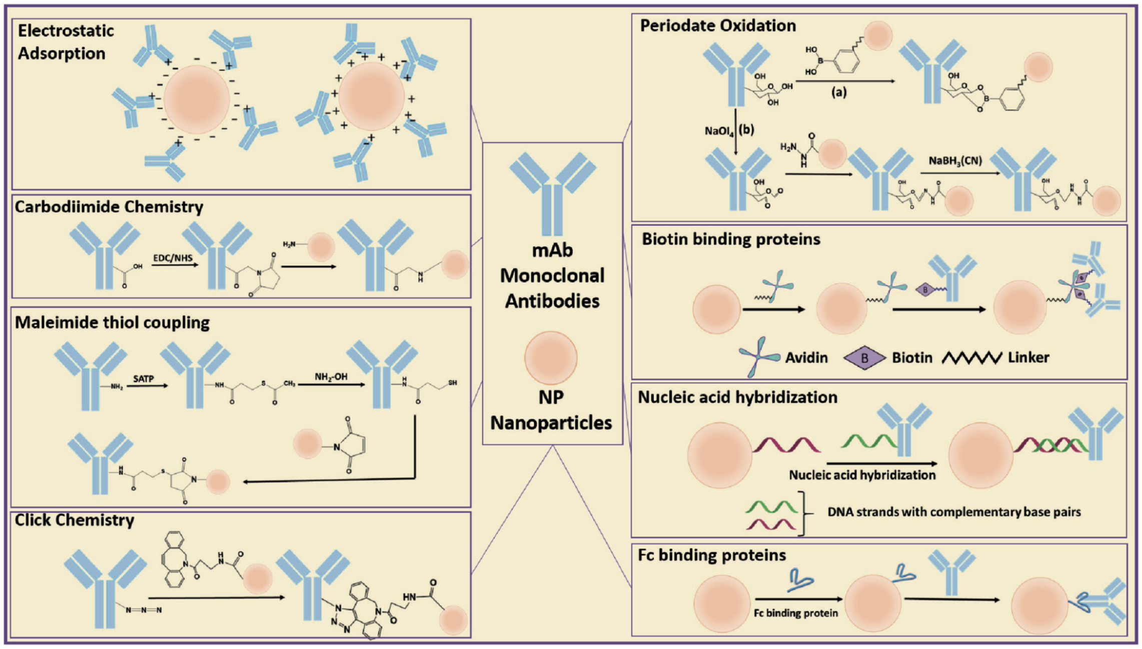

Figure 1.7: Strategies for antibody functionalization of delivery vehicle surface. From Sivaram et al., 2018. [108].

polymeric vehicles that are not based on specific affinity interactions, including PEGylation and polymer end-group chemistry optimization, and we also incorporate affinity-based targeting through conjugation of antibodies to the surface of the polyplexes. We adapt a recently developed method of introducing cell surface targeting antibodies to the surface of nanoparticles through a versatile mouse IgG1 Fc-binding monobody linker [119, 120]. The monobody linker contains a single cysteine residue which enables site specific binding to a thiol-reactive maleimide group exposed on the surface of the delivery vehicle. Once the monobody is conjugated to the surface, any mouse IgG1 antibody can be coupled to the delivery vehicle.

1.3.2 Delivery Vehicle Targeting in the Endothelial Environment

Endothelial cells experience constant blood flow across their luminal surface, so delivery vehicles do not have extended contact with ECs. The endothelial environment is also dense with serum proteins and hematopoietic cells that could affect the interaction between delivery vehicles and ECs. These properties support the motivation to develop targeted nanomedicines that bind to the endothelium. Particles in the blood stream also face rapid clearance from circulation, primarily in the liver for most nano-sized medicines. Targeting delivery vehicles to endothelial surface marker PECAM-1 (CD31) was recently shown to enhance mRNA delivery to the endothelium and prevent accumulation in the liver [121].

It is important to assess targeting methods in a setting that mimics the vascular environment [104]. Many studies employ microfluidic chambers that mimic the flow conditions of the vasculature. Endothelialized microfluidic chips are lined with ECs on the luminal walls of the channels [122]. These chambers allow for precise control over parameters such as flow rate and vessel diameter, and often many conditions can be tested simultaneously. However, as discussed in Section 1.1.1, cultured ECs do not always replicate *in vivo* phenotypes [13]. Furthermore, vasculature *in vivo* is made up of multiple cell types such as pericytes and smooth muscle cells, and extracellular matrix materials, all of which may have an impact on the properties of ECs, a factor that may limit the correlation between nanocarrier targeting *in vitro* versus *in vivo*.

A method for testing targeted nanocarriers in explanted human vessels was recently developed by Lysyy and Bracaglia and colleagues, and was used to test the targeted nucleic acid delivery vehicles described in Chapter 2 [123]. This *ex vivo* perfusion system maintains many of the advantages of using a benchtop microfluidic system as opposed to an *in vivo* animal model, such as being able to rapidly screen multiple conditions and vehicle formulations, while creating a binding environment that is truer to physiological conditions. Another method of testing nanocarrier targeting in human tissues *ex vivo* was described in Section 1.1.3; transplant-declined human organs placed on a normothermic machine perfusion system provide an organ-specific endothelium for testing formulations of targeted delivery vehicles [124].

While *in vitro* and *ex vivo* flow chamber systems are essential tools for the development of targeted therapeutics, it is important to note that targeting via receptor-ligand binding

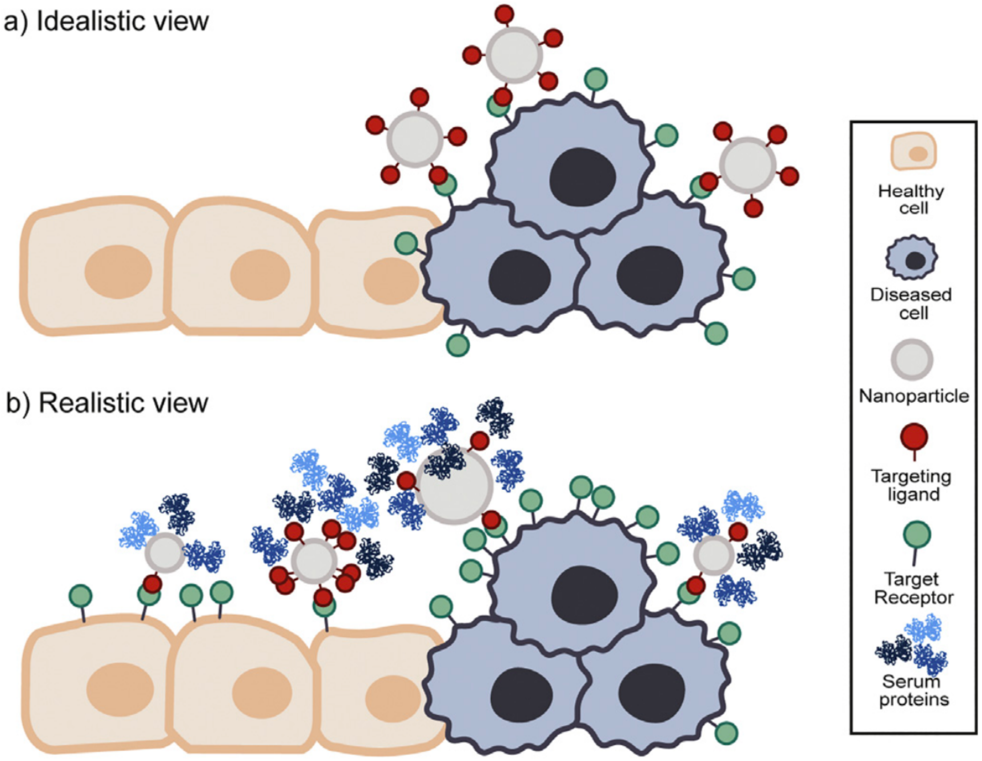

Figure 1.8: Targeted nanomedicines *in vivo*. From Woythe et al., 2021 [104].

does not work as a 'homing' mechanism; binding interactions only occur at a close range (<0.5 nm) [104, 107, 125]. A targeted nanoparticle that binds with high affinity to a specific EC marker *in vitro* will not necessarily reach and bind to the intended endothelial target *in vivo*. Further explorations into which binding properties, such as valency or binding kinetics, are most critical for designing targeted nanocarriers are being investigated [104, 126].

These binding interactions can be further impeded by other proteins and cells that the targeted vehicle may encounter (**Figure 1.8**) [104]. Ligands on the surface of delivery vehicles may be blocked by adsorption of serum proteins. Most surface antigens that have been used for targeting are not exclusively expressed in a single cell type, but rather are expressed to varying degrees in different cell types that a targeted delivery vehicle may encounter. In the following section (Section 1.3.3) we discuss endothelial cell surface antigens that have been shown to work well for targeting delivery vehicles.

1.3.3 Cell Surface Antigens for Endothelium Targeting

The endothelium is heterogeneous in cell morphology and protein expression, as described in Section 1.1.1 [11]. Adaptable antibody-based targeting platforms can be used to target organ-specific endothelia. As an example, angiotensin-converting enzyme (ACE) and thrombomodulin (TM) are both enriched in the pulmonary endothelium relative to other vascular beds and can be used to target nanocarriers to the lung endothelium [127].

EC phenotypes are also dynamic in response to changing physiological states [5]. This could work against targeting efforts if surface markers are shed or internalized in response to disease states or to ligand binding. Conversely, these dynamic properties could be an advantage for targeting specific areas of the endothelium where there is inflammation, vascular obstruction, nearby solid tumor growth, or other physiological changes (**Figure 1.9**) [12].

Surface expression of selectins and other adhesion molecules on cytokine-activated ECs has been used to target therapeutic delivery to inflamed regions of the vasculature [12]. E-selectin has been targeted using antibody-conjugated nanoparticles [128, 129, 130], a thioaptamer-conjugated to nanoparticles [131], and nanoparticles conjugated to an E-selectin binding molecule Sialyl Lewis A [132]. Inflammation in the endothelium can also be treated by targeting delivery to other molecules that are upregulated in inflammatory ECs including integrins [133], cell adhesion molecules VCAM-1 and ICAM-1 [134], transglutaminase [135], and von Willebrand factor [136].

As described in Section 1.1.4, ECs near tumors develop specific molecular and morphological phenotypes. These pathological features can be used to target nanomedicines to the microvascular beds surrounding a tumor. In a recent study, a screen of cancer-related antigens on breast tumor associated ECs (BTECs) identified CD105 (endoglin) as a target for selective delivery to BTECs over normal ECs, likely related to the role of CD105 in angiogenesis [137]. Angiogenesis in tumor microvascular beds can also be modulated by targeting drug delivery to integrins, in particular $\alpha_{\mathrm{v}}\beta_3$ and $\alpha_{\mathrm{v}}\beta_5$, which are overexpressed

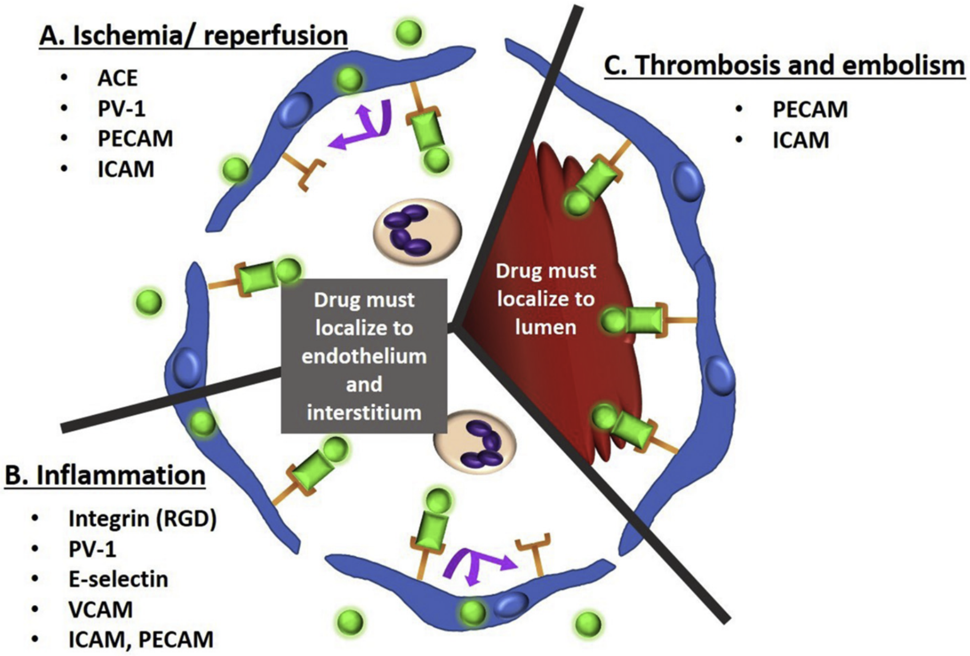

Figure 1.9: Endothelial antigens for targeting vascular pathologies. From Glassman et al., 2020. [12].

in angiogenic ECs relative to quiescent ECs [43]. Other potential target proteins that are overexpressed in tumor ECs include VEGF, VCAM-1, and matrix metalloproteinases (MMPs) [106]. Cargo of EC-targeted vehicles can be delivered to the ECs themselves to normalize their signaling and junctions, or to the cancerous cells via transcytosis through the endothelium or by passing through gaps in the affected endothelial layer.

Transmembrane proteins that are highly expressed in ECs relative to other cell types, abundant on all ECs throughout the vascular system, and persist on the cell surface regardless of other conditions or disease states are also useful for developing endothelium-targeted delivery vehicles. Several studies have performed side-by-side comparisons of two or more EC surface antigens including PECAM-1, ICAM-1, ICAM-2, VCAM-1, E-selectin and TfR-1 [74, 123, 126, 134]. In chapter 2 we functionalize the surface of poly(amine-co-ester) (PACE) polyplexes with antibodies against platelet endothelial cell adhesion molecule-1 (PECAM-1, or CD31) as a demonstration of our targeted delivery system in cultured ECs. We selected CD31 due to its abundant expression on ECs in culture and *in vivo* [138, 139].

Chapter 2

End Group Modified Poly(amine-co-ester) Polyplexes for Targeted Nucleic Acid Delivery to the Endothelium

The polymer synthesis described in this chapter was performed by Alexandra Piotrowski-Daspit, Ph.D (PACE-PEG-Maleimide) and Hee Won Suh, Ph.D (end group modified PACEs).

2.1 Abstract

Successful gene delivery to the endothelium is limited by a need for delivery vehicles that efficiently transfect endothelial cells (ECs) under physiologically relevant conditions. A family of cationic poly(amine-co-ester) (PACE) polymers is highly effective at encapsulating and transfecting nucleic acids in a variety of *in vitro* and animal models. The tunable properties of PACE terpolymers enable precise optimization of polymeric vehicles for different

delivery settings. In this study we identify a modified PACE polymer with a primary amine-containing end group that is optimal for transfection of human endothelial cells. We then incorporate a PEGylated PACE polymer to enhance the stability and reduce the toxicity of the delivery vehicle. Finally, we employ a new PACE-PEG polymer with a terminal maleimide group to covalently couple the delivery vehicle with antibodies targeting human PECAM-1 (CD31) using thiol-based coupling and a Fc-binding monobody adapter. We find that PACE vehicles formulated using EC-optimized polymer end group modifications and conjugated to CD31-targeting antibodies are taken up at higher rates compared to non-targeted vehicles. These results demonstrate the adaptability and customizability of PACE polymers and of the monobody adapter technology.

2.2 Introduction

Gene delivery to the endothelium has great therapeutic potential [50, 68, 129, 140]. A significant barrier that must be overcome is in the packaging of nucleic acids into a vehicle that can deliver therapeutic doses of nucleic acid cargos to endothelial cells. The endothelium is under a constant state of flow, meaning nanocarriers may not accumulate in desired areas, and the liver, spleen, and macrophages actively clear particles from circulation. Affinity-based targeting of delivery vehicles to the endothelium may overcome these barriers [12].

We have recently described the development of poly(amine-co-ester) (PACE) polymers [99, 100]. PACEs are a family of cationic polymers that efficiently encapsulate and serve as a delivery vehicle for nucleic acids (pDNA, mRNA, siRNA, and miRNA) *in vitro* and *in vivo* [83, 100, 141, 142]. PACE polymers are composed of three monomers: an amino-substituted diol, a lactone, and a diester. The amino-diol gives the polymer a cationic charge due to the tertiary amine, whereas the lactone and diester monomers confer hydrophobicity. The relative content of each monomer determines the physical properties of the polymer and delivery vehicles, as well as the encapsulation efficiency, stability, release profile, and biocompatibility. Varying monomer compositions have been systematically examined, demonstrating that this family of polymers offers a precise control over delivery vehicle properties [100]. This has been used to optimize PACE vehicles for specific applications, including the identifying optimal formulations for different types of nucleic acids, or for different routes of administration *in vivo*.

The PACE family has recently been further expanded to introduce new functionality and points of control over properties of the polymer and the delivery vehicles it can form. It was recently reported that PACE polymers can be actuated, by exposure to elevated temperatures (37°C – 100°C), to significantly improve transfection of mRNA *in vitro* and *in vivo* [143]. The improvement in transfection was associated with a hydrolysis-driven reduction in polymer molecular weight and change in polymer end group composition. This motivated the systematic generation of a library of PACE polymers conjugated to different amine-containing end group molecules [101]. Polymer performance metrics including mRNA encapsulation, cellular uptake, endosomal escape, and transfection varied significantly between end groups within the same cell type *in vitro*. Subsequently, different PACE end groups have been found to be optimal for transfecting different cell types *in vitro* and different tissues or with different administration routes *in vivo*.

Recent investigations into the customizability of PACE delivery vehicles have characterized the role of polyethylene glycol (PEG) surface coatings on transfection efficiency in different settings. PEG groups can promote stability and reduce cytotoxicity of cationic gene delivery polymers, but incorporation of PEG into delivery vehicles significantly reduces transfection efficiency *in vitro* [142, 144, 145]. PEG can enhance transfection *in vivo*, however the extent of enhancement depends on the tissue and route of administration [142, 146]. For example, PACE-mediated delivery to mucosal tissues such as the lung epithelium can benefit from PEG coatings to penetrate the mucosal barrier [142].

We sought to further develop the customizable properties of PACE polymers to design a PACE delivery vehicle optimized for specific binding and cargo delivery to human ECs.

To that end, we screened a subset of end-group modified PACE polymers that had shown high endosomal escape and transfection efficiency in other cell lines. We next synthesized a PEGylated PACE polymer with a thiol-reactive maleimide group conjugated to the end of the PEG group, PACE-PEG-Maleimide (PACE-PEG-Mal or PP-Mal). The maleimide group at the end of the hydrophilic 5 kDa PEG chain is exposed to the outer surface of the polyplex where it can engage in thiol-based coupling of molecules to the polyplex.

Here, we screened a selection of end group modified PACE polymers for siRNA transfection efficiency in human umbilical vein endothelial cells (HUVECs). We formulated PACE with siRNA against interleukin (IL)-15, a target that is relevant to our work in pretreatment of human organ grafts to prevent peri-transplant injuries. Human ECs primed with interferon (IFN)-γ and activated by complement express IL-15 on their surface in complex with IL-15Rα [23, 25]. This boosts the responses of allogeneic CD8^{+} effector memory T (T$_{\mathrm{EM}}$) cells which express IL-2Rβ/γ on their surface. Blocking this interaction limits host $^{+}$ T$_{\mathrm{EM}}$ cell activation, suggesting that reducing IL-15 expression is a useful target for preventing immune-mediated damage to transplanted allografts [24, 25, 26].

After identifying PACE-E2 as an end group derivative that optimized siRNA transfection in HUVECs, we generated CD31-targeted PACE-E2 polyplexes using a two-step coupling reaction and a monobody adapter system. An engineered Fc-binding monobody (Mb) containing a single C-terminal cysteine residue, which orients the Mb on the polyplex surface, enabled site specific coupling to the PACE-E2 polyplexes [119, 120, 147]. The Mb selectively binds the Fc region of mouse IgG1 antibodies, which we used to bind either an anti-human CD31 or an isotype matched control antibody to the surface of PACE polyplexes, generating Ab-Mb-polyplexes (either CD31-Mb-polyplexes or Iso-Mb-polyplexes). Our results using antibodies against CD31 to target to human ECs show proof-of-principle for a customizable and adaptable targeted nucleic acid delivery vehicle platform with PACE polymers.

2.3 Materials and Methods

2.3.1 Polymer Synthesis, Purification, and Characterization

Poly(amine-co-ester) (PACE) polymers were synthesized by enzyme (C. antarctica lipase B) catalyzed terpolymerization of pentadecanolide (PDL), methyldiethanolamine (MDEA), and sebacic acid (SA) monomers following previously published methods, with some modifications [99, 100, 143]. 10 mol% PDL was used for all polymers unless otherwise noted. Monomers were dissolved in diphenyl ether and allowed to oligomerize at 1 atm under argon at 90°C for 24 hours, after which polymerization proceeded under vacuum (2 mmHg) at 90°C for an additional 48 hours (**Supplemental Figure A.1**). For PACE-PEG synthesis, 5K MW PEG was an additional monomer. For PACE-PEG-Maleimide synthesis, 5K MW PEG-Maleimide was an additional monomer. For end group modified PACE polymers, amine-containing end groups were conjugated to PACE after polymerization, following previously published methods [101]. Polymers were purified following previously published methods and the composition and molecular weight were analyzed using proton NMR (Aligent DD2 400 MHz NMR Spectrometer) and GPC (Ultimate 3000 UHPLC; Thermo Fisher Scientific) [100].

2.3.2 Polyplex Formulation

Polyplexes were formulated at a polymer to nucleic acid ratio of 100:1 or 50:1 by weight as noted. PACE polymers were dissolved in DMSO at 100 mg/mL and incubated with shaking (350 rpm) overnight at 37°C. Polymer blends were made by combining PACE-PEG-Maleimide or PACE-PEG with PACE-E2 at a concentration of 3%, 10%, or 30% PEGylated PACE by weight. Control or IL-15 targeting siRNAs, or Cy5-labeled DNA or mRNA, was mixed with PACE polymers in sodium acetate buffer (25 mM, pH 5.8), vortexed for 25 seconds, then incubated for 10 minutes, RT (**Figure 2.1B**). For *in vitro* experiments, cells were treated at a concentration of 100 nM nucleic acid or 0.1 mg/mL polymer weight as noted.

2.3.3 Polyplex Characterization

Polyplex size and surface zeta potential was characterized by dynamic light scattering (DLS) using a Zetasizer Pro (Malvern Panalytical). Polyplexes were diluted to 40 μg/mL in deionized water for DLS measurements. Polyplexes were imaged by transmission electron microscopy (TEM, FEI Tecnai Osiris 200kV) using a tungsten stain. Nucleic acid loading was quantified using a Quant-iT PicoGreen dsDNA assay or a Quant-iT RiboGreen RNA assay (Thermo Fisher Scientific, Waltham, MA, USA). PicoGreen or RiboGreen reagent was added to polyplexes and fluorescence was measured with a plate reader. Fluorescence intensity was compared to a standard curve of DNA oligo, siRNA, or mRNA and encapsulation in polyplexes was calculated by subtracting the fluorescent signal in polyplex samples from the signal in a solution of free nucleic acid of equivalent concentration.

2.3.4 Monobody-Antibody Conjugation of Polyplexes

Monobody development has been described previously [147, 148, 149]. We used the monobody clone FCM101 with a C-terminal cysteine residue for site-specific thiol-mediated covalent coupling [147, 148].

Polyplexes were formulated with a polymer blend of 10% or 30% PACE-PEG-Maleimide (wt%) and PACE-E2. Centrifugal filtration in 100K MWCO filter tubes (MilliporeSigma, Burlington, MA, USA) was used for buffer exchange from sodium acetate buffer (25 mM, pH 5.8) to MES buffer (0.05 M, pH 5.5). Polyplexes were concentrated from 1 mg/mL to 5 mg/mL then washed with MES buffer and resuspended in MES buffer at a concentration of 5 mg/mL. A 2 mg/mL solution of monobody (Mb) in TCEP/TBS buffer, pH 7.5 was added to polyplexes to a final ratio of 20:1 polymer:Mb (w/w). Polyplex-monobody mixture was incubated for 1 hour at room temperature on an orbital shaker set to 250 rpm. Mb-polyplexes were then washed with PBS using centrifugal filtration and resuspended in PBS at a concentration of 5 mg/mL. A 1 mg/mL solution of anti-hCD31 or isotype control antibody in PBS was added to polyplexes to a final ratio of 18:1 polymer:Ab (w/w). Mb-polyplex:antibody mixture was incubated for 1 hour at room temperature on an orbital shaker set to 250 rpm (**Figure 2.4A**). For *in vitro* experiments, Ab-Mb-polyplexes were diluted to 1 mg/mL in PBS then added to cells to a final concentration of 0.1 mg/mL. For *ex vivo* isolated vessel perfusion system (IVPS) experiments, Ab-Mb-polyplexes at 5 mg/mL in PBS were injected directly into the perfusion loop for a final concentration of 0.1 mg/mL.

Polyplex size and surface zeta potential was characterized throughout the conjugation procedure by dynamic light scattering, as described above. To measure nucleic acid loading and Mb binding to the polyplexes, filtrate samples were collected following each buffer exchange step and analyzed by Quant-iT PicoGreen or RiboGreen assays, as described above, and by SDS-PAGE electrophoresis. Mb-Ab-polyplexes were imaged by transmission electron microscopy (TEM, FEI Tecnai Osiris 200kV) using a tungsten stain.

2.3.5 Evaluation of Polyplex Stability

CD31-Mb-polyplexes and Isotype-Mb-polyplexes formulated with Cy5-DNA were diluted to 1 mg/mL in PBS or PBS + 10% FBS and stored for up to one week at 37°C with shaking (350 rpm), or at 4°C. At each time point, 40 μg of polyplexes was removed and diluted in 1 mL deionized water for DLS measurement of size and zeta potential. To evaluate the effectiveness of polyplexes in delivering nucleic acid cargo after storage, polyplexes were stored in PBS or PBS + 10% FBS at 37°C, shaking (350 rpm), or at 4°C for 24 hours and 7 days. At each time point, polyplexes were delivered to HUVECs at a concentration of 0.1 mg/mL in complete media for 2 hours, 37°C. Cells were uplifted and analyzed by flow cytometry as described below.

2.3.6 Polyplex Delivery *in vitro*

Human umbilical vein endothelial cells (HUVECs) were obtained from the Yale Vascular Biology and Therapeutics tissue culture core. HUVECs pooled from three donors were isolated from fresh umbilical veins by collagenase digestion and cultured on 0.1% gelatin-coated flasks containing M199 medium (Gibco) supplemented with 20% FBS, 1% P/S, and 1% endothelial cell growth supplement (ECGS). Cells were plated into multi-well plates coated with 0.1% gelatin at a concentration of 100,000 cells/mL and grown overnight. Fresh media was added to cells prior to treatment. For IL-15 siRNA delivery, IFN-γ (100 ng/mL) was added to the media to stimulate IL-15 expression.

Fresh polyplexes in sodium acetate buffer or Ab-Mb-polyplexes in PBS were added dropwise to cells at a concentration of 100 nM nucleic acid or 0.1 mg/mL polymer, as noted. Polyplexes were left on cells for 2, 18, or 24 hours, where noted. Polyplex delivery of dye labeled oligos and siRNA was assessed by measuring cellular uptake of encapsulated dye-labeled DNA using flow cytometry, or by measuring IL-15 expression and knockdown using RT-qPCR.

2.3.7 Polyplex Toxicity *in vitro*

Cell viability following polyplex treatment was measured using flow cytometry staining (SYTOX Green, propidium iodide, or Annexin V; Thermo Fisher Scientific) or using CellTiter-Glo 2.0 luminescent cell viability plate reader assay (Promega).

2.3.8 Polyplex Delivery to Human Umbilical Arteries in An isolated Vessel Perfusion System

An isolated vessel perfusion system (IVPS) was set up as previously described [123]. Briefly, de-identified human umbilical cords were obtained from Yale-New Haven Children's Hospital (New Haven, CT) from scheduled cesarean sections (C-section). Umbilical arteries were dissected from the cord on ice and cut into 10 cm segments. Vessels were cannulated and assembled into perfusion chambers connected to tubing running through a peristaltic pump. Vessel chambers were immersed in a 37°C water bath and vessels were perfused in a closed loop with 5 mL complete M199 media at a flow rate of 2.5 mL/min. After 15 minutes of perfusion, 100 μL of polyplexes (5 mg/mL in PBS) were injected into the perfusion loop as a bolus. Vessels were perfused for 30 minutes or 1 hour, where noted. Vessel chambers were then disassembled and vessels were prepared for analysis by flow cytometry and confocal microscopy as described below.

2.3.9 Flow cytometry

For *in vitro* experiments, cells were washed three times with warm cell culture media and once with HBSS. Cells were then detached with TrypLE Express (Thermo Fisher Scientific), washed with PBS, and resuspended in 1%BSA/PBS. Cells were then stained with either SYTOX Green or propidium iodide (Thermo Fisher Scientific) to exclude dead cells. Cells were stained with a PE conjugated human IL-15 antibody (R&D Systems) for 30 minutes at room temperature. Cells were then washed with FACS buffer and analyzed using an Attune NxT flow cytometer.

For IVPS experiments, vessels were removed from perfusion chambers and filled with warm collagenase solution (0.1% in PBS) (Worthington Biochemical). After 10 minutes at 37°C, vessels were flushed with 1 mL of FACS buffer (1% BSA/PBS), collecting the flow through. Cells were pelleted and resuspended in FACS buffer containing Alexa Fluor 488 labeled anti-human CD105 (Thermo Fischer Scientific) or an isotype control (Alexa Fluor 488 mouse IgG2a, BD Pharmingen). Cells were stained for 1 hour on ice, then washed with FACS buffer and analyzed using an Attune NxT flow cytometer.

2.3.10 Microscopy

For *in vitro* polyplex uptake imaging, HUVECs were plated on gelatin-coated glass-bottom well plates and grown for 24 or 48 hours until fully confluent. Cells were treated with Cy5-labeled DNA loaded polyplexes in complete media for two hours at 37°C. Following treatment, cells were washed with media three times then fixed with 2% PFA in cell culture media for 10 minutes at room temperature. Cells were then washed with PBS, permeabilized with 0.1% Triton X-100, then stained with Alexa Fluor 555 conjugated phalloidin (Thermo Fisher Scientific) for 60 minutes at room temperature. Cells were then washed with PBS and stained with Hoechst and imaged using an EVOS FL Auto 2 microscope (Thermo Fischer Scientific).

Polyplex uptake in perfused human umbilical arteries was visualized by whole-mount en face confocal microscopy, as described previously [123]. A 2 mm segment of the perfused artery was stained with Alexa Fluor 488 labeled anti-human CD105 (Thermo Fischer Scientific) for 1 hour on ice. Vessel segments were washed twice with 1% BSA/PBS, then stained with Hoechst (1 ug/mL in 1% BSA/PBS) (Sigma) for 10 minutes. Vessel segments were mounted on microscope slides and coated with glycerin. Images were captured with an LSM 410 spinning-disc confocal microscope and processed using Zen (Carl Zeiss).

2.3.11 Statistical Analysis

Results were analyzed using GraphPad Prism (version 9.3.1 for macOS).

2.4 Results and Discussion

2.4.1 PACE Polymer Synthesis and Functionalization

PACE polymers were synthesized by enzyme catalyzed terpolymerization of an amino-substituted diol (MDEA), a lactone (PDL), and a diester (SA) following previously published methods (**Figure 2.1A, Supplemental Figure A.1**) [99, 100, 143]. Methyldiethanolamine (MDEA) provides a tertiary amine, giving the polymer a mildly cationic charge which promotes complexation with nucleic acids. The lactone monomer, pentadecanolide (PDL), confers hydrophobicity which can enhance the stability and reduce cytotoxicity of the resulting polyplex. A long chain diester monomer, either sebacic acid (SA) or diethyl sebacate (DES), adds additional control of hydrophobicity. The 10 wt% PDL PACE polymers used in this study are viscous at room temperature and form polyplexes upon dissolution in an aqueous buffer (sodium acetate buffer, pH 5.8) and vigorous mixing with a nucleic acid solution (**Figure 2.1B**) [100]. From a library of 30 end group modified PACE polymers generated in a previous study, we selected 6 polymers to test with ECs; we selected this set of polymers based on their previously identified high endosomal escape and transfection efficiency in Expi293F cells (**Figure 2.1C**) [101].

Having previously found that incorporation of a PEG-PACE block copolymer improved polyplex stability and reduced cytotoxicity, and motivated by enabling further functionalization of PACE polyplexes, we synthesized a new PACE polymer, PACE-PEG-Maleimide (PACE-PEG-Mal or PP-Mal) that terminates with a maleimide group at the end of a 5 kDa PEG chain (**Figure 2.1D**). PACE-PEG-Mal can be combined with other end group modified PACE polymers to form blended polyplexes. The thiol reactive maleimide end group on PP-Mal enables coupling of the polymer, or a polyplex made with this polymer, to an exposed thiol.

We used a monobody designed with a single cysteine residue at the C-terminus as an adapter to attach antibodies targeting an EC-specific surface antigen to the surface of polyplexes formulated with a blend of PP-Mal and PACE-E2 (**Figure 2.1E**) [147, 148, 149].

2.4.2 Screen of End Group Modified PACE Polymers

A library of PACE polymers conjugated to a variety of amine-containing end groups was generated in a previous study [101]. We sought to identify end group modified PACE

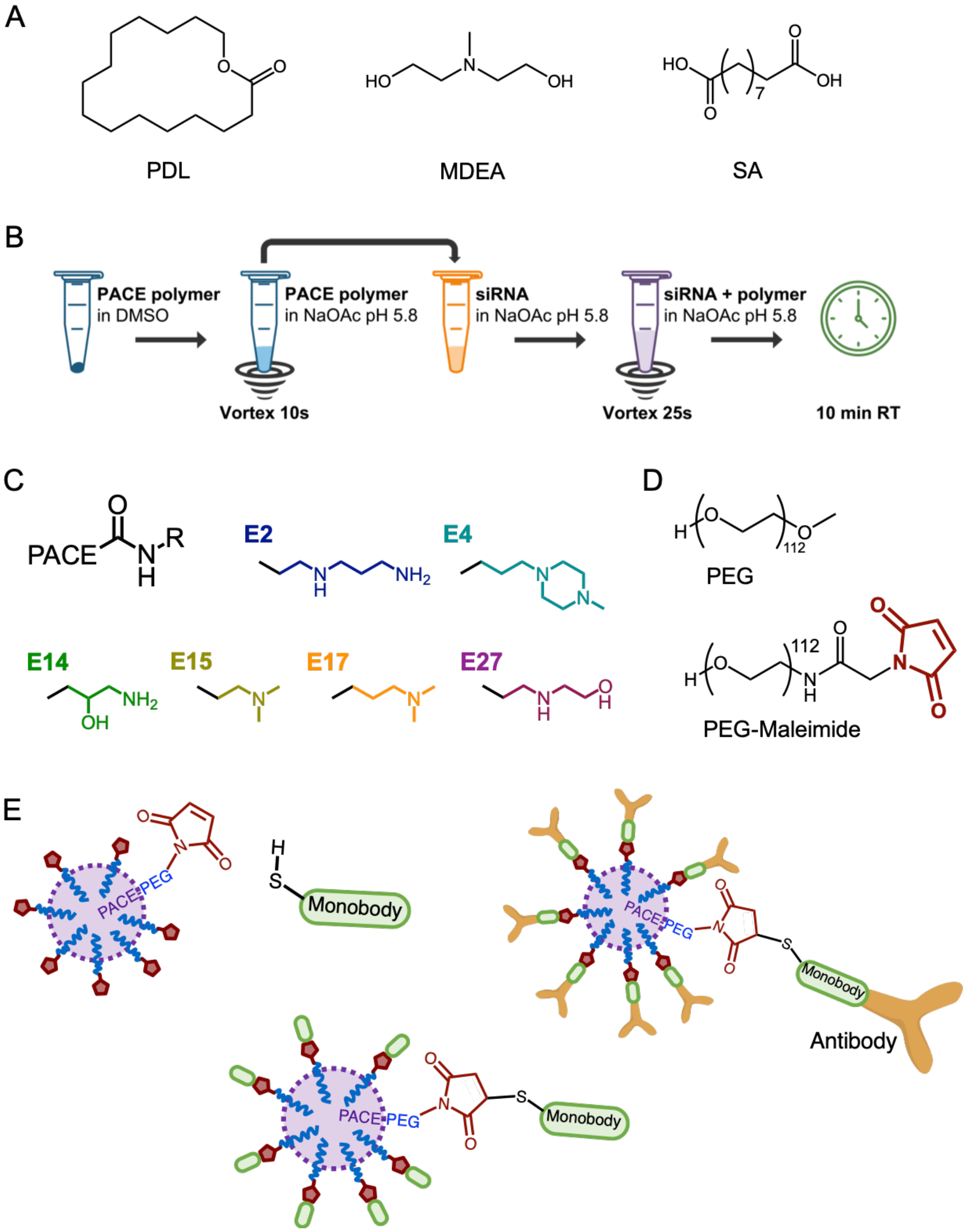

Figure 2.1: PACE end group synthesis and polyplex surface conjugation. (A) Poly(amine-co-ester) (PACE) is synthsized by copolymerization of pentadecanolide (PDL), methyldiethanolamine (MDEA), and sebacic acid (SA). **(B)** PACE polyplexes are formulated by mixing polymer and nucleic acid solutions in sodium acetate buffer. **(C)** End group modified PACE polymers. **(D)** 5 kDa poly(ethylene glycol) (PEG) or PEG-Maleimide can be added as additional monomers in PACE synthesis to create PACE-PEG or PACE-PEG-Mal. **(E)** Polyplexes formulated with a blend of PACE-PEG-Mal can be conjugated to a monobody adapter in order to attach antibodies to the polyplex surface.

polymer(s) that efficiently transfect endothelial cells. To screen for the best performing polymer, we first characterized the size, PDI, and surface charge of polyplexes formulated using each of the six end group modified PACE polymers shown in **Figure 2.1**. Polyplexes were formulated with siRNA as the nucleic acid cargo. All polyplexes were between 70 – 110 nm in diameter with PDIs between 0.25 – 0.4 (**Figure 2.2A**). With the exception of PACE-E2, all of the polymers formed polyplexes with a positive surface charge between 22-28 mV (**Figure 2.2B**). PACE-E2 polyplexes were the smallest in diameter, and had a more positive surface charge of 38 mV (**Figure 2.2A,B**).

We then transfected human umbilical vein endothelial cells (HUVEC) with siRNA targeting IL-15 encapsulated in polyplexes formulated using each of the six end group modified PACE polymers, as well as a 'classic' carboxyl end group PACE and a commercial transfection reagent (Lipofectamine RNAiMAX, Thermo Fisher Scientific). Knockdown efficiency of IL-15 mRNA after 24 hours was measured by RT-qPCR. We found that PACE-E2, which terminates in a primary amine (**Figure 2.1C**), delivered the highest knockdown percentage relative to cells treated with a control siRNA (**Figure 2.2C**). PACE-E14 also terminates in a primary amine and performed significantly better than RNAiMAX and other PACE polymers (**Figure 2.2C**). HUVECs are known to be difficult to transfect with siRNA, so it was not unexpected to see only ∼50% knockdown with the commercial reagent. Furthermore, PACE-E2 polyplexes delivered a more sustained knockdown effect than RNAiMAX following a single siRNA treatment (**Supplemental Figure A.2A**).

2.4.3 Incorporation of PACE-PEG in PACE-E2 Polyplexes

We found that while PACE-E2 effectively delivered siRNA to HUVECs, it also caused some toxicity. However, incorporation of 2.5% PACE-PEG (PP) in polyplexes significantly improved cell viability (**Figure 2.2D**). This is consistent with previously reported data [100, 142]. Incorporation of small amounts of PEGylated PACE into PACE polyplexes increases hydrophilicity, which reduces interactions with soluble proteins and with the cell

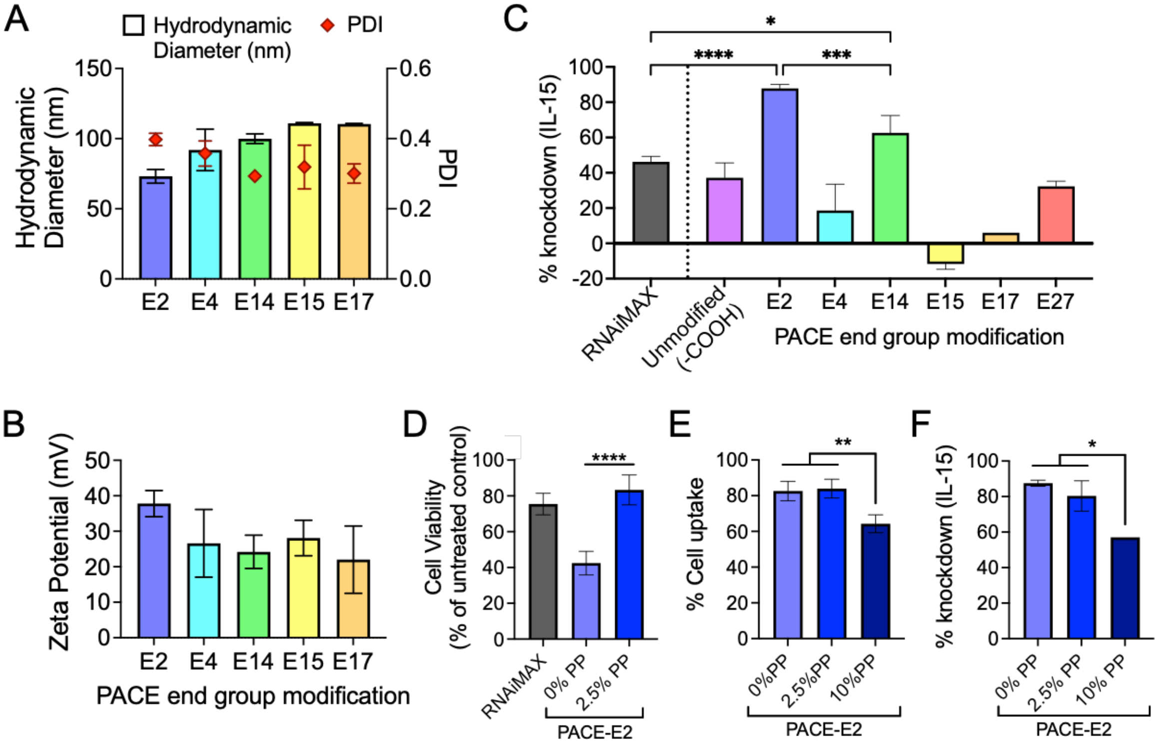

Figure 2.2: Screen of end group modified PACE polymers for optimal siRNA transfection in human endothelial cells. (A) Hydrodynamic diameter (bars) and PDI (red diamonds) and **(B)** zeta potential of of polyplexes formulated with end group modified PACE polymers encapsulating siRNA against human IL-15. **(C)** Percentage of IL-15 knockdown in HUVECs using end group modified PACE polymers, unmodified PACE-COOH, and Lipofectamine RNAiMAX (Thermo Fisher Scientific). Percent knockdown is calculated relative to cells treated with a non-targeting control siRNA. **(D)** *In vitro* cytotoxicity of PACE-E2 polyplexes. **(E)** Cellular uptake of PACE-E2 polyplexes formulated with 0%, 2.5%, or 10% PACE-PEG (weight%) encapsulating dye-labeled oligo following 24 hours of treatment in static culture. **(F)** Percentage of IL-15 knockdown in HUVECs by siRNA encapsulated in PACE-E2 polyplexes formulated with 0%, 2.5%, or 10% PACE-PEG (weight%). *$p<0.05$; **$p<0.01$; ***$p<0.001$; ****$p<0.0001$.

surface. As a result, stability may be improved while transfection efficiency is often lost [94, 100]. Transfection and knockdown efficiency were not diminished with up to 2.5% PACE-PEG, however incorporation of 10% PACE-PEG into PACE-E2 polyplexes resulted in a decrease in cellular uptake of dye-labeled oligos that corresponded with a decrease in siRNA mediated IL-15 knockdown (**Figure 2.2E,F; Supplemental Figure A.2B,C**).

2.4.4 PACE-PEG-Maleimide Polyplexes

The E2 primary amine end group was found to be optimal in transfecting HUVECs relative to other PACE polymers. Polyplexes formulated with a blend of PACE-E2 and PACE-PEG were more stable and less cytotoxic than polyplexes made with PACE-E2 only, but delivered a weaker knockdown effect with siRNA. To further optimize a PACE delivery vehicle for delivery to the endothelium, we synthesized PACE-PEG-Maleimide (PACE-PEG-Mal or PP-Mal) as a tool for conjugating cell surface binding molecules such as antibodies to the surface of polyplexes, as described in Section 1.3 (**Figure 2.1D,E**). To validate PP-Mal as an effective polymer for forming polyplex delivery vehicles, we first characterized unconjugated polyplexes made with this polymer.

To generate polyplexes incorporating both PACE-E2 and PP-Mal, we blended the two polymers in DMSO (100 mg/mL) using either 3%, 10%, or 30% PP-Mal by weight prior to polyplex formulation. Blended PP-Mal/PACE-E2 polyplexes were between 70 – 100 nm in diameter, consistent with PACE-E2 polyplexes made without any PEGylated polymer (**Figure 2.3A**). Increasing PP-Mal content reduced the surface charge of polyplexes, with 30% PP-Mal/P-E2 polyplexes having a close to neutral zeta potential of +6 mV (**Figure 2.3B**). The hydrophilic PEG groups orient on the outer surface of the polyplex, shielding the cationic charge of the base PACE polymer.

Next, we measured the encapsulation efficiency of PACE-E2 polyplexes. PACE-E2 polyplexes exhibited high loading efficiency (98.6% encapsulation). Incorporation of up to 30% PP-Mal in PACE-E2 polyplexes did not significantly affect the encapsulation efficiency of siRNA relative to polyplexes made without any PP-Mal (**Figure 2.3C**). We evaluated the cellular uptake of unconjugated PP-Mal/PACE-E2 polyplexes by transfecting HUVECs with polyplexes loaded with a fluorescently labeled DNA oligo for 24 hours. The trend in percentage of cells having taken up polyplexes, gated based on untreated cells, was consistent between PP/PACE-E2 polyplexes and PP-Mal/PACE-E2 polyplexes (**Figures 2.2D and 2.3D**). As expected, increasing PP-Mal content resulted in a reduction of cellular uptake.

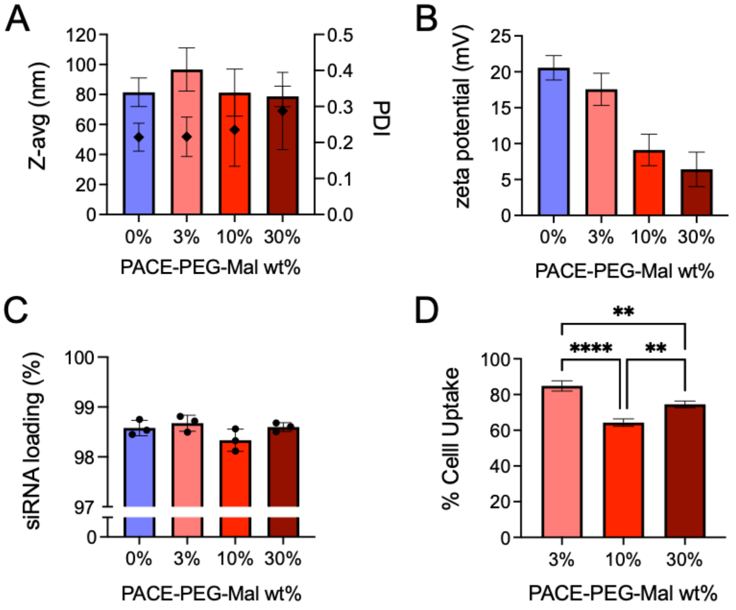

Figure 2.3: Forumulation of blended PACE-E2 polyplexes with PACE-PEG-Maleimide. **(A)** Hydrodynamic diameter (bars) and PDI (black diamonds) and **(B)** zeta potential of polyplexes formulated with blends of PACE-PEG-Mal and PACE-E2 polymers (0%, 3%, 10%, and 30% PP-Mal by weight) encapsulating siRNA against human IL-15. **(C)** siRNA loading of PACE-E2 polyplexes with varying PACE-PEG-Mal content. **(D)** Cellular uptake of PP-Mal/PACE-E2 polyplexes encapsulating dye-labeled oligo following 24 hours of treatment in static culture. **$p<0.01$; ****$p<0.0001$.

We observed a significant reduction in cellular uptake of 10% PP-Mal/PACE-E2 polyplexes relative to both 3% and 30% PP-Mal/PACE-E2 polyplexes. This correlated with a very slight reduction in loading with 10% PP-Mal (98.3%), however this reduction in loading is unlikely to account for the difference in uptake that we observed (**Figure 2.3D**).

While the percentage of cells having taken up 30% PP-Mal/PACE-E2 polyplexes remained fairly high (~75%) in this setting despite the addition of PEG, it should be noted that the uptake studies of non-conjugated polyplexes (**Figures 2.2, 2.3, and Supplemental Figure A.2**) are carried out with HUVECs exposed to polyplexes in static culture for a full 24 hours. A larger difference in uptake between polyplexes with different PEG content was seen at shorter time points. To better mimic a physiological setting in which ECs have only passing exposure to nanocarriers, uptake studies of Ab-Mb-conjugated polyplexes were performed by exposing HUVECs to Ab-Mb-polyplexes for only 2 hours in static culture followed by several washes to remove any unbound or loosely associated polyplexes. However, 2 hours was insufficient time to observe uptake of all non-conjugated polyplexes, so 24 hour time points were used to validate the delivery of non-conjugated polyplexes. Described further in Section 2.4.6, the ability to bind to and be taken up by cells after a brief exposure period (2 hours) demonstrates the benefits of antibody conjugation targeting the endothelium.

2.4.5 Conjugation of PACE-PEG-Maleimide/PACE-E2 Polyplexes Using Monobody Adapter

To conjugate EC targeting antibodies to the surface of PP-Mal/PACE-E2 polyplexes via the monobody adapter shown in **Figure 2.1E**, we adapted a method that was recently developed to conjugate the monobody adapter to the surface of poly(lactic acid)-poly(ethylene glycol) (PLA-PEG) nanoparticles [149]. Several modifications were made to accommodate the differences in polymer composition, size and stability between dye-loaded PLA-PEG nanoparticles and dye-labeled nucleic acid loaded PACE polyplexes, resulting in the conjugation protocol depicted in Figure **2.4A** and described in Section 2.3.4. For example, PLA-PEG nanoparticles can be pelleted by centrifugation at high speeds then redispersed in buffer in order to remove excess Mb and change the buffer, whereas we used centrifugal filters at lower speeds to prevent pelleting of polyplexes during these steps.

To evaluate the stability of the PP-Mal/PACE-E2 polyplexes throughout the conjugation protocol we measured the size, PDI, and surface charge by dynamic light scattering (DLS) at each step of the conjugation procedure (**Figure 2.4A**, DLS Samples 1-5).

30% PP-Mal/PACE-E2 polyplexes increase slightly in size throughout the conjugation procedure, with an increase in hydrodynamic diameter from 85 nm (fresh polyplexes) to 130 nm (following Mb binding and buffer exchange) (**Figure 2.4B**). There was no increase in size following the addition of either CD31 or isotype antibodies. Freshly prepared 10% PP-Mal/PACE-E2 polyplexes had a large PDI of 0.7, much larger than that of fresh

30% PP-Mal/PACE-E2 polyplexes. 10% PP-Mal/PACE-E2 polyplexes exhibited a more monodisperse population following Mb binding and buffer exchange, however after incubation with both CD31 and isotype antibodies, the size of the conjugated 10% PP-Mal/PACE-E2 polyplexes roughly doubled in size from 150 nm to 300 nm (**Figure 2.4B**). This may be due to aggregation of the polyplexes during the antibody binding incubation, however the PDI (black squares) and the size distribution plot indicate a monodisperse population as opposed to a small population of large aggregates. With both polyplex formulations, the PDI decreased over the course of the reactions. This could be due to the constant agitation during the hour-long incubation periods, or due to loss of small particles or large aggregates during the buffer exchange steps.

Both formulations of polyplexes had similar positive surface charges when freshly prepared, and the zeta potentials became more neutral over the course of the conjugation, possibly due to the accumulation of protein (Mb then Ab) on the surface of the polyplexes (**Figure 2.4C**).

Next we sought to assess whether conjugated Ab-Mb-polyplexes can be stored at 4°C for later usage, and to determine how long conjugated polyplexes remain stable under physiological conditions. Both CD31-Mb-polyplexes and Isotype-Mb-polyplexes made from a 30% PP-Mal/PACE-E2 starting formulation maintained a stable size with a low PDI for up to 72 hours shaking at 37°C in both PBS and PBS + 10% FBS, after which the polyplexes increased in size from ¡200 nm to ¡300 nm through day 8. (**Figure 2.4D**). After observing that the Ab-Mb-polyplexes remained intact for up to 8 days shaking at 37°C, we also tested the binding functionality of Ab-Mb-polyplexes after 24 hours or 8 days of storage (see Section 2.4.6).

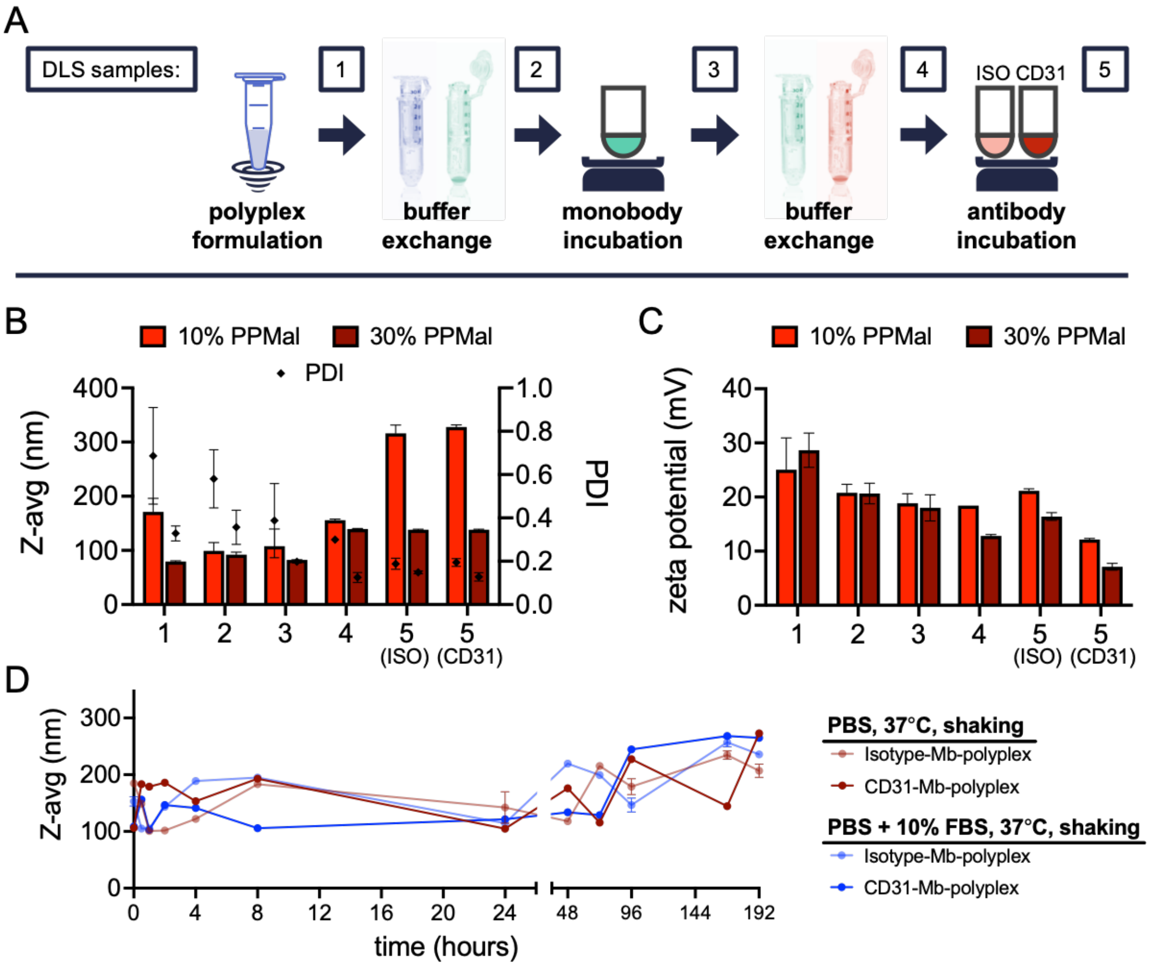

Figure 2.4: Conjugation of PACE-PEG-Maleimide/PACE-E2 Polyplexes Using Monobody Adapter. **(A)** Schematic overview of the reaction protocol developed for conjugating the C-terminal monobody cysteine to thiol reactive maleimide groups on the surface of PP-Mal/PACE-E2 polyplexes. Samples were collected for dynamic light scattering (DLS) measurements at steps 1 - 5. **(B)** Hydrodynamic diameter (bars) and PDI (black diamonds) and **(C)** zeta potential of either 10% or 30% PP-Mal/PACE-E2 polyplexes encapsulating Cy5-labeled DNA oligos throughout the conjugation procedure. Numbers along the x-axis correspond to DLS sample collection points labeled in **(A)**. **(D)** Stability of Ab-Mb-polyplexes over time at 37°C, shaking (350 rpm). Ab-Mb-polyplexes were resuspended at 1 mg/mL in either PBS (red lines) or PBS + 10% FBS (blue lines). At each time point, 40 μg of polyplexes was collected and diluted in 1 mL deionized water for DLS measurement.

2.4.6 Uptake of Endothelium-Targeted Polyplexes *in vitro* and *ex vivo*

We treated HUVECs with 0.1 mg/mL CD31-Mb-polyplexes or Isotype-Mb-polyplexes loaded with Cy5-labeled DNA oligo to evaluate the effect of Ab-Mb-conjugation on polyplex uptake by ECs. Cells were treated for 2 hours in complete medium at 37°C, then washed thoroughly to remove unbound or loosely associated polyplexes from the cells and analyzed by flow cytometry. Both 10% and 30% PP-Mal/PACE-E2 CD31-Mb-polyplexes were taken up significantly more than Isotype-Mb-polyplexes (**Figure 2.5A-C**). Cells treated with both 10% and 30% PP-Mal/PACE-E2 Isotype-Mb-polyplexes showed some uptake relative to untreated cells (**Figure 2.5A,C**), however CD31-targeting increased the mean fluorescence by 13-fold over Isotype-Mb-polyplexes with the 10% PP-Mal/PACE-E2 formulation and 9-fold over Isotype-Mb-polyplexes with the 30% PP-Mal/PACE-E2 formulation (**Figure 2.5B**). Formulating polyplexes with a higher PP-Mal content (30%) did not lead to increased cellular uptake compared to 10% PP-Mal/PACE-E2 polyplexes.

To test the functionality of the Ab-Mb-polyplexes following storage at 4°C or 37°C, we measured uptake of 30% PP-Mal/PACE-E2 Ab-Mb-polyplexes after 24 hours and 8 days of storage. Following overnight storage under all three conditions (4°C, 37°C shaking, or 37°C shaking + 10% FBS), 30% PP-Mal/PACE-E2 CD31-Mb-polyplexes maintained their binding specificity for ECs relative to Isotype-Mb-polyplexes, however the Ab-Mb-polyplexes that were stored in 10% FBS had significantly lower uptake than Ab-Mb-polyplexes stored in PBS (**Figure 2.5D**). We hypothesize that this is due to adsorption of serum proteins to the polyplex, blocking interactions between the attached antibodies and the EC surface proteins, as described in Section 1.3.2 (**Figure 1.8**).

After 8 days of shaking at 37°C, 30% PP-Mal/PACE-E2 CD31-Mb-polyplexes stored in PBS without FBS maintained specific binding to ECs relative to Isotype-Mb-polyplexes stored under the same conditions, however the fluorescence intensity of the transfected cells was much lower than the intensity that was seen with freshly conjugated Ab-Mb-polyplexes (**Supplemental Figure A.3**). This may have been caused by either loss of dye-labeled oligo from the polyplexes, bleaching of the fluorophore, or diminished binding of the CD31-Mb-polyplexes due to loss of antibody on the polyplex surface, or a combination of these factors. CD31-Mb-polyplexes stored in PBS + 10% FBS were not taken up by ECs, likely

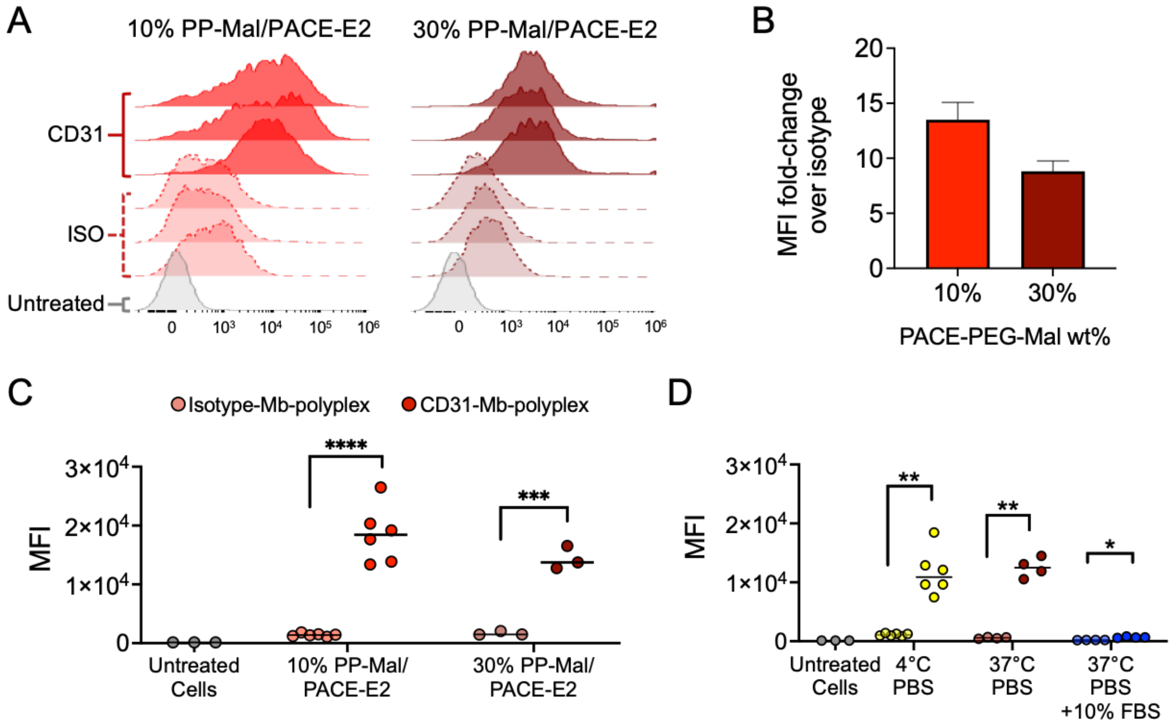

Figure 2.5: Uptake of endothelium-targeted polyplexes *in vitro*. **(A)** Flow cytometry histogram plots of Cy5 fluorescence intensity. 10% PP-Mal/PACE-E2 Ab-Mb-polyplexes are shown on the left in red, 10% PP-Mal/PACE-E2 Ab-Mb-polyplexes are shown on the right in dark red. CD31-Mb-polyplexes are in solid lines, Isotype-Mb-polyplexes are in dashed lines with lighter coloring. Untreated cells are shown in grey. **(B)** Fold increase in mean fluorescence intensity (MFI) between CD31-Mb-polyplexes and Isotype-Mb-polyplexes, error bars represent the SEM. **(C)** MFI of cells treated with 10% or 30% PP-Mal/PACE-E2 CD31-Mb-polyplexes or Isotype-Mb-polyplexes for 2 hours in complete media at 37°C. **(D)** MFI of cells treated with 30% PP-Mal/PACE-E2 Ab-Mb-polyplexes that had been stored under various conditions prior to cell treatments. 30% PP-Mal/PACE-E2 Ab-Mb-polyplexes were stored at 1 mg/mL in PBS or in PBS + 10%FBS at 4°C (static) or 37°C (shaking, 350 rpm) for 24 hours. Following storage, polyplexes were delivered to cells at 0.1 mg/mL final concentration for 2 hours in complete media at 37°C. Uptake of stored Ab-Mb-polyplexes was evaluated by flow cytometry. *$p<0.05$; **$p<0.01$; ***$p<0.001$; ****$p<0.0001$.

attributable to protein adsorption blocking Ab binding as described above (**Supplemental Figure A.3**).

To evaluate the effect of conjugating antibodies to the polyplex surface in a setting that better mimics the *in vivo* environment, we delivered Ab-Mb-polyplexes to human umbilical arteries using a recently developed isolated vessel perfusion system (IVPS) [123]. After perfusing the vessels with 0.1 mg/mL Ab-Mb-polyplexes for 1 hour at 37°C in complete media, we did not see a difference in uptake by vessel ECs between CD31-Mb-polyplexes and Isotype-Mb-polyplexes. Both the CD31-Mb-poyplex treated vessels and and Isotype-Mb-polyplex treated vessels had similar amounts of uptake as analyzed by confocal microscopy and flow cytometry (**Supplemental Figure A.4**). We observed that some regions of the endothelium that had sustained more damage during perfusion were brighter in the Cy5 channel, suggesting that either polyplexes or free dye was accumulating non-specifically on those regions. We hypothesize that free Cy5-labeled oligo or free excess Cy5 dye leaked out of the polyplexes during perfusion and accumulated on the vessel walls. Previously we had not seen any non-specific accumulation or uptake of free DNA on ECs *in vitro*, however the vessel lumen, and in particular areas of cell death, may be more susceptible to this non-specific interaction. Further investigations into using PACE polyplexes in the IVPS loop are proposed in Section 4.2.1.

2.5 Conclusion

We developed a polymeric nucleic acid delivery vehicle with enhanced transfection of human endothelial cells by combining three strategies: cell-specific antibody binding interactions, EC-optimized polymer end group chemistry, and a PEG coating that promotes stability and reduces cytotoxicity.

We found that PACE-PEG-Maleimide (PP-Mal) content affects the polyplex size and stability through conjugation, as well as the transfection efficiency of the resulting CD31-targeted Ab-Mb-polyplexes. However, increasing the amount of PP-Mal from 10% to 30% did not increase the uptake of CD31-Mb-polyplexes, suggesting that there is a point at which additional maleimide groups does not aid in either conjugation to the monobody adapter, or in binding of additional antibodies to the Mb-polyplex surface. Additional PP-Mal concentrations should be evaluated in order to determine the optimal maleimide content for cell surface targeting.

The monobody adapter technology can be used to bind any antibody. In the context of treating the endothelium, this enables careful selection of surface antigens based on organ specific EC phenotypes or disease-state specific antigen presentation on ECs. In addition, the monobody linker can be applied to any delivery vehicle with an exposed thiol reactive group. By changing antibodies and polymer blends, this targeting system can readily be adapted for use with PACE vehicles optimized for delivery to any organ. This makes the monobody adapter system compatible with the highly tunable properties of the PACE family of polymers.

We have demonstrated a significant benefit in cellular uptake with targeted polyplexes, compared to unconjugated or isotype-conjugated polyplexes, however the performance of these Ab-Mb-polyplexes in *ex vivo* or *in vivo* settings should be further explored. In addition, an in-depth analysis of polyplexes formulated with different combinations and concentrations of each of the end group modified PACE polymers and PACE-PEG-Mal is needed in order to apply this technology more broadly.

Chapter 3

A Digital Pathology Tool for Quantification of Color Features in Histologic Specimens

The work described in this chapter was done in collaboration with Jenna DiRito, PhD. This chapter is adapted from Reschke & DiRito et. al., 2021 [32].

3.1 Abstract

In preclinical research, histological analysis of tissue samples is often limited to qualitative or semi-quantitative scoring assessments. The reliability of this analysis can be impaired by the subjectivity of these approaches, even when read by experienced pathologists. Furthermore, the laborious nature of manual image assessments often leads to the analysis being restricted to a relatively small number of images that may not accurately represent the whole sample. Thus, there is a clear need for automated image analysis tools that can provide robust and rapid quantification of histologic samples from paraffin-embedded or cryopreserved tissues. To address this need, we have developed a color image analysis algorithm (DigiPath) to quantify distinct color features in histologic sections. We demonstrate the utility of this tool

across multiple types of tissue samples and pathologic features, and compare results from our program to other quantitative approaches such as color thresholding and hand tracing. We believe this tool will enable more thorough and reliable characterization of histological samples to facilitate better rigor and reproducibility in tissue-based analyses.

3.2 Introduction

Histological analysis of tissue biopsies–either formalin-fixed, paraffin-embedded (FFPE) or cryopreserved—remains a cornerstone of preclinical research [150, 151, 152, 153, 154]. Nevertheless, there are well acknowledged issues with the reliability of the standard semi-quantitative assessments typically performed on these samples [151, 155, 156]. These issues can potentially be circumvented in clinical settings by carefully controlled workflows that ensure consistency in sample preparation and reduce inter-observer variability [157]. However, replicating these conditions in preclinical research often presents a variety of challenges depending on the nature of the analysis to be performed and whether the researchers have access to an expert pathologist [153].

Even if researchers have access to a trained pathologist, the volume of tissue typically involved in preclinical research can make manual analysis of each individual image impractical. Studies in animal models with large numbers of replicates can yield an overwhelming abundance of tissue. Similarly, studies utilizing non-transplanted human organs—an area of emphasis in our laboratory—require evaluation of large amounts of tissue per organ in order to properly characterize these highly heterogenous samples. In two recent examples, we evaluated 1000's of images collected from dozens of biopsies [31, 124]. In these instances, manual forms of color image analysis—where the researcher must evaluate each individual image one by one—are simply not feasible.

Digital color thresholding is a commonly used method to automate the analysis of features of interest in color images of histologic samples [153, 158, 159, 160]. In these methods, a threshold value is identified for each of the three RGB (Red, Green, and Blue) color channels to isolate a specific subset of color shades. However, color features in standard histologic stains (e.g. hematoxylin and eosin, H&E) are typically blended shades of the three RGB colors. As a result, what is visually distinct to the eye can be difficult or even impossible to isolate using a simple color thresholding approach. To overcome this limitation, more sophisticated approaches have been developed that can identify single features of interest within specific stains [161, 162, 163]. While useful for certain focused applications, these approaches are limited by their lack of adaptability to any color feature of interest regardless of histochemical stain. Thus, there remains a need for software that has the efficiency and reproducibility of the existing automated methods but is also easily adaptable to many different types of histological features and stains within a single workflow.

The aim of this work was to address the need for more rapid, reliable and adaptable methods of digital analysis in histological specimens. To that end, we developed and validated an automated image analysis approach (DigiPath) that uses a color-based classification algorithm to identify and rapidly quantify areas of interest in color images. We demonstrate that this approach is accurate, reliable and significantly faster than a standard method of hand tracing areas of interest. We also show that it can be used for assessment of a wide array of different histological features in human and animal biopsy specimens. Based on the evidence presented here, we believe DigiPath can enable comprehensive, reproducible, and rapid analysis of histology specimens in preclinical research.

3.3 Materials and Methods

3.3.1 Organ Retrieval and Storage

All non-transplanted organs were provided under an existing research protocol with New England Donor Services (NEDS) after obtaining research consent from the donor families. In the U.S., since the donor is deceased, this research is not considered human subject research as defined in the HHS Policy for Protection of Human Research Subjects 45 CFR 46.102. HIPAA is still invoked with these specimens and all organs used have been de-identified. After in situ flushing of the abdominal organs with either cold University of Wisconsin or Custodial Histidine-Tryptophan-Ketoglutarate (HTK) preservation solution, organs were procured, packed in ice, and placed in static cold storage prior to experimentation per standard clinical practice.

3.3.2 Kidney Normothermic Machine Perfusion

Kidneys were prepared and perfused for one hour on the *ex vivo* normothermic machine perfusion circuit as previously described [164]. Biopsies were collected at the end of the perfusion period.

3.3.3 Biopsy and Staining Procedures

Wedge biopsies were collected and fixed in 10% formalin for a minimum of 24 hours. Formalin fixed biopsies were paraffin embedded, sectioned to 4 µm, and stained with either hematoxylin and eosin (H&E), Sirius red, martius scarlet blue (MSB), or terminal deoxynucleotidyl transferase dUTP nick end labeling (TUNEL) stain in the Yale Histology laboratory. Immunofluorescent TUNEL staining was performed on 6 µm cryosections using the In Situ Cell Death Detection Kit, TMR red (Sigma).

3.3.4 Mouse Model of Steatohepatitis

C57BL/6J mice were from the National Cancer Institute as previously described [165]. All experiments were performed in specific pathogen-free facilities and were performed in accordance with the regulations adopted by the National Institutes of Health (NIH) and approved by the Animal Care and Use Committee of the Yale University. Eight-week old male C57BL/6J mice were placed on a high-fat diet (HFD; 45% fat, D12451 Research Diets) or chow as a model for steatohepatitis and chronic liver injury. After 10 weeks of a HFD animals were given a vehicle or digoxin at multiple dosages (low - 0.125 mg/kg, medium - 0.5 mg/kg, high - 2.5 mg/kg) twice a week by gavage feeding and continued with HFD feeding for a total of 15 weeks. At the end of the protocols, whole livers were collected for histological analysis and stained with H&E. Images were collected at 10X magnification in the Ouyang Laboratory.

3.3.5 Brightfield Imaging

Three sections per biopsy were tiled at 20x magnification using an EVOS FL Auto 2 microscope (ThermoFischer Scientific). All new images were captured as 24-bit RGB color images with 3.2 million pixels (12 MB) at a resolution of 58522 pixels per inch. Following image collection, images were manually parsed into “edge” versus “continuous” images to distinguish images that were wholly contained within the section (continuous) versus images that were partially tissue and partially blank space (edge). Edge images were excluded to avoid artifacts in analysis. Continuous images were then loaded into the program for quantification.

3.3.6 Hand Tracing Analysis

Users generating the hand tracing results were given explicit instructions on how to use the Freehand selections tool in ImageJ. While hand tracing each image, users recorded their screens for accurate measurements of the time it took to do each image analysis. After hand tracing each image, users measured the areas and created binary masks of their outlines.

3.3.7 Color Threshold Analysis

Images were opened in ImageJ. The ‘Threshold Color’ window was opened, and a set of Red, Green, and Blue thresholds was chosen in Red/Green/Blue (RGB) space using the default thresholding method. The selection was converted to a binary mask, which was saved for evaluating accuracy relative to hand tracing.

3.3.8 DigiPath Program

The DigiPath custom program was developed in MATLAB (Version R2019b; The Mathworks, Inc. 2019) with the Image Processing Toolbox (The Mathworks, Inc. 2020) installed. The complete code, entitled 'DigiPath.mlapp', is available as a packaged app on Mathworks.com, and in the Supplemental Materials.

3.3.9 Image Analysis Using Custom MATLAB Program

After eliminating edge images from each experimental set of 24-bit color images, two to four training images that were representative of any variations in staining were selected by the user. The images analyzed in this study had 800,000 pixels (3 MB per image; **Figures 3.1, 3.2**), 1.4 million pixels (5.3 MB per image; **Figure 3.4**), or 3.2 million pixels (12 MB per image; **Figures 3.3, 3.5**). The program was initiated, and positive and negative regions were selected as prompted by drawing polygons of any shape and size on the displayed training images. The complete image set was run through the algorithm using the Color Map and Positive Color List generated in the training steps. Binary mask overlays of regions the program had identified as positively stained were reviewed visually. Images for which the program-determined regions did not line up with visually identifiable features were run through the program a second time using an updated Color Map and Positive Color List. Results are represented by plotting the percent of the image area with positive staining. Each point represents one image field within a biopsy. The significance of differences between biopsies was calculated using one-way ANOVA.

3.3.10 Evaluation of DigiPath Performance

Area of microvascular obstructions was quantified in six 20X images of kidneys stained with H&E using three quantitative methods: hand tracing, color thresholding, and DigiPath analysis. A set of three independent users analyzed the same six images using each method. A consensus hand-traced standard was generated for each image by including areas that were selected by all three users. This was used as a standard for comparison to areas found by color thresholding or DigiPath. A confusion matrix was generated where the hand-traced classification of the images served as the 'true' positive and negative values, and the classification by color thresholding or DigiPath were positioned as the 'predicted' positive and negative values. Metrics including sensitivity, specificity, and accuracy were calculated from each matrix. Three correlation coefficients, F-score, Matthew's Correlation Coefficient (MCC), and Youden's J Statistic, were calculated to assess the performance of the color thresholding and DigiPath methods in the hands of each independent user. The significance of differences between methods was calculated using two-way ANOVA.

3.3.11 Correlation Metrics

Three correlation metrics were derived from a confusion matrix of all possible classification outcomes (FP – false positives, FN – false negatives, TP – true positives, and TN – true negatives). Youden's J Statistic represents 'informedness' – the probability that the program will make an informed decision [166]. This takes into account both sensitivity and specificity.

$$J = \frac{TP}{TP+FN} + \frac{TN}{TN+FP} - 1 = sensitivity + specificity - 1$$

The F-score is a measure of accuracy and is derived from sensitivity and precision values [167].

$$F = \frac{2TP}{2TP+FP+FN} = 2 \times \frac{precision \times sensitivity}{precision + sensitivity}$$

MCC is a measure of both markedness and informedness and accounts for the proportion of occurances of each possible classification outcome [168, 169, 170].

$$MCC = \frac{TP \times TN - FP \times FN}{\sqrt{(TP + FP)(TP + FN)(TN + FP)(TN + FN)}}$$

3.3.12 ImageJ Quantification

Immunofluorescent TUNEL images were processed using the Watershed and Analyze Particles functions in ImageJ. The total number of DAPI positive (blue) and TUNEL positive (red) cells were quantified.

3.4 Results

3.4.1 DigiPath Yields More Efficient Results When Compared to Hand Tracing Methods

Hand tracing is frequently used as a standard method to quantify areas of interest in IHC stained tissue sections from pre-clinical biopsy specimens. We therefore compared DigiPath to traditional hand tracing as a gold standard. Three independent users were asked to quantify areas of microvascular obstruction in human kidney biopsies that underwent normothermic machine perfusion (NMP) using both hand tracing in ImageJ and DigiPath. These microvascular obstructions (not classic thrombi) are structures unique to the serum free perfusate conditions of NMP and are easily identifyable on histology [31]. With DigiPath, we observed that features were systematically 1-3% smaller as compared to hand tracing. This result is consistent with a small and systematic over estimation of size by users when hand tracing features (**Figure 3.1A** and **Figure A.5**). We also found that images with more positive area (e.g. Image 4) were subjected to higher inter-user variability (21% error of the mean) with either method (**Figure 3.1B**). Nevertheless, there was general agreement in quantified area between hand tracing and DigiPath methods (**Figure 3.1B**). Although inter-user variability was observed, we found that each user reported similar relative trends in the amount of positive area (i.e. User 1 values < User 2 values < User 3 values).

While DigiPath produced similar results to hand tracing, we found that DigiPath significantly reduced the time of analysis. To quantify 5 images by hand, users took on average 98.5 ± 80.3 minutes. However, when using DigiPath to quantify those same 5 images, users took on average 7.6 ± 1.7 minutes in total. This number includes the time it took users to set parameters in training images and process images of interest. A repeated measure mixed-model two-way ANOVA showed that the method of analysis (i.e. DigiPath vs. hand tracing) significantly affected cumulative analysis time (**Figure 3.1C**). We also conducted a Bonferroni multiple comparisons test to evaluate the difference in cumulative analysis times between DigiPath and hand tracing at each image number up to 5 images. Due to the high variability between users in the hand tracing analysis time, at 5 images the difference in cumulative analysis time between DigiPath and hand tracing was not statistically significant (p=0.062). However, we observed a trend of decreasing p values between DigiPath and hand tracing as the number of images increased (3 images: p=0.613, 4 images: p=0.098, 5 images: p=0.062).

We next extrapolated how long it might take to analyze 500 images, a typical number of images in our prior studies, we estimate that we would save at least ~167 hours of quantification time compared to hand tracing (**Figure A.6**). Analyzing 500 images by hand tracing is unrealistic and would be unlikely to be carried out in a study. Nonetheless the extrapolation from the average hand tracing time per image provides a conservative estimate of the amount of time that can be saved by quantifying color image features with DigiPath. It also demonstrates how DigiPath analysis can enable a far more in-depth quantitative analysis than is practical with a manual approach.

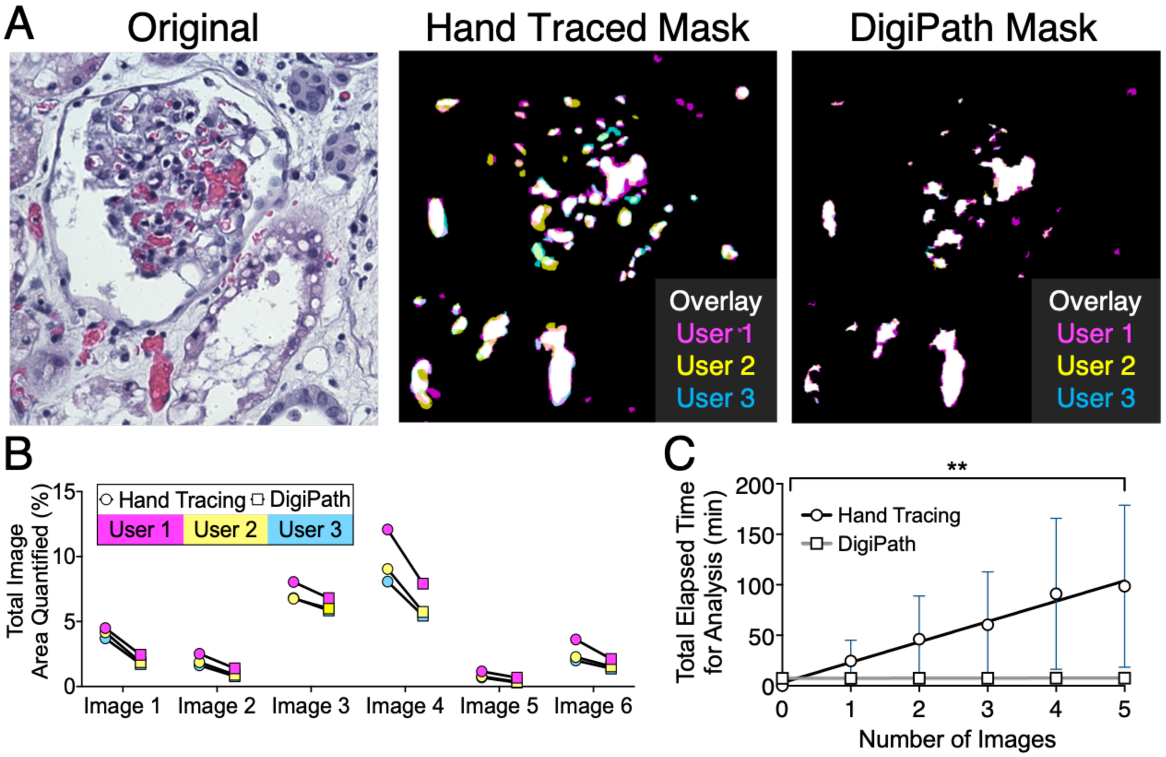

Figure 3.1: DigiPath is a more efficient method for quantification than hand tracing. **(A)** Representative image from an H&E section of a kidney during NMP. Obstructions are quantified using hand tracing or DigiPath by three individual users (User 1 – magenta, User 2 – yellow, User 3 – cyan). **(B)** Total area quantified using hand tracing or DigiPath methods from three users. **(C)** Total time elapsed for hand tracing (circles, black line) or DigiPath (squares, gray line) methods across three users for 5 separate images. Mixed-model ANOVA showed a significant difference between the DigiPath and hand tracing cumulative analysis times (**p=0.0027).

3.4.2 DigiPath Achieves Greater Correlation With Hand-Traced Standards Than Color Thresholding

Standard thresholding methods - which pick a specific threshold value of intensity for each of the three colors to distinguish between feature versus background - are reliable only under conditions where the pathologic features are predominantly a single distinct color (Red, Green, or Blue). However, typical pathologic features (and tissue backgrounds) are mixes of the individual Red, Green, and Blue color channels meaning that cannot be easily separated this way without either setting the threshold too high (leading to high false negative rates) or setting the threshold too low (leading to high false positive rates). To compare the accuracy of DigiPath to a standard color thresholding approach, three independent users quantified a set of six images using both DigiPath and color thresholding in ImageJ.

The results from both DigiPath and standard thresholding were analyzed against a hand-traced standard. We found that the color thresholding method resulted in a tradeoff between sensitivity (accurate inclusion of all positive regions) and specificity (accurate exclusion of all negative regions). This effect can be seen in the image masks generated from the thresholding results; at the same color threshold setting, some microvascular obstructions are undercounted whereas other areas with no obstruction are incorrectly counted (**Figure 3.2A**). Conversely, DigiPath improved sensitivity in identification of positive areas without significantly impacting the exclusion of negative areas.

DigiPath showed greater overall correlation to hand-traced standards than color thresholding by three metrics: Youden's J Statistic (J-score), F-score, and Matthew's Correlation Coefficient (MCC). Each of these metrics are derived from a matrix of all possible classification outcomes (false positives, false negatives, true positives, and true negatives) and are commonly used to analyze the performance of binary classifications [169]. Across three users, DigiPath consistently classified regions of microvascular obstruction in kidneys with significantly greater correlation to hand-traced standards than was achieved using color thresholding (**Figure 3.2B**).

3.4.3 DigiPath Enables Quantification of Multiple Histological Features Across Different Stains

We next sought to assess the adaptability of DigiPath for quantification of a variety of different histological features between liver and kidney. We first assessed the ability of DigiPath to quantify the degree of steatosis in a series of 3 transplant-declined human livers (**Figure 3.3A**). Livers 1 and 2 were declined for transplant due to the presence of steatosis, whereas Liver 3 did not list steatosis as a reason for decline (**Table 3.1**). We used DigiPath to quantify the area of fat droplets in biopsies from each liver. DigiPath identified fat droplets

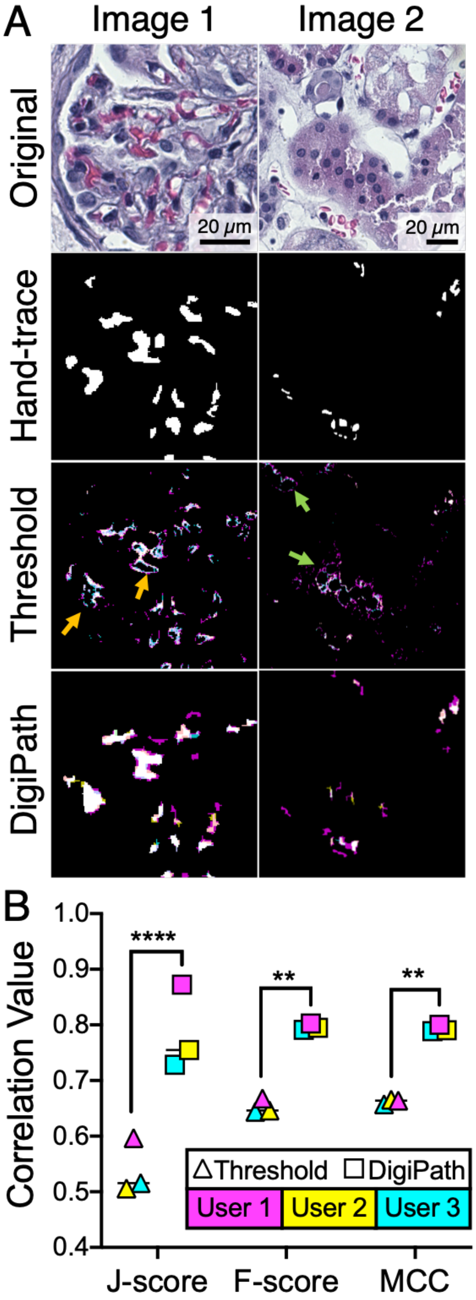

Figure 3.2: DigiPath achieves better correlation with hand-traced standards than color thresholding. **(A)** Representative images of a human kidney section stained with H&E. Masks of microvascular obstructions were generated by hand tracing (a composite of three independent user tracings), color thresholding and DigiPath (overlays of three independent users: User 1 – cyan, User 2 – yellow, User 3 – magenta). Areas of undercounting (orange arrows) and overcounting (green arrows) from color thresholding are shown. **(B)** F-score, Matthews Correlation Coefficient (MCC) and Youden's J Statistic were calculated to measure the correlation of results from thresholding and DigiPath methods with the hand-traced standard. Lines represent median. $^{**}p<0.01$; $^{****}p<0.0001$. Scale bars, 20 μm.

in both Livers 1 and 2, and negligible droplet area in Liver 3 (Liver 1 median: 29.2%; Liver 2 median: 9.3%; Liver 3 median: 0.7%). Steatosis is reported as the cumulative area of fat droplets per image area (**Figure 3.3A**). DigiPath also allows quantification of the variability of steatotic areas within a single biopsy. We used DigiPath to analyze over 400 20x images covering two sections of a biopsy from liver 1 and found that the percent steatotic area in individual image fields ranged from less than 1% to over 60%, with a median of 29% steatosis (**Figure 3.3A**). This demonstrates the capability of DigiPath to characterize the spatial variation of histologic features within a whole biopsy.

Similarly, we found that we could quantify the distribution of fibrosis in livers using the DigiPath tool on Sirius red stained biopsies. With Sirius red, high collagen levels, associated with fibrosis, stain red in fibrotic and cirrhotic samples. We assessed two livers with stage 2 fibrosis (Liver 4 median: 10.1%) or no diagnosis of fibrosis (Liver 5 median: 0.3%) (**Figure 3.3B**) for levels of Sirius red staining. Donor demographics are displayed in **Table 3.1**.

We next assessed how reliably DigiPath could quantify the same feature identified with two different stains. To test this, we quantified microvascular obstructions in a perfused kidney (Kidney 1; **Table 3.2**) using both H&E and MSB stains prepared on sequential sections (**Figure 3.3C**). Serial sections of a kidney biopsy were stained with either H&E or MSB in order to compare the results from both stains on nearly identical tissue sections. Microvascular obstructions appeared to have similar distributions between the two stains (**Figure 3.3C**). According to a Mann-Whitney test, there were no statistical significances between H&E and MSB stained sections. Slight differences in median values may be attributed to the variance of features observed in serial sections and the location of individual fields captured when tiling whole sections.

3.4.4 DigiPath Quantifies Steatosis in Experimental Mouse Livers

To confirm that DigiPath could quantify features of interest from histological specimens processed outside of our lab, we next sought to determine if DigiPath could accurately

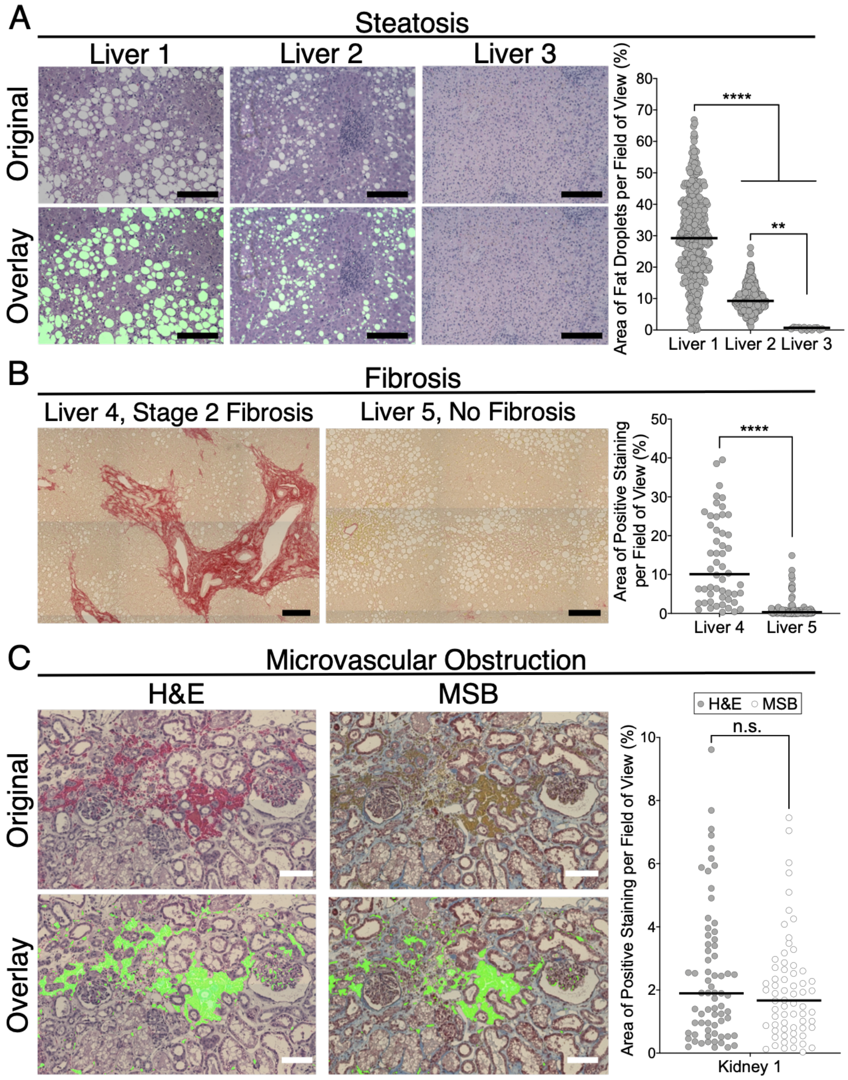

Figure 3.3: DigiPath enables quantification of multiple histological features across different stains. (A) Representative 20x image fields of three livers with varying degrees of steatosis. Scale bars, 200 µm. Quantification by DigiPath of steatotic area per image field on the right. **(B)** Representative images of tiled liver biopsies stained with Sirius red. Scale bars, 200 µm. Quantification of Sirius red staining displayed on the right. **(C)** Representative images of perfused kidneys stained with either H&E (left) or MSB (right). Scale bars, 100 µm. Overlays show area quantified in a single image. Distribution of positive staining quantified with DigiPath is shown to the right. Each dot represents one field of view. Lines represent the median. Differences between groups are not significant (n.s.) according to a Mann-Whitney test.

quantify previously published results [165]. In a model of murine hepatosteatosis, DigiPath was able to quantify the area of steatosis across a series of images from different animals (**Figure 3.4**). DigiPath quantification also confirmed the previously published result that treatment with oral Digoxin reduces hepatosteatosis in mice (**Figure 3.4B**) [165]. These

Table 3.1: Human Liver Demographics.

Liver	Age	Donor Type	Cause of Death	Reason for decline
Liver 1	50	DBD	Cerebrovascular accident (CVA)	Macrovesicular steatosis ~50% with evidence of NASH
Liver 2	57	DCD	Arrest from presumed electrolyte abnormalities with pancreatitis	Older DCD with alcohol history, steatosis on imaging and abnormal LFTs (peak bili 1.9)
Liver 3	36	DCD	Anoxic arrest (respiratory arrest 2/2 secretions -> cardiac arrest)	Slow to progress (Extubated 8:55, arrest 9:39, flush 10:13)
Liver 4	49	DBD	CVA witnessed at work, progressed to brain death over days with aggressive care	40-45% macrovesicular steatosis, moderate inflammation, and stage 2 fibrosis
Liver 5	29	DCD	Known brain aneurysm undergoing elective completion stent assisted coiling with intra-op aneurysm rupture early March. Complex course with acinetobacter in CSF, vasospasm and arrhythmias	Transaminases sharply rising in 2-5k range on 3/14, peaked and coming down

Table 3.2: Human Kidney Demographics.

Kidney	Age	Donor Type	Cause of Death	Reason for decline
Kidney 1	39	DBD	overdose	suspected malignancy
Kidney 2	70	DBD	history of hypertension and diabetes	stroke
Kidney 3	70	DBD	history of hypertension and diabetes	stroke

results demonstrate DigiPath's utility to quickly and accurately quantify areas of interest across treatment groups in preclinical research models. Additionally, DigiPath's ability to quantify specimens in different species and with variable sample preparations further demonstrates the value of this tool in the pre-clinical research setting.

3.4.5 DigiPath Reveals Patterns of Cell Death in Kidney Biopsies During Cold Storage

To evaluate DigiPath in a novel application, we assessed the degree of cell death in non-transplanted human kidneys during the course of cold storage (Kidneys 2,3; **Table 3.2**).

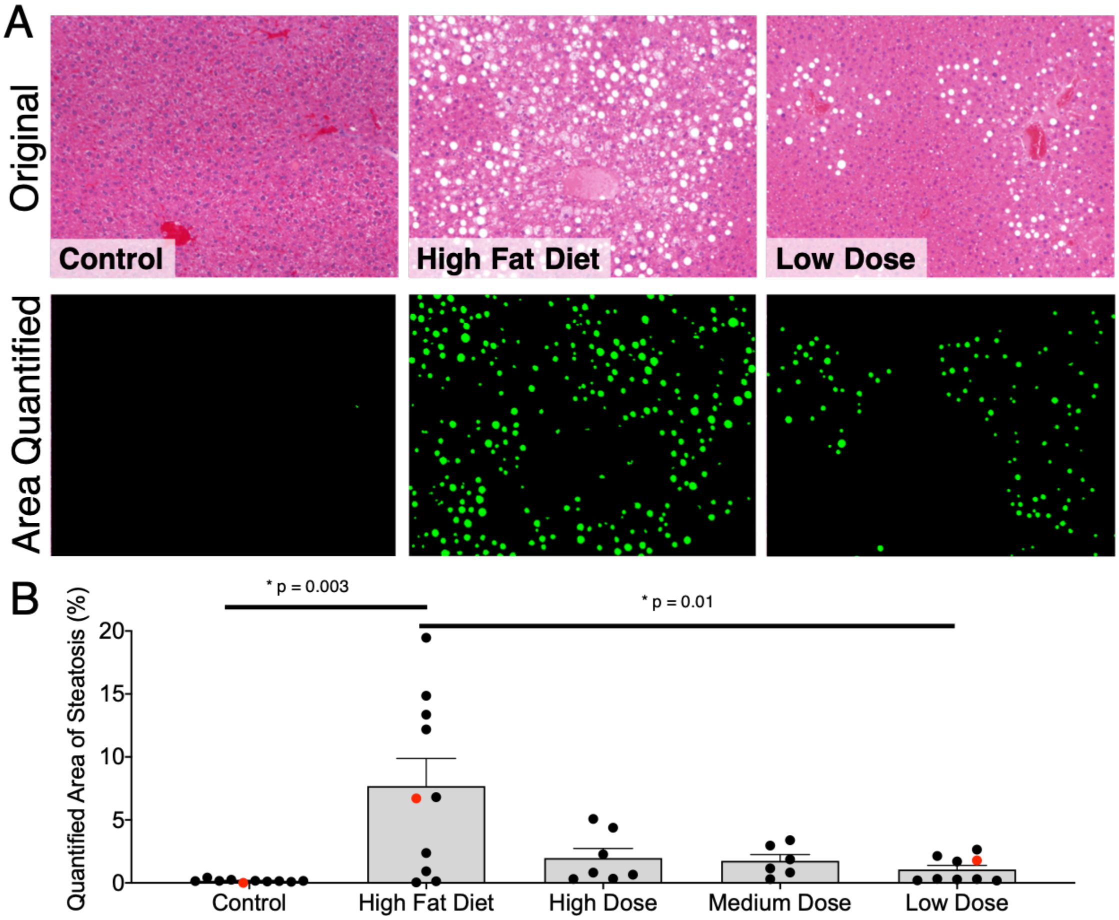

Figure 3.4: DigiPath quantifies experimental model of mouse hepatosteatosis. (A) Representative images of tissue from mouse livers on a standard diet (Control; left), High Fat Diet (middle), or High Fat Diet with a Low Dose of oral Digoxin (right). Area quantified with DigiPath is shown in green. **(B)** Quantification of steatotic area in murine models of hepatosteatosis with variable doses of Digoxin. Control group was fed standard chow. Each dot represents an individual image. Red dots correspond to images in **(A)**. Error bars represent the standard error of the mean. Differences between groups are significant according to a student's t-test.

Based on findings in a recently completed study, we hypothesized that cell death may be occurring during the course of cold storage in some marginal human organs [31]. We applied TUNEL staining to biopsies collected from a pair of kidneys after 6, 12, 18, 24, 30, 36, 48, 60 and 72 hours of cold storage (**Figure 3.5**). DigiPath was able to detect both TUNEL-positive (brown) and TUNEL-negative (blue) cells (nuclei) in each image (**Figure 3.5A**). This enabled us to quantify the amount of TUNEL staining normalized to the total cell density in each image (**Figure 3.5B**).

We observed a significant increase in TUNEL staining area normalized to the TUNEL negative cell area from 6 hours to 72 hours of cold storage in both kidneys (**Figure 3.5B**). The left kidney had a greater proportion of TUNEL positive cells than the right kidney at 72 hours (Left median: 0.16 brown:blue area ratio; Right median: 0.11 brown:blue area ratio; $p<0.0001$). We found that quantification of dead cells in ImageJ using immunofluorescent TUNEL staining yielded similar trends. At 6 hours of cold storage we observed <1% TUNEL positive cells. At 72 hours of cold storage, we quantified a median of 62.4% and 13.7% TUNEL positive cells in the left and right kidneys respectively (**Figure 3.5C,D**). We then used DigiPath to quantify TUNEL staining in biopsies taken at intermediate time points and found that both organs had a small early spike in cell death at 12-18 hours, followed by a larger increase in cell death beginning at 30-36 hours and continuing up to 72 hours (**Figure A.8**).

3.5 Discussion

Quantitative analysis of histological samples poses a significant challenge due to the nature of color images as an overlay of Red, Green, and Blue channels. While tissues stained with immunofluorescence can be evaluated by measuring each target in its individual color channel, nearly all features in a color image are made up of a mixture of three colors. As a result, histological features that are easily identifiable by eye are difficult to encode as a set of computational rules that an automated program can use to accurately detect features. Despite the difficulty of generating quantitative results from histology slides, they remain an important and highly used element of pre-clinical research.

To address this need, we have developed the DigiPath program which is a color-based classification algorithm that facilitates rapid and reliable quantification of histology features (**Figure A.7**). DigiPath can be used to quantify stained features in any RGB color image. It is particularly advantageous in pre-clinical research settings with large sample numbers, as

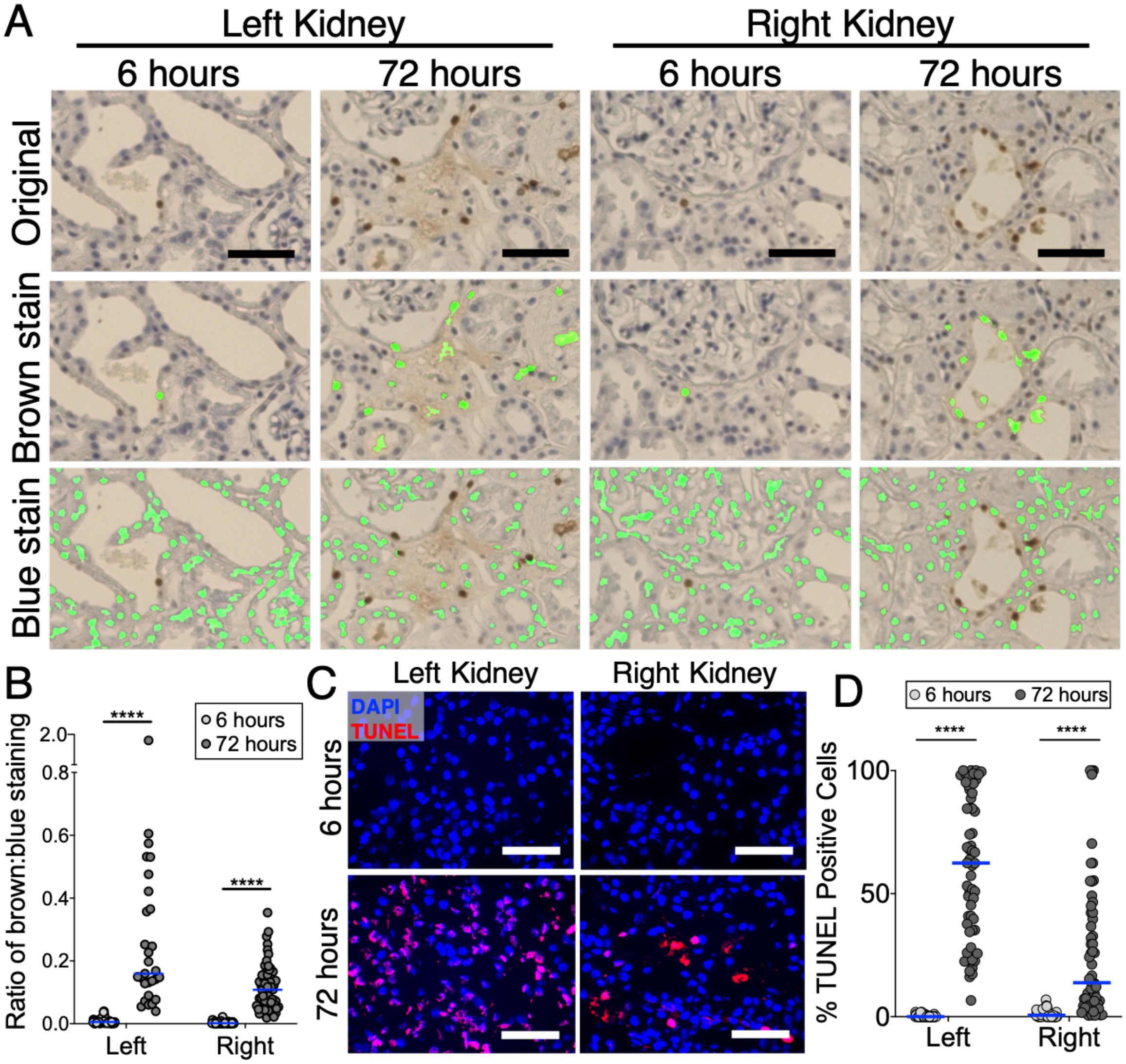

Figure 3.5: DigiPath reveals patterns of cell death in kidney biopsies during cold storage. **(A)** Representative images of Left and Right kidneys stained with TUNEL assay after 6 or 72 hours on cold storage. Overlays show area quantified after training DigiPath to recognize TUNEL-positive (brown) or TUNEL-negative (blue) cells. Scale bars, 50 µm. **(B)** Quantification TUNEL staining in Left and Right kidneys at the beginning and end of cold storage using DigiPath. In **(B)** the ratio of TUNEL-positive (brown) cell area to TUNEL-negative (blue) cell area is plotted. **(C)** Representative images from immunofluorescence TUNEL staining are presented (Red – TUNEL; Blue – DAPI). Scale bars, 50 µm. **(D)** Quantification of TUNEL staining in Left and Right kidneys at the beginning and end of cold storage using immunofluorescence. In **(D)** the number of TUNEL positive cells are divided by the number of DAPI cells. Each dot represents one field of view within the biopsy. Lines represent the median. $****p<0.0001$.

it enables high-throughput, quantitative assessment of unlimited numbers of high-resolution images. To quantify features of interest in the biopsies presented here, we captured 20x fields of view covering the entire biopsy. This resulted in up to 400 images per biopsy, depending on the biopsy size. In this study, we analyzed 25 whole biopsies for a total of over 1,800 images. Assessing this quantity of data by hand is simply not feasible regardless of access to a trained pathologist. In addition, DigiPath also allows researchers to access more nuanced information about the spatial heterogeneity of pathologic features. This added information can enable a more comprehensive characterization of pathologies (e.g. hepatic steatosis) both within and between biopsies.

DigiPath is a classification algorithm that makes decisions based directly on the categorization of pixel colors assigned during the training as ‘positive’ or ‘negative’. Since a typical image contains millions of pixels, selecting positive and negative regions on a few images generates classification data from hundreds of thousands of pixels. This approach allows a large training set of pixel color data points to be generated from a relatively small number of training images and further enables rapid implementation of DigiPath into a research workflow. DigiPath is therefore distinct from more broadly encompassing machine learning approach which require extensive training data sets of manually annotated images in order to account for all possible staining variability. However, for this approach to be effective, all images to be analyzed must share the same basic color palate. Thus we recommend that users run a new training set for each batch of samples to be analyzed; this ensures consistency in the color of pathologic features between the training images and images intended for quantitative analysis.

There are some limitations of DigiPath in its current iteration. As noted, applications of DigiPath are currently limited to features that can be defined solely by color. The DigiPath user-interface provides options for filtering features by size, however histological analyses that rely solely on morphology and do not employ distinguishing color stains cannot be performed using DigiPath. Hands-on analysis time using DigiPath is greatly reduced relative to hand tracing, however hands-on time may increase if samples collected in a study were stained on different days or in different facilities, likely requiring separate training runs for each biopsy.

While many potential sources of color variation can be controlled within a study (e.g image collection settings, tissue thickness, staining procedures), there may be some experimental variables that introduce differences in staining between samples that cannot be avoided. For example, the histological appearance of a feature of interest may appear differently in different species. If the researcher is comparing the same feature across different species, DigiPath results may not be directly comparable between species. Nevertheless, DigiPath can accommodate many other variable image properties including different tissue thicknesses and different magnification levels, as long as the training image set is consistent with the images to be analyzed. DigiPath can also analyze images of any size, depending on the memory limits of the user's computer. This is comparable to other commonly used image analysis software such as ImageJ.

Recent publications have described automated color image analysis methods developed for specific applications, including blood vessel segmentation and determination of differentiation potential of mesenchymal stem cells [161, 163]. Other automated color image analysis programs have been developed to detect specific stains, such as diaminobenzidine [162]. Like DigiPath, these examples detect features based on color. However, DigiPath's versatility allows a researcher to use a single tool for a broad range of color-based quantification applications. There are a number of programs with image analysis tools available for download. ImageJ (imagej.nih.gov/ij) is widely used in biomedical research to view, edit, and analyze both fluorescent and color images [158, 160, 161, 162, 163, 171, 172, 173, 174]. In this study we used ImageJ's Color Threshold feature and found that this method consistently resulted in lower correlation with hand-traced standards compared to DigiPath. QuPath is a recently developed open source image analysis software and a powerful tool for whole slide image analysis [175]. Other free downloadable image analysis programs include CellProfiler (cellprofiler.org), BioImageXD (bioimagexd.net), and Advanced Cell Classifier (cellclassifier.org) [176, 177, 178]. However the descriptions of these programs focus on applications for confocal or fluorescent images, while color image analysis is not emphasized, if described at all. To our knowledge, there are no comparable open-access programs available for color image analysis. Thus, we believe DigiPath's adaptability, ease of use, and transparent classification algorithm make it a useful tool for preclinical researchers seeking rapid quantitative analysis of histologic samples.

3.6 Conclusion

DigiPath is a highly adaptable tool that enables high-throughput, quantitative analysis of any color-defined histologic feature. DigiPath is available for download as a free app in the MATLAB File Exchange (www.mathworks.com/matlabcentral/fileexchange). The app is accessible to researchers regardless of their level of experience with coding and can be operated by users who are not formally trained in pathology. The ability to automatically detect features in histology images based on three-channel RGB color data enables a more quantitative approach to histological analysis, an experimental technique that is already essential in pre-clinical research.

Chapter 4

Conclusions and Recommendations for Future Work

4.1 Conclusions

In this dissertation we discussed homeostatic and pathological properties of the endothelium and described methods for delivering therapeutics to this distributed tissue network. In particular we focused on gene delivery and the potential for modulating expression of proteins involved in acute inflammation. We explored the potential of affinity based targeted delivery vehicle systems to enhance delivery of therapeutic cargos to the endothelium under physiological conditions.

In Chapter 2 we explored the PACE family of cationic polymers for gene delivery applications. We developed new functionalities of PACE polyplexes, which are nucleic acid-polymer complexes formed using a liquid form of PACE that is synthesized with a low hydrophobic monomer content. We built on previous studies that had found that PACE end group compositions had a significant impact on properties such as nucleic acid encapsulation, cellular uptake, and endosomal escape. We identified an end group modified PACE polymer – PACE-E2, which terminates in a primary amine – as delivering a significantly greater siRNA-mediated knockdown of IL-15 in HUVECs relative to unmodified PACE and to PACE conjugated to other amine-containing end groups. To evaluate our delivery platform, we targeted IL-15 expression due to its role in activating cytotoxic and helper T cells in acute inflammation. We then blended PACE-E2 with a PEGylated PACE polymer terminating in a thiol-reactive maleimide group (PACE-PEG-Maleimide, or PP-Mal) to form polyplex delivery vehicles with the combined benefits of the E2 end group, the accessibility of reactive groups for thiol-based coupling, and the stability provided by PEGylation. We used this reactive group to couple a Fc-targeting monobody to the surface of PP-Mal/PACE-E2 polyplexes via a single C-terminal cysteine residue on the monobody (Mb). The Mb was engineered to bind the Fc portion of mouse IgG1, and can therefore act as an adapter to attach mIgG1 antibodies (Ab). In this study we coupled an anti-human-CD31 mAb to PACE polyplexes. We showed that polyplexes remained intact, with nucleic acid cargo still encapsulated, throughout the conjugation reactions. We found that blended PACE polyplexes conjugated to anti-CD31 antibodies via the Mb adapter were taken up by human endothelial cells at much higher and faster rates compared to unconjugated polyplexes of the same polymer composition. The same enhancement in uptake was not seen with polyplexes conjugated to an isotype-matched control Ab.

In Chapter 3 we developed a digital pathology application for color-based quantification of histologic specimens, and we used this app to quantify pathological features in transplant-declined human organs and in animal model tissues. In our work with transplant-declined human organs, we identified a need for a quantitative and high-throughput method for analyzing the large quantities of tissue biopsies that are generated in this area of research. As described in Section 1.1.3, organ transplantation creates a window of privileged access to the organ, and in particular to the endothelium which can be easily accessed via machine perfusion. Our application, DigiPath, was initially developed to assess the clearance of microvascular obstructions in human kidneys following *ex vivo* perfusion with a combination of tissue plasminogen activator (tPA) and plasminogen. We have also used this versatile tool to quantify vascular area in engineered grafts grown *in vitro* from cultured human endothelial cells.

4.2 Recommendations for Future Work

4.2.1 Functionalized PACE Polyplexes

In Chapter 2, we used PACE-E2 blended with PACE-PEG-Maleimide to formulate polyplex delivery vehicles that target delivery of nucleic acids to endothelial cells. In this study we made polymer blends with 10% and 30% PP-Mal content by weight. Following up on these data, it will be informative to make polyplexes using a broader range of PP-Mal content to find an optimal polymer blend that generates stable and effective polyplexes that efficiently bind to Mbs to generate targeted Ab-Mb-polyplexes. PEGylation has been shown in many settings to improve nanoparticle stability and stealth properties, but can affect cellular uptake in different ways depending on the vehicle, cargo, and application. *In vitro* we found that increasing PACE-PEG content reduced transfection efficiency, which was consistent with previous findings using unmodified PACE (**Figure 2.2**). However, this previous study showed that higher amounts of PACE-PEG improved transfection *in vivo*. For further investigation into the role of PEG in PP-Mal/PACE-2 polyplexes, we can also vary the length of the PEG groups (in this study, we used 5 kDa PEG or PEG-Mal).

In addition to the effects of PEG content on delivery, increasing PP-Mal theoretically increases the number of thiol reactive groups available for Mb conjugation. However we need to determine what effect the suface coverage of Mbs has on Ab binding and on the targeting performance of Ab-Mb-polyplexes. A thorough analysis of Mb and Ab conjugation to polyplexes of different polymer compositions is needed in order to reveal any potential relationships between PP-Mal content, Mb or Ab binding, and polyplex transfection efficiency.

The end group modified PACE polymers that we tested in HUVECs in this study were selected from a larger library based on their high transfection efficiencies and endosomal escape in an earlier screen of the polymer library in Expi293F cells [101]. They measured the encapsulation efficiency, cellular uptake, and endosomal escape of each polymer in the library, and found that endosomal escape efficiency was most highly correlated with transfection efficiency. The effect of Ab-Mb conjugation on intracellular trafficking and endosomal escape should be further investigated, as this is a critical factor in determining transfection efficiency.

Targeted delivery of Ab-Mb-polyplexes should be evaluated in a setting closer to *in vivo* conditions. In this study we performed preliminary experiments delivering PP-Mal/PACE-E2 Ab-Mb-polyplexes to human umbilical artery segments in an *ex vivo* isolated vessel perfusion loop system (IVPS) [123]. In these experiments we did not find any uptake improvement from CD31 targeting versus isotype control, and we observed high fluorescence signal in vessels perfused with unencapsulated dye-labeled DNA oligos. We hypothesize that the polyplexes may not have withstood the shear forces in the perfusion loop. The tubing is compressed where it runs through the peristaltic pump mechanism, and there are changes in tubing diameter where the loop connects to the vessel cartridge. In future experiments we plan to test this hypothesis by collecting samples from the perfusate to measure polyplex stability and release of cargo, and vary parameters such as flow rate or tubing size. We also plan to test polyplexes encapsulating fluorescently labeled mRNA to see if a larger cargo is less likely to leak out due to the forces in the loop. Alternatively, a microfluidic chamber can be used to measure the effects of flow rates on Ab-Mb-polyplex binding to cultured ECs.

As a further investigation of applications of Ab-Mb-polyplexes for targeting the endothelium, we can compare targeted polyplex uptake in different human EC cell lines (for example, dermal microvascular endothelial cells (HDMEC), or pulmonary microvascular endothelial cells (HPMEC)) using the same antibody. Because the Mb linker can be used to attach any compatible mouse IgG1 antibody, we can easily explore polyplex targeting to surface antigens that are differentially expressed in ECs due to organ-specific functions, inflammatory signaling, or other physiological conditions.

We identified PACE-E2 as the best-performing polymer for siRNA transfection in HUVECs among the end-group modified polymers that we tested. There is evidence that different end groups perform better for delivery to different cells or organs, through different administration routes, or with different nucleic acids. An end-group modified PACE, PACE-E14, was found to deliver the highest mRNA transfection in the lung by intratracheal delivery of reporter mRNA in mice [179]. PACE-PEG blends with unmodified PACE as well as PACE-E14 have been thoroughly investigated, however PP-Mal blends and Ab-Mb conjugation have not been explored. In upcoming experiments we will formulate PP-Mal/PACE-E14 polyplexes conjugated to antibodies targeting the lung epithelium, and deliver these to mice intratracheally.

4.2.2 Quantitative Histological Analysis

DigiPath was originally developed to aid in analyzing biopsy data from transplant-declined human organs, as described in Chapter 3. To make as much use of the donated tissue as possible, multiple biopsies of each organ are collected and cryo-banked. The quantities of tissues that arise from this practice necessitates a semi-automated workflow to process and make efficient use of the samples. A key component of this is an image analysis pipeline that can process images of different kinds. Since the development of DigiPath, additional image analysis modules (for example, masking or quantifying immunofluorescence microscopy images) that can plug in to a broader workflow are being developed.

One ongoing study is taking advantage of the high throughput capacity of DigiPath to systematically evaluate intra-organ and intra-biopsy variation in order to better understand how representative a single biopsy is of the health of a whole organ. Biopsies of different kinds (needle or wedge) from different regions of an organ are collected and disparate sections within each biopsy are stained. Features that identify injury to the organ such as fibrosis or ischemia are quantified and compared between biopsies, sections, and in some cases a paired organ from the same donor. DigiPath enables a quantitative assessment of these features using of a greater number of images and biopsies than could be processed manually.

The DigiPath app can be expanded upon to include morphology and texture in the identification of features. In its current format, there is an option to limit the range of sizes of features that will be detected. This enables some control over ruling out features that are either too big or too small to be relevant for quantifying the feature of interest. However, there is currently no option to have the program look for only features of a certain shape – for example, screening for round features will aid in quantifying lipid droplets, whereas screening for elongated structures will help identify microvasculature.

Appendix A

Supplementary Figures

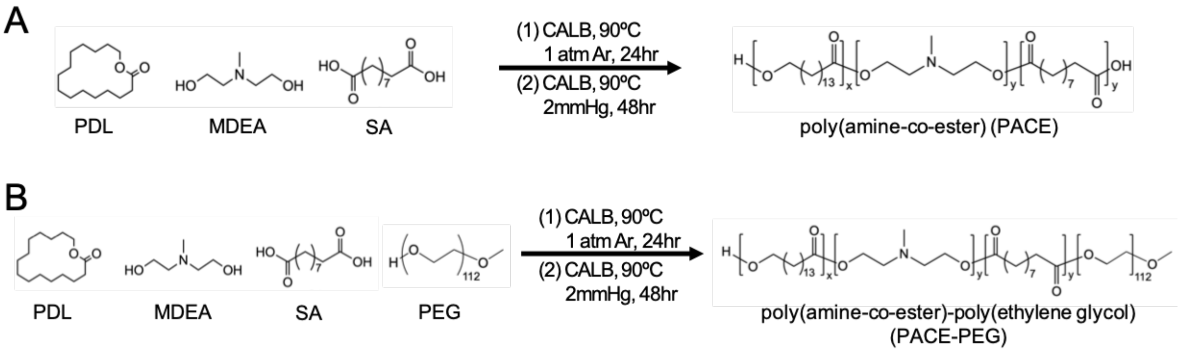

Figure A.1: Synthetic route for PACE **(A)** and PACE-PEG **(B)** by enzymatic copolymerization of pentadecanolide (PDL), methyldiethanolamine (MDEA), sebacic acid (SA), and poly(ethylene glycol) (PEG).

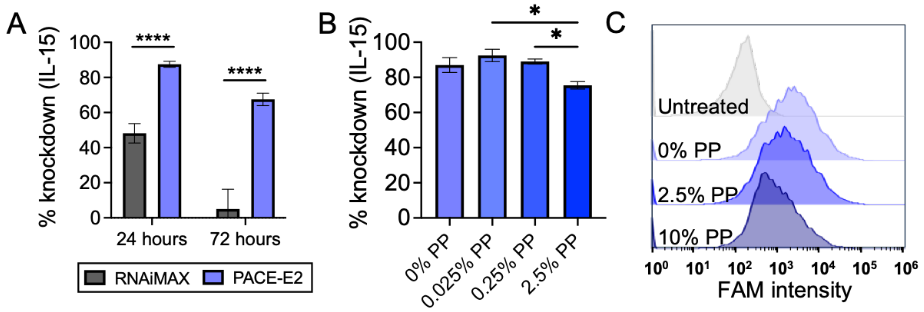

Figure A.2: **(A)** Knockdown of IL-15 in HUVEC is sustained for up to 72 hours with PACE-E2 siRNA polyplex delivery. **(B)** Addition of 2.5 wt% PACE-PEG significantly reduces cytotoxicity with minor decrease in transfection and knockdown efficiency **(C,D)**. *$p<0.05$; **$p<0.01$; ***$p<0.001$; ****$p<0.0001$.

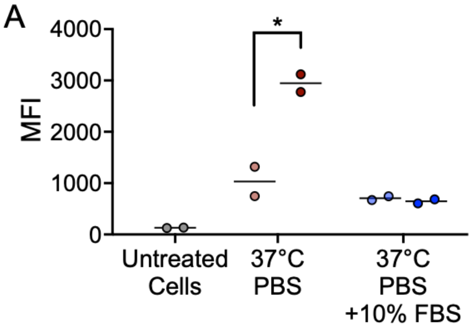

Figure A.3: **(A)** CD31-Mb-polyplexes stored at 1 mg/mL in PBS (dark red circles) maintained specific EC binding over Isotype-Mb-polyplexes stored at 1 mg/mL in PBS (light red circles) after 8 days of storage at 37C, shaking. When stored in PBS + 10% FBS (blue circles), CD31-Mb-polyplexes did not bind to ECs above nonspecific binding of Isotype-Mb-polyplexes. *$p<0.05$.

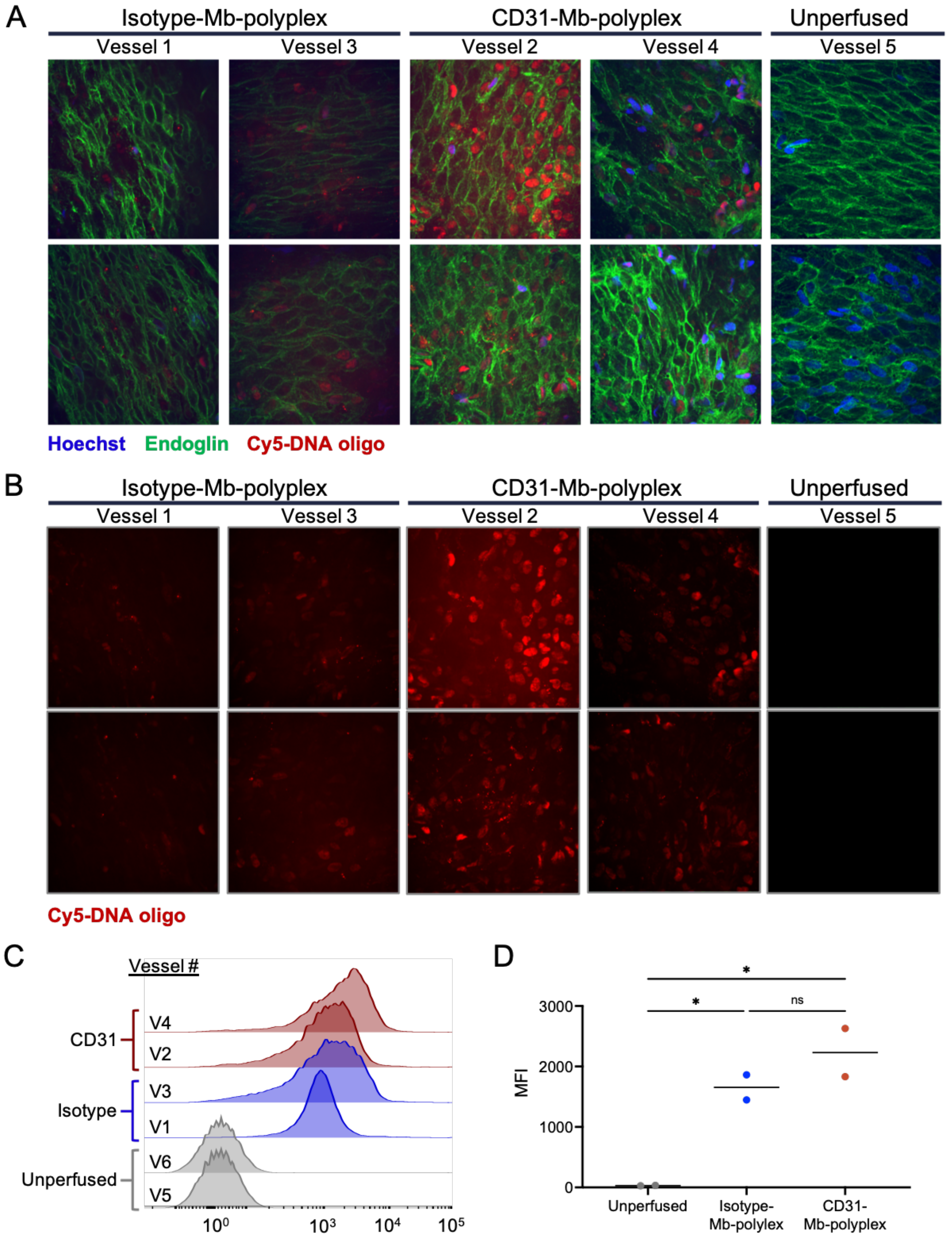

Figure A.4: **(A,B)** Confocal images of isolated human umbilical arteries following perfusion with Ab-Mb-polyplexes. An overlay of Hoechst nuclear stain (blue), endoglin (green), and Cy5 DNA oligo (red) is shown in **(A)**. **(B)** shows the isolated Cy5 channel of each field of view shown in **(A)**. **(C)** Flow cytometry histograms of Cy5 intensity in ECs (gated by endoglin-positive staining) isolated from vessels. Mean fluorescence intensity (MFI) is plotted in **(D)**. $*p<0.05$.

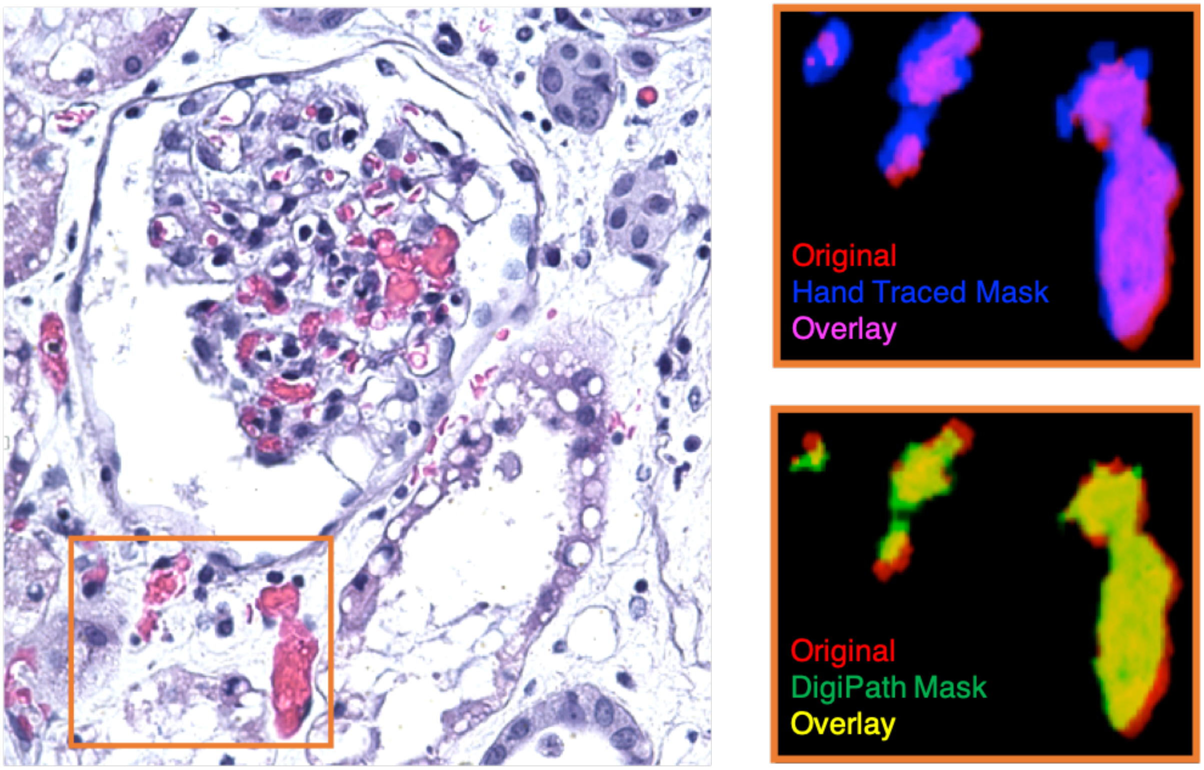

Figure A.5: Overlays of hand-traced (blue) or DigiPath (green) mask on original H&E obstruction (red). Orange box defines area of interest.

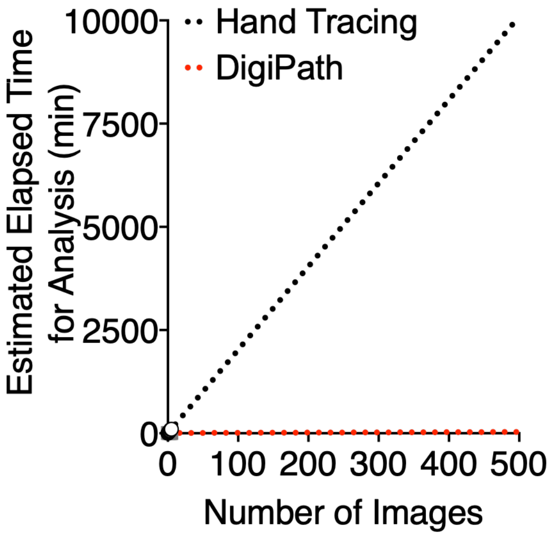

Figure A.6: Estimated extrapolation of analysis time for hand tracing (black line) or DigiPath (red line) in larger imaging sets of up to 500 images.

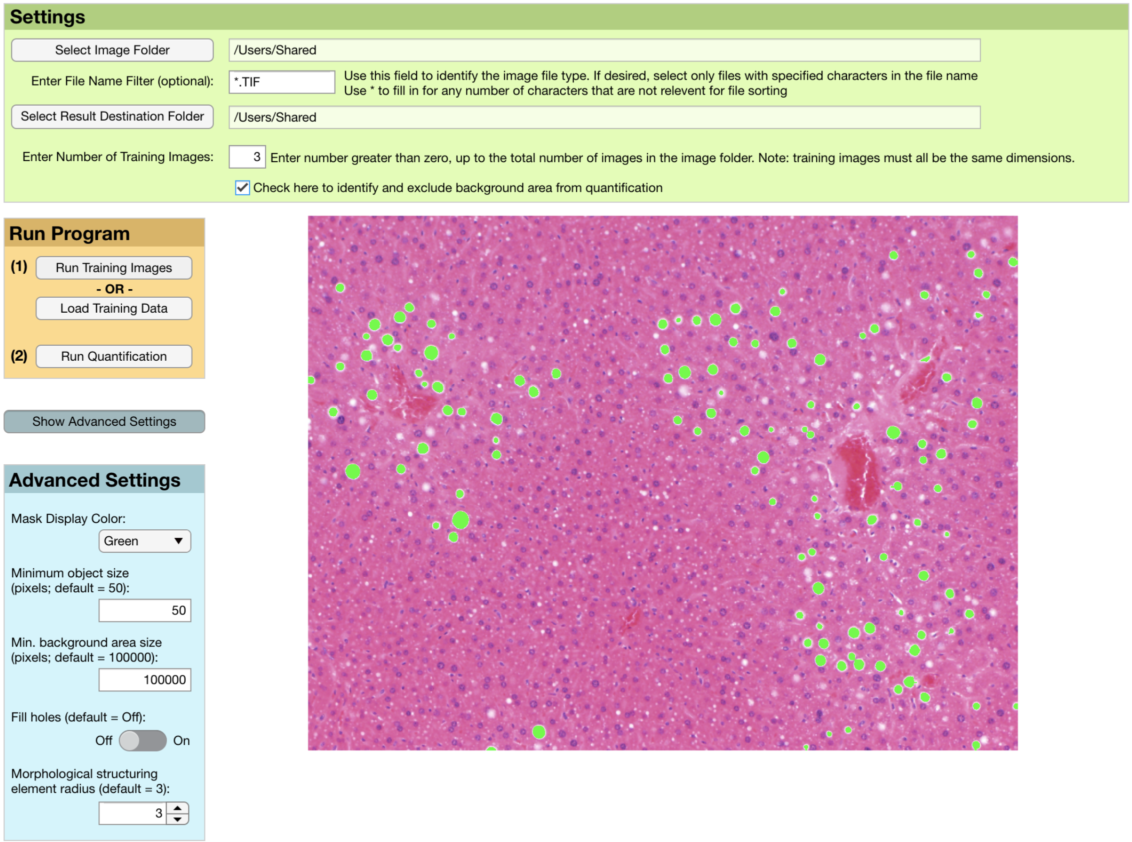

Settings

Select Image Folder: /Users/Shared

Enter File Name Filter (optional): *.TIF — Use this field to identify the image file type. If desired, select only files with specified characters in the file name
Use * to fill in for any number of characters that are not relevent for file sorting

Select Result Destination Folder: /Users/Shared

Enter Number of Training Images: 3 — Enter number greater than zero, up to the total number of images in the image folder. Note: training images must all be the same dimensions.

☑ Check here to identify and exclude background area from quantification

Run Program

(1) Run Training Images - OR - Load Training Data

(2) Run Quantification

Advanced Settings

Mask Display Color: Green

Minimum object size (pixels; default = 50): 50

Min. background area size (pixels; default = 100000): 100000

Fill holes (default = Off): Off On

Morphological structuring element radius (default = 3): 3

Figure A.7: The DigiPath app interface is organized into three sections. The 'Settings' section is used to select image folders and file types, assign the number of training images, and choose whether to exclude background areas. The 'Run Program' section is used to initiate the training portion of the workflow or load previously generated training data, and to run the automated quantification once the training portion is complete. The 'Avanced Settings' section (toggled to visible/invisible) is a panel with additional options to customize aspects of the analysis such as size thresholds, mask color, and morphological operations.

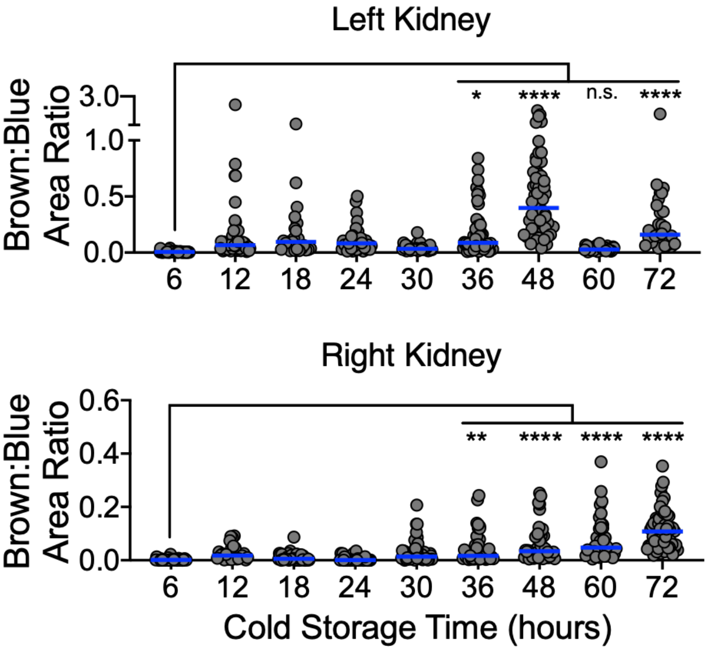

Figure A.8: Quantification of TUNEL staining in Left (top) and Right (bottom) kidneys during cold storage. The ratio of TUNEL-positive (brown) cell area to TUNEL-negative (blue) cell area is plotted. Each dot represents one field of view within the biopsy. Lines represent the median. **$p<0.01$; ***$p<0.001$; ****$p<0.0001$.

Bibliography

[1] W. C. Aird. Spatial and temporal dynamics of the endothelium. *J Thromb Haemost*, 3(7):1392–1406, Jul 2005.

[2] J. S. Pober and W. C. Sessa. Evolving functions of endothelial cells in inflammation. *Nat Rev Immunol*, 7(10):803–815, Oct 2007.

[3] M. K. Pugsley and R. Tabrizchi. The vascular system. An overview of structure and function. *J Pharmacol Toxicol Methods*, 44(2):333–340, 2000.

[4] W. C. Aird. Phenotypic heterogeneity of the endothelium: I. Structure, function, and mechanisms. *Circ Res*, 100(2):158–173, Feb 2007.

[5] M. Potente and T. Mäkinen. Vascular heterogeneity and specialization in development and disease. *Nat Rev Mol Cell Biol*, 18(8):477–494, 08 2017.

[6] N. Ricard, S. Bailly, C. Guignabert, and M. Simons. The quiescent endothelium: signalling pathways regulating organ-specific endothelial normalcy. *Nat Rev Cardiol*, 18(8):565–580, 08 2021.

[7] J. Andrade, C. Shi, A. S. H. Costa, J. Choi, J. Kim, A. Doddaballapur, T. Sugino, Y. T. Ong, M. Castro, B. Zimmermann, M. Kaulich, S. Guenther, K. Wilhelm, Y. Kubota, T. Braun, G. Y. Koh, A. R. Grosso, C. Frezza, and M. Potente. Control of endothelial quiescence by FOXO-regulated metabolites. *Nat Cell Biol*, 23(4):413–423, 04 2021.

[8] C. Sturtzel. Endothelial Cells. *Adv Exp Med Biol*, 1003:71–91, 2017.

[9] K. Neubauer and B. Zieger. Endothelial cells and coagulation. *Cell Tissue Res*, May 2021.

[10] P. A. Cahill and E. M. Redmond. Vascular endothelium - Gatekeeper of vessel health. *Atherosclerosis*, 248:97–109, May 2016.

[11] H. G. Augustin and G. Y. Koh. Organotypic vasculature: From descriptive heterogeneity to functional pathophysiology. *Science*, 357(6353), 08 2017.

[12] P. M. Glassman, J. W. Myerson, L. T. Ferguson, R. Y. Kiseleva, V. V. Shuvaev, J. S. Brenner, and V. R. Muzykantov. Targeting drug delivery in the vascular system: Focus on endothelium. *Adv Drug Deliv Rev*, 157:96–117, 2020.

[13] H. Uwamori, Y. Ono, T. Yamashita, K. Arai, and R. Sudo. Comparison of organ-specific endothelial cells in terms of microvascular formation and endothelial barrier functions. *Microvasc Res*, 122:60–70, 03 2019.

[14] T. M. McIntyre, S. M. Prescott, A. S. Weyrich, and G. A. Zimmerman. Cell-cell interactions: leukocyte-endothelial interactions. *Curr Opin Hematol*, 10(2):150–158, Mar 2003.

[15] S. W. Hunt, E. S. Harris, S. A. Kellermann, and Y. Shimizu. T-lymphocyte interactions with endothelium and extracellular matrix. *Crit Rev Oral Biol Med*, 7(1):59–86, 1996.

[16] T. Kambayashi and T. M. Laufer. Atypical MHC class II-expressing antigen-presenting cells: can anything replace a dendritic cell? *Nat Rev Immunol*, 14(11):719–730, Nov 2014.

[17] S. J. Cleary, N. Kwaan, J. J. Tian, D. R. Calabrese, B. Mallavia, M. Magnen, J. R. Greenland, A. Urisman, J. P. Singer, S. R. Hays, J. Kukreja, A. M. Hay, H. L. Howie, P. Toy, C. A. Lowell, C. N. Morrell, J. C. Zimring, and M. R. Looney. Complement activation on endothelium initiates antibody-mediated acute lung injury. *J Clin Invest*, 130(11):5909–5923, 11 2020.

[18] J. S. Pober, J. Merola, R. Liu, and T. D. Manes. Antigen Presentation by Vascular Cells. *Front Immunol*, 8:1907, 2017.

[19] J. Merola, M. Reschke, R. W. Pierce, L. Qin, S. Spindler, T. Baltazar, T. D. Manes, F. Lopez-Giraldez, G. Li, L. G. Bracaglia, C. Xie, N. Kirkiles-Smith, W. M. Saltzman, G. T. Tietjen, G. Tellides, and J. S. Pober. Progenitor-derived human endothelial cells evade alloimmunity by CRISPR/Cas9-mediated complete ablation of MHC expression. *JCI Insight*, 4(20), 10 2019.

[20] P. Abrahimi, R. Liu, and J. S. Pober. Blood Vessels in Allotransplantation. *Am J Transplant*, 15(7):1748–1754, Jul 2015.

[21] D. Vestweber. How leukocytes cross the vascular endothelium. *Nat Rev Immunol*, 15(11):692–704, Nov 2015.

[22] A. M. Ring, J. X. Lin, D. Feng, S. Mitra, M. Rickert, G. R. Bowman, V. S. Pande, P. Li, I. Moraga, R. Spolski, E. Ozkan, W. J. Leonard, and K. C. Garcia. Mechanistic and structural insight into the functional dichotomy between IL-2 and IL-15. *Nat Immunol*, 13(12):1187–1195, Dec 2012.

[23] S. W. Stonier and K. S. Schluns. Trans-presentation: a novel mechanism regulating IL-15 delivery and responses. *Immunol Lett*, 127(2):85–92, Jan 2010.

[24] J. C. Nolz and M. J. Richer. T cell longevity and effector functions by IL-15. *Mol Immunol*, 117:180–188, 01 2020.

[25] C. B. Xie, B. Jiang, L. Qin, G. Tellides, N. C. Kirkiles-Smith, D. Jane-Wit, and J. S. Pober. Complement-activated interferon--primed human endothelium transpresents interleukin-15 to CD8+ T cells. *J Clin Invest*, 130(7):3437–3452, 07 2020.

[26] M. Patidar, N. Yadav, and S. K. Dalai. Interleukin 15: A key cytokine for immunotherapy. *Cytokine Growth Factor Rev*, 31:49–59, 10 2016.

[27] D. E. Stewart, V. C. Garcia, J. D. Rosendale, D. K. Klassen, and B. J. Carrico. Diagnosing the Decades-Long Rise in the Deceased Donor Kidney Discard Rate in the United States. *Transplantation*, 101(3):575–587, 03 2017.

[28] R. A. Wolfe, E. C. Roys, and R. M. Merion. Trends in organ donation and transplantation in the United States, 1999-2008. *Am J Transplant*, 10(4 Pt 2):961–972, Apr 2010.

[29] A. Stephan. Organ Shortage: Can We Decrease the Demand? *Exp Clin Transplant*, 15(Suppl 1):6–9, Feb 2017.

[30] M. Cooper, R. Formica, J. Friedewald, R. Hirose, K. O'Connor, S. Mohan, J. Schold, D. Axelrod, and S. Pastan. Report of National Kidney Foundation Consensus Conference to Decrease Kidney Discards. *Clin Transplant*, 33(1):e13419, 01 2019.

[31] J. R. DiRito, S. A. Hosgood, M. Reschke, C. Albert, L. G. Bracaglia, J. R. Ferdinand, B. J. Stewart, C. M. Edwards, A. G. Vaish, S. Thiru, D. C. Mulligan, D. J. Haakinson, M. R. Clatworthy, W. M. Saltzman, J. S. Pober, M. L. Nicholson, and G. T. Tietjen. Lysis of cold-storage-induced microvascular obstructions for ex vivo revitalization of marginal human kidneys. *Am J Transplant*, 21(1):161–173, 01 2021.

[32] M. Reschke, J. R. DiRito, D. Stern, W. Day, N. Plebanek, M. Harris, S. A. Hosgood, M. L. Nicholson, D. J. Haakinson, X. Zhang, W. Z. Mehal, X. Ouyang, J. S. Pober, W. M. Saltzman, and G. T. Tietjen. A digital pathology tool for quantification of color features in histologic specimens. *Bioeng Transl Med*, 7(1):e10242, Jan 2022.

[33] F. A. Auger, L. Gibot, and D. Lacroix. The pivotal role of vascularization in tissue engineering. *Annu Rev Biomed Eng*, 15:177–200, 2013.

[34] S. Pashneh-Tala, S. MacNeil, and F. Claeyssens. The Tissue-Engineered Vascular Graft-Past, Present, and Future. *Tissue Eng Part B Rev*, 22(1):68–100, Feb 2016.

[35] S. W. Cho, F. Yang, S. M. Son, H. J. Park, J. J. Green, S. Bogatyrev, Y. Mei, S. Park, R. Langer, and D. G. Anderson. Therapeutic angiogenesis using genetically engineered human endothelial cells. *J Control Release*, 160(3):515–524, Jun 2012.

[36] M. A. Skylar-Scott, S. G. M. Uzel, L. L. Nam, J. H. Ahrens, R. L. Truby, S. Damaraju, and J. A. Lewis. Biomanufacturing of organ-specific tissues with high cellular density and embedded vascular channels. *Sci Adv*, 5(9):eaaw2459, 09 2019.

[37] S. Lee, E. S. Sani, A. R. Spencer, Y. Guan, A. S. Weiss, and N. Annabi. Human-Recombinant-Elastin-Based Bioinks for 3D Bioprinting of Vascularized Soft Tissues. *Adv Mater*, 32(45):e2003915, Nov 2020.

[38] F. E. Freeman, P. Pitacco, L. H. A. van Dommelen, J. Nulty, D. C. Browe, J. Y. Shin, E. Alsberg, and D. J. Kelly. 3D bioprinting spatiotemporally defined patterns of growth factors to tightly control tissue regeneration. *Sci Adv*, 6(33):eabb5093, Aug 2020.

[39] L. H. Solis, Y. Ayala, S. Portillo, A. Varela-Ramirez, R. Aguilera, and T. Boland. Thermal inkjet bioprinting triggers the activation of the VEGF pathway in human microvascular endothelial cells in vitro. *Biofabrication*, 11(4):045005, 07 2019.

[40] W. Song, A. Chiu, L. H. Wang, R. E. Schwartz, B. Li, N. Bouklas, D. T. Bowers, D. An, S. H. Cheong, J. A. Flanders, Y. Pardo, Q. Liu, X. Wang, V. K. Lee, G. Dai, and M. Ma. Engineering transferrable microvascular meshes for subcutaneous islet transplantation. *Nat Commun*, 10(1):4602, 10 2019.

[41] X. Dong, J. Gao, Y. Su, and Z. Wang. Nanomedicine for Ischemic Stroke. *Int J Mol Sci*, 21(20), Oct 2020.

[42] A. R. Cantelmo, L. C. Conradi, A. Brajic, J. Goveia, J. Kalucka, A. Pircher, P. Chaturvedi, J. Hol, B. Thienpont, L. A. Teuwen, S. Schoors, B. Boeckx, J. Vriens, A. Kuchnio, K. Veys, B. Cruys, L. Finotto, L. Treps, T. E. Stav-Noraas, F. Bifari, P. Stapor, I. Decimo, K. Kampen, K. De Bock, G. Haraldsen, L. Schoonjans, T. Rabelink, G. Eelen, B. Ghesquière, J. Rehman, D. Lambrechts, A. B. Malik, M. Dewerchin, and P. Carmeliet. Inhibition of the Glycolytic Activator PFKFB3 in Endothelium Induces Tumor Vessel Normalization, Impairs Metastasis, and Improves Chemotherapy. *Cancer Cell*, 30(6):968–985, Dec 2016.

[43] A. Duro-Castano, E. Gallon, C. Decker, and M. J. Vicent. Modulating angiogenesis with integrin-targeted nanomedicines. *Adv Drug Deliv Rev*, 119:101–119, 09 2017.

[44] S. Seaman, Z. Zhu, S. Saha, X. M. Zhang, M. Y. Yang, M. B. Hilton, K. Morris, C. Szot, H. Morris, D. A. Swing, L. Tessarollo, S. W. Smith, S. Degrado, D. Borkin, N. Jain, J. Scheiermann, Y. Feng, Y. Wang, J. Li, D. Welsch, G. DeCrescenzo, A. Chaudhary, E. Zudaire, K. D. Klarmann, J. R. Keller, D. S. Dimitrov, and B. St Croix. Eradication of Tumors through Simultaneous Ablation of CD276/B7-H3-Positive Tumor Cells and Tumor Vasculature. *Cancer Cell*, 31(4):501–515, 04 2017.

[45] G. Preissler, F. Loehe, I. V. Huff, U. Ebersberger, V. V. Shuvaev, I. Bittmann, I. Hermanns, J. C. Kirkpatrick, K. Fischer, M. E. Eichhorn, H. Winter, K. W. Jauch, S. M. Albelda, V. R. Muzykantov, and R. Wiewrodt. Targeted endothelial delivery of nanosized catalase immunoconjugates protects lung grafts donated after cardiac death. *Transplantation*, 92(4):380–387, Aug 2011.

[46] A. Wilson, W. Zhou, H. C. Champion, S. Alber, Z. L. Tang, S. Kennel, S. Watkins, L. Huang, B. Pitt, and S. Li. Targeted delivery of oligodeoxynucleotides to mouse lung endothelial cells in vitro and in vivo. *Mol Ther*, 12(3):510–518, Sep 2005.

[47] R. Kuruba, A. Wilson, X. Gao, and S. Li. Targeted delivery of nucleic-acid-based therapeutics to the pulmonary circulation. *AAPS J*, 11(1):23–30, Mar 2009.

[48] L. A. Teuwen, V. Geldhof, A. Pasut, and P. Carmeliet. COVID-19: the vasculature unleashed. *Nat Rev Immunol*, 20(7):389–391, 07 2020.

[49] T. Suvorava and W. Kaesemeyer. Targeting the Vascular Endothelium in the Treatment of COVID-19. *J Cardiovasc Pharmacol*, 77(1):1–3, 01 2021.

[50] Q. Qiao, X. Liu, T. Yang, K. Cui, L. Kong, C. Yang, and Z. Zhang. Nanomedicine for acute respiratory distress syndrome: The latest application, targeting strategy, and rational design. *Acta Pharm Sin B*, 11(10):3060–3091, Oct 2021.

[51] Z. Varga, A. J. Flammer, P. Steiger, M. Haberecker, R. Andermatt, A. S. Zinkernagel, M. R. Mehra, R. A. Schuepbach, F. Ruschitzka, and H. Moch. Endothelial cell infection and endotheliitis in COVID-19. *Lancet*, 395(10234):1417–1418, 05 2020.

[52] J. Ai, W. Hong, M. Wu, and X. Wei. Pulmonary vascular system: A vulnerable target for COVID-19. *MedComm (2020)*, Oct 2021.

[53] H. Deng, T. X. Tang, D. Chen, L. S. Tang, X. P. Yang, and Z. H. Tang. Endothelial Dysfunction and SARS-CoV-2 Infection: Association and Therapeutic Strategies. *Pathogens*, 10(5), May 2021.

[54] J. M. O'Sullivan, D. M. Gonagle, S. E. Ward, R. J. S. Preston, and J. S. O'Donnell. Endothelial cells orchestrate COVID-19 coagulopathy. *Lancet Haematol*, 7(8):e553–e555, 08 2020.

[55] G. Goshua, A. B. Pine, M. L. Meizlish, C. H. Chang, H. Zhang, P. Bahel, A. Baluha, N. Bar, R. D. Bona, A. J. Burns, C. S. Dela Cruz, A. Dumont, S. Halene, J. Hwa, J. Koff, H. Menninger, N. Neparidze, C. Price, J. M. Siner, C. Tormey, H. M. Rinder, H. J. Chun, and A. I. Lee. Endotheliopathy in COVID-19-associated coagulopathy: evidence from a single-centre, cross-sectional study. *Lancet Haematol*, 7(8):e575–e582, Aug 2020.

[56] M. Ackermann, S. E. Verleden, M. Kuehnel, A. Haverich, T. Welte, F. Laenger, A. Vanstapel, C. Werlein, H. Stark, A. Tzankov, W. W. Li, V. W. Li, S. J. Mentzer, and D. Jonigk. Pulmonary Vascular Endothelialitis, Thrombosis, and Angiogenesis in Covid-19. *N Engl J Med*, 383(2):120–128, 07 2020.

[57] J. Xie, Z. Shen, Y. Anraku, K. Kataoka, and X. Chen. Nanomaterial-based blood-brain-barrier (BBB) crossing strategies. *Biomaterials*, 224:119491, 12 2019.

[58] D. Male and R. Gromnicova. Nanocarriers for Delivery of Oligonucleotides to the CNS. *Int J Mol Sci*, 23(2), Jan 2022.

[59] S. Veszelka, M. Mészáros, G. Porkoláb, A. Szecskó, N. Kondor, G. Ferenc, T. F. Polgár, G. Katona, Z. Kóta, L. Kelemen, T. Páli, J. P. Vigh, F. R. Walter, S. Bolognin, J. C. Schwamborn, J. S. Jan, and M. A. Deli. A Triple Combination of Targeting Ligands Increases the Penetration of Nanoparticles across a Blood-Brain Barrier Culture Model. *Pharmaceutics*, 14(1), Dec 2021.

[60] K. Kucharz, K. Kristensen, K. B. Johnsen, M. A. Lund, M. Lønstrup, T. Moos, T. L. Andresen, and M. J. Lauritzen. Post-capillary venules are the key locus for transcytosis-mediated brain delivery of therapeutic nanoparticles. *Nat Commun*, 12(1):4121, 07 2021.

[61] R. L. Manthe, M. Loeck, T. Bhowmick, M. Solomon, and S. Muro. Intertwined mechanisms define transport of anti-ICAM nanocarriers across the endothelium and brain delivery of a therapeutic enzyme. *J Control Release*, 324:181–193, 08 2020.

[62] J. K. Saucier-Sawyer, Y. Deng, Y. E. Seo, C. J. Cheng, J. Zhang, E. Quijano, and W. M. Saltzman. Systemic delivery of blood-brain barrier-targeted polymeric nanoparticles enhances delivery to brain tissue. *J Drug Target*, 23(7-8):736–749, 2015.

[63] S. T. Crooke, B. F. Baker, R. M. Crooke, and X. H. Liang. Antisense technology: an overview and prospectus. *Nat Rev Drug Discov*, 20(6):427–453, 06 2021.

[64] M. Giacca. *Gene Therapy.* Springer Milan, 2011.

[65] S. M. Elbashir, J. Harborth, W. Lendeckel, A. Yalcin, K. Weber, and T. Tuschl. Duplexes of 21-nucleotide RNAs mediate RNA interference in cultured mammalian cells. *Nature*, 411(6836):494–498, May 2001.

[66] J. C. Burnett and J. J. Rossi. RNA-based therapeutics: current progress and future prospects. *Chem Biol*, 19(1):60–71, Jan 2012.

[67] T. Coelho, D. Adams, A. Silva, P. Lozeron, P. N. Hawkins, T. Mant, J. Perez, J. Chiesa, S. Warrington, E. Tranter, M. Munisamy, R. Falzone, J. Harrop, J. Cehelsky, B. R. Bettencourt, M. Geissler, J. S. Butler, A. Sehgal, R. E. Meyers, Q. Chen, T. Borland, R. M. Hutabarat, V. A. Clausen, R. Alvarez, K. Fitzgerald, C. Gamba-Vitalo, S. V. Nochur, A. K. Vaishnaw, D. W. Sah, J. A. Gollob, and O. B. Suhr. Safety and efficacy of RNAi therapy for transthyretin amyloidosis. *N Engl J Med*, 369(9):819–829, Aug 2013.

[68] C. Lorenzer, M. Dirin, A. M. Winkler, V. Baumann, and J. Winkler. Going beyond the liver: progress and challenges of targeted delivery of siRNA therapeutics. *J Control Release*, 203:1–15, Apr 2015.

[69] A. Fire, S. Xu, M. K. Montgomery, S. A. Kostas, S. E. Driver, and C. C. Mello. Potent and specific genetic interference by double-stranded RNA in Caenorhabditis elegans. *Nature*, 391(6669):806–811, Feb 1998.

[70] M. M. Zhang, R. Bahal, T. P. Rasmussen, J. E. Manautou, and X. B. Zhong. The growth of siRNA-based therapeutics: Updated clinical studies. *Biochem Pharmacol*, 189:114432, 07 2021.

[71] C. F. Bennett. Therapeutic Antisense Oligonucleotides Are Coming of Age. *Annu Rev Med*, 70:307–321, 01 2019.

[72] K. Gavrilov and W. M. Saltzman. Therapeutic siRNA: principles, challenges, and strategies. *Yale J Biol Med*, 85(2):187–200, Jun 2012.

[73] K. A. Whitehead, R. Langer, and D. G. Anderson. Knocking down barriers: advances in siRNA delivery. *Nat Rev Drug Discov*, 8(2):129–138, Feb 2009.

[74] J. M. Kułdo, S. A. Ásgeirsdóttir, P. J. Zwiers, A. R. Bellu, M. G. Rots, J. A. Schalk, K. I. Ogawara, C. Trautwein, B. Banas, H. J. Haisma, G. Molema, and J. A. Kamps. Targeted adenovirus mediated inhibition of NF-B-dependent inflammatory gene expression in endothelial cells in vitro and in vivo. *J Control Release*, 166(1):57–65, Feb 2013.

[75] K. Kusumoto, H. Akita, T. Ishitsuka, Y. Matsumoto, T. Nomoto, R. Furukawa, A. El-Sayed, H. Hatakeyama, K. Kajimoto, Y. Yamada, K. Kataoka, and H. Harashima. Lipid envelope-type nanoparticle incorporating a multifunctional peptide for systemic siRNA delivery to the pulmonary endothelium. *ACS Nano*, 7(9):7534–7541, Sep 2013.

[76] P. H. Tan, M. Manunta, N. Ardjomand, S. A. Xue, D. F. Larkin, D. O. Haskard, K. M. Taylor, and A. J. George. Antibody targeted gene transfer to endothelium. *J Gene Med*, 5(4):311–323, Apr 2003.

[77] Y. Zhao and L. Huang. Lipid nanoparticles for gene delivery. *Adv Genet*, 88:13–36, 2014.

[78] M. A. Subhan and V. P. Torchilin. Efficient nanocarriers of siRNA therapeutics for cancer treatment. *Transl Res*, 214:62–91, 12 2019.

[79] J. Chen, K. Wang, J. Wu, H. Tian, and X. Chen. Polycations for Gene Delivery: Dilemmas and Solutions. *Bioconjug Chem*, 30(2):338–349, 02 2019.

[80] S. P. Schwendeman. Moving RNA interference beyond the liver. *J Control Release*, 313:161–162, 11 2019.

[81] J. E. Zuckerman, C. H. Choi, H. Han, and M. E. Davis. Polycation-siRNA nanoparticles can disassemble at the kidney glomerular basement membrane. *Proc Natl Acad Sci U S A*, 109(8):3137–3142, Feb 2012.

[82] Y. Tang, Z. Zeng, X. He, T. Wang, X. Ning, and X. Feng. SiRNA Crosslinked Nanoparticles for the Treatment of Inflammation-induced Liver Injury. *Adv Sci (Weinh)*, 4(2):1600228, Feb 2017.

[83] J. Cui, A. S. Piotrowski-Daspit, J. Zhang, M. Shao, L. G. Bracaglia, T. Utsumi, Y. E. Seo, J. DiRito, E. Song, C. Wu, A. Inada, G. T. Tietjen, J. S. Pober, Y. Iwakiri, and W. M. Saltzman. Poly(amine-co-ester) nanoparticles for effective Nogo-B knockdown in the liver. *J Control Release*, 304:259–267, 06 2019.

[84] Z. Fu, X. Zhang, X. Zhou, U. Ur-Rehman, M. Yu, H. Liang, H. Guo, X. Guo, Y. Kong, Y. Su, Y. Ye, X. Hu, W. Cheng, J. Wu, Y. Wang, Y. Gu, S. F. Lu, D. Wu, K. Zen, J. Li, C. Yan, C. Y. Zhang, and X. Chen. In vivo self-assembled small RNAs as a new generation of RNAi therapeutics. *Cell Res*, 31(6):631–648, 06 2021.

[85] K. A. Woodrow, Y. Cu, C. J. Booth, J. K. Saucier-Sawyer, M. J. Wood, and W. M. Saltzman. Intravaginal gene silencing using biodegradable polymer nanoparticles densely loaded with small-interfering RNA. *Nat Mater*, 8(6):526–533, Jun 2009.

[86] E. Blanco, H. Shen, and M. Ferrari. Principles of nanoparticle design for overcoming biological barriers to drug delivery. *Nat Biotechnol*, 33(9):941–951, Sep 2015.

[87] N. D. Donahue, H. Acar, and S. Wilhelm. Concepts of nanoparticle cellular uptake, intracellular trafficking, and kinetics in nanomedicine. *Adv Drug Deliv Rev*, 143:68–96, 03 2019.

[88] R. Pasqualini, B. J. Moeller, and W. Arap. Leveraging molecular heterogeneity of the vascular endothelium for targeted drug delivery and imaging. *Semin Thromb Hemost*, 36(3):343–351, Apr 2010.

[89] A. S. Piotrowski-Daspit, A. C. Kauffman, L. G. Bracaglia, and W. M. Saltzman. Polymeric vehicles for nucleic acid delivery. *Adv Drug Deliv Rev*, 156:119–132, 2020.

[90] C. K. Chen, P. K. Huang, W. C. Law, C. H. Chu, N. T. Chen, and L. W. Lo. Biodegradable Polymers for Gene-Delivery Applications. *Int J Nanomedicine*, 15:2131–2150, 2020.

[91] E. W. Kavanagh and J. J. Green. Toward Gene Transfer Nanoparticles as Therapeutics. *Adv Healthc Mater*, page e2102145, Jan 2022.

[92] A. Vaheri and J. S. Pagano. Infectious poliovirus RNA: a sensitive method of assay. *Virology*, 27(3):434–436, Nov 1965.

[93] E. Fröhlich. The role of surface charge in cellular uptake and cytotoxicity of medical nanoparticles. *Int J Nanomedicine*, 7:5577–5591, 2012.

[94] M. Piest and J. F. J. Engbersen. Effects of charge density and hydrophobicity of poly(amido amine)s for non-viral gene delivery. *J Control Release*, 148(1):83–90, Nov 2010.

[95] J. J. Green, J. Shi, E. Chiu, E. S. Leshchiner, R. Langer, and D. G. Anderson. Biodegradable polymeric vectors for gene delivery to human endothelial cells. *Bioconjug Chem*, 17(5):1162–1169, 2006.

[96] J. Kim, A. C. Mirando, A. S. Popel, and J. J. Green. Gene delivery nanoparticles to modulate angiogenesis. *Adv Drug Deliv Rev*, 119:20–43, 09 2017.

[97] J. J. Green, R. Langer, and D. G. Anderson. A combinatorial polymer library approach yields insight into nonviral gene delivery. *Acc Chem Res*, 41(6):749–759, Jun 2008.

[98] R. B. Shmueli, J. C. Sunshine, Z. Xu, E. J. Duh, and J. J. Green. Gene delivery nanoparticles specific for human microvasculature and macrovasculature. *Nanomedicine*, 8(7):1200–1207, Oct 2012.

[99] J. Zhou, J. Liu, C. J. Cheng, T. R. Patel, C. E. Weller, J. M. Piepmeier, Z. Jiang, and W. M. Saltzman. Biodegradable poly(amine-co-ester) terpolymers for targeted gene delivery. *Nat Mater*, 11(1):82–90, Dec 2011.

[100] A. C. Kauffman, A. S. Piotrowski-Daspit, K. H. Nakazawa, Y. Jiang, A. Datye, and W. M. Saltzman. Tunability of Biodegradable Poly(amine- co-ester) Polymers for Customized Nucleic Acid Delivery and Other Biomedical Applications. *Biomacromolecules*, 19(9):3861–3873, 09 2018.

[101] Y. Jiang, Q. Lu, Y. Wang, E. Xu, A. Ho, P. Singh, Y. Wang, Z. Jiang, F. Yang, G. T. Tietjen, P. Cresswell, and W. M. Saltzman. Quantitating Endosomal Escape of a Library of Polymers for mRNA Delivery. *Nano Lett*, 20(2):1117–1123, 02 2020.

[102] B. Y. Kim, J. T. Rutka, and W. C. Chan. Nanomedicine. *N Engl J Med*, 363(25):2434–2443, Dec 2010.

[103] Y. Barenholz. Doxil®–the first FDA-approved nano-drug: lessons learned. *J Control Release*, 160(2):117–134, Jun 2012.

[104] L. Woythe, N. B. Tito, and L. Albertazzi. A quantitative view on multivalent nanomedicine targeting. *Adv Drug Deliv Rev*, 169:1–21, 02 2021.

[105] P. Kolhar, A. C. Anselmo, V. Gupta, K. Pant, B. Prabhakarpandian, E. Ruoslahti, and S. Mitragotri. Using shape effects to target antibody-coated nanoparticles to lung and brain endothelium. *Proc Natl Acad Sci U S A*, 110(26):10753–10758, Jun 2013.

[106] F. Danhier. To exploit the tumor microenvironment: Since the EPR effect fails in the clinic, what is the future of nanomedicine? *J Control Release*, 244(Pt A):108–121, 12 2016.

[107] G. T. Tietjen, L. G. Bracaglia, W. M. Saltzman, and J. S. Pober. Focus on Fundamentals: Achieving Effective Nanoparticle Targeting. *Trends Mol Med*, 24(7):598–606, 07 2018.

[108] A. J. Sivaram, A. Wardiana, C. B. Howard, S. M. Mahler, and K. J. Thurecht. Recent Advances in the Generation of Antibody-Nanomaterial Conjugates. *Adv Healthc Mater*, 7(1), 01 2018.

[109] H. Ragelle, S. Colombo, V. Pourcelle, K. Vanvarenberg, G. Vandermeulen, C. Bouzin, J. Marchand-Brynaert, O. Feron, C. Foged, and V. Préat. Intracellular siRNA delivery dynamics of integrin-targeted, PEGylated chitosan-poly(ethylene imine) hybrid nanoparticles: A mechanistic insight. *J Control Release*, 211:1–9, Aug 2015.

[110] P. Vader, B. J. Crielaard, S. M. van Dommelen, R. van der Meel, G. Storm, and R. M. Schiffelers. Targeted delivery of small interfering RNA to angiogenic endothelial cells with liposome-polycation-DNA particles. *J Control Release*, 160(2):211–216, Jun 2012.

[111] H. Y. Nam, J. Kim, S. W. Kim, and D. A. Bull. Cell targeting peptide conjugation to siRNA polyplexes for effective gene silencing in cardiomyocytes. *Mol Pharm*, 9(5):1302–1309, May 2012.

[112] J. Devalliere, W. G. Chang, J. W. Andrejecsk, P. Abrahimi, C. J. Cheng, D. Jane-wit, W. M. Saltzman, and J. S. Pober. Sustained delivery of proangiogenic microRNA-132 by nanoparticle transfection improves endothelial cell transplantation. *FASEB J*, 28(2):908–922, Feb 2014.

[113] L. Lin, M. Cai, S. Deng, W. Huang, J. Huang, X. Huang, M. Huang, Y. Wang, X. Shuai, and K. Zhu. Amelioration of cirrhotic portal hypertension by targeted cyclooxygenase-1 siRNA delivery to liver sinusoidal endothelium with polyethylenimine grafted hyaluronic acid. *Nanomedicine*, 13(7):2329–2339, Oct 2017.

[114] J. Cheng, B. A. Teply, I. Sherifi, J. Sung, G. Luther, F. X. Gu, E. Levy-Nissenbaum, A. F. Radovic-Moreno, R. Langer, and O. C. Farokhzad. Formulation of functionalized PLGA-PEG nanoparticles for in vivo targeted drug delivery. *Biomaterials*, 28(5):869–876, Feb 2007.

[115] M. Liu, L. Wang, Y. Lo, S. C. Shiu, A. B. Kinghorn, and J. A. Tanner. Aptamer-Enabled Nanomaterials for Therapeutics, Drug Targeting and Imaging. *Cells*, 11(1), 01 2022.

[116] A. M. Chacko, J. Han, C. F. Greineder, B. J. Zern, J. L. Mikitsh, M. Nayak, D. Menon, I. H. Johnston, M. Poncz, D. M. Eckmann, P. F. Davies, and V. R. Muzykantov. Collaborative Enhancement of Endothelial Targeting of Nanocarriers by Modulating Platelet-Endothelial Cell Adhesion Molecule-1/CD31 Epitope Engagement. *ACS Nano*, 9(7):6785–6793, Jul 2015.

[117] A. Parodi, N. Quattrocchi, A. L. van de Ven, C. Chiappini, M. Evangelopoulos, J. O. Martinez, B. S. Brown, S. Z. Khaled, I. K. Yazdi, M. V. Enzo, L. Isenhart, M. Ferrari, and E. Tasciotti. Synthetic nanoparticles functionalized with biomimetic leukocyte membranes possess cell-like functions. *Nat Nanotechnol*, 8(1):61–68, Jan 2013.

[118] J. Gao, D. Chu, and Z. Wang. Cell membrane-formed nanovesicles for disease-targeted delivery. *J Control Release*, 224:208–216, Feb 2016.

[119] A. Koide, C. W. Bailey, X. Huang, and S. Koide. The fibronectin type III domain as a scaffold for novel binding proteins. *J Mol Biol*, 284(4):1141–1151, Dec 1998.

[120] F. Sha, G. Salzman, A. Gupta, and S. Koide. Monobodies and other synthetic binding proteins for expanding protein science. *Protein Sci*, 26(5):910–924, 05 2017.

[121] H. Parhiz, V. V. Shuvaev, N. Pardi, M. Khoshnejad, R. Y. Kiseleva, J. S. Brenner, T. Uhler, S. Tuyishime, B. L. Mui, Y. K. Tam, T. D. Madden, M. J. Hope, D. Weissman, and V. R. Muzykantov. PECAM-1 directed re-targeting of exogenous mRNA providing two orders of magnitude enhancement of vascular delivery and expression in lungs independent of apolipoprotein E-mediated uptake. *J Control Release*, 291:106–115, 12 2018.

[122] Y. Y. Chen, A. M. Syed, P. MacMillan, J. V. Rocheleau, and W. C. W. Chan. Flow Rate Affects Nanoparticle Uptake into Endothelial Cells. *Adv Mater*, 32(24):e1906274, Jun 2020.

[123] T. Lysyy, L. G. Bracaglia, L. Qin, C. Albert, J. S. Pober, G. Tellides, W. M. Saltzman, and G. T. Tietjen. Ex vivo isolated human vessel perfusion system for the design and assessment of nanomedicines targeted to the endothelium. *Bioeng Transl Med*, 5(2):e10154, May 2020.

[124] G. T. Tietjen, S. A. Hosgood, J. DiRito, J. Cui, D. Deep, E. Song, J. R. Kraehling, A. S. Piotrowski-Daspit, N. C. Kirkiles-Smith, R. Al-Lamki, S. Thiru, J. A. Bradley, K. Saeb-Parsy, J. R. Bradley, M. L. Nicholson, W. M. Saltzman, and J. S. Pober. Nanoparticle targeting to the endothelium during normothermic machine perfusion of human kidneys. *Sci Transl Med*, 9(418), 11 2017.

[125] J. Di, F. Xie, and Y. Xu. When liposomes met antibodies: Drug delivery and beyond. *Adv Drug Deliv Rev*, 154-155:151–162, 2020.

[126] R. Y. Kiseleva, P. G. Glassman, K. M. LeForte, L. R. Walsh, C. H. Villa, V. V. Shuvaev, J. W. Myerson, P. A. Aprelev, O. A. Marcos-Contreras, V. R. Muzykantov, and C. F. Greineder. Bivalent engagement of endothelial surface antigens is critical to prolonged surface targeting and protein delivery in vivo. *FASEB J*, 34(9):11577–11593, 09 2020.

[127] E. Simone, B. S. Ding, and V. Muzykantov. Targeted delivery of therapeutics to endothelium. *Cell Tissue Res*, 335(1):283–300, Jan 2009.

[128] S. Gholizadeh, J. A. A. M. Kamps, W. E. Hennink, and R. J. Kok. PLGA-PEG nanoparticles for targeted delivery of the mTOR/PI3kinase inhibitor dactolisib to inflamed endothelium. *Int J Pharm*, 548(2):747–758, Sep 2018.

[129] S. Theoharis, U. Krueger, P. H. Tan, D. O. Haskard, M. Weber, and A. J. George. Targeting gene delivery to activated vascular endothelium using anti E/P-Selectin antibody linked to PAMAM dendrimers. *J Immunol Methods*, 343(2):79–90, Apr 2009.

[130] S. A. Asgeirsdóttir, E. G. Talman, I. A. de Graaf, J. A. Kamps, S. C. Satchell, P. W. Mathieson, M. H. Ruiters, and G. Molema. Targeted transfection increases siRNA uptake and gene silencing of primary endothelial cells in vitro–a quantitative study. *J Control Release*, 141(2):241–251, Jan 2010.

[131] S. Ma, X. Y. Tian, Y. Zhang, C. Mu, H. Shen, J. Bismuth, H. J. Pownall, Y. Huang, and W. T. Wong. E-selectin-targeting delivery of microRNAs by microparticles ameliorates endothelial inflammation and atherosclerosis. *Sci Rep*, 6:22910, Mar 2016.

[132] J. A. Palma-Chavez, K. Fuentes, B. E. Applegate, J. A. Jo, and P. Charoenphol. Development and Characterization of PLGA-Based Multistage Delivery System for Enhanced Payload Delivery to Targeted Vascular Endothelium. *Macromol Biosci*, 21(3):e2000377, 03 2021.

[133] G. A. Koning, R. M. Schiffelers, M. H. Wauben, R. J. Kok, E. Mastrobattista, G. Molema, T. L. ten Hagen, and G. Storm. Targeting of angiogenic endothelial cells at sites of inflammation by dexamethasone phosphate-containing RGD peptide liposomes inhibits experimental arthritis. *Arthritis Rheum*, 54(4):1198–1208, Apr 2006.

[134] O. A. Marcos-Contreras, C. F. Greineder, R. Y. Kiseleva, H. Parhiz, L. R. Walsh, V. Zuluaga-Ramirez, J. W. Myerson, E. D. Hood, C. H. Villa, I. Tombacz, N. Pardi, A. Seliga, B. L. Mui, Y. K. Tam, P. M. Glassman, V. V. Shuvaev, J. Nong, J. S. Brenner, M. Khoshnejad, T. Madden, D. Weissmann, Y. Persidsky, and V. R. Muzykantov. Selective targeting of nanomedicine to inflamed cerebral vasculature to enhance the blood-brain barrier. *Proc Natl Acad Sci U S A*, 117(7):3405–3414, 02 2020.

[135] C. Qi, Y. Jin, Y. Chen, W. Li, Y. Li, K. Liang, Y. Li, Y. Zhang, and Y. Du. TGase-mediated cell membrane modification and targeted cell delivery to inflammatory endothelium. *Biomaterials*, 269:120276, 02 2021.

[136] M. K. Khang, A. E. Kuriakose, T. Nguyen, C. M. Co, J. Zhou, T. T. D. Truong, K. T. Nguyen, and L. Tang. Enhanced Endothelial Cell Delivery for Repairing Injured Endothelium via Pretargeting Approach and Bioorthogonal Chemistry. *ACS Biomater Sci Eng*, 6(12):6831–6841, 12 2020.

[137] J. Huang, P. Guo, and M. A. Moses. Rationally Designed Antibody Drug Conjugates Targeting the Breast Cancer-Associated Endothelium. *ACS Biomater Sci Eng*, 6(5):2563–2569, 05 2020.

[138] P. Lertkiatmongkol, D. Liao, H. Mei, Y. Hu, and P. J. Newman. Endothelial functions of platelet/endothelial cell adhesion molecule-1 (CD31). *Curr Opin Hematol*, 23(3):253–259, May 2016.

[139] P. J. Newman. The role of PECAM-1 in vascular cell biology. *Ann N Y Acad Sci*, 714:165–174, Apr 1994.

[140] V. Fehring, U. Schaeper, K. Ahrens, A. Santel, O. Keil, M. Eisermann, K. Giese, and J. Kaufmann. Delivery of therapeutic siRNA to the lung endothelium via novel Lipoplex formulation DACC. *Mol Ther*, 22(4):811–820, Apr 2014.

[141] J. Cui, L. Qin, J. Zhang, P. Abrahimi, H. Li, G. Li, G. T. Tietjen, G. Tellides, J. S. Pober, and W. Mark Saltzman. Ex vivo pretreatment of human vessels with siRNA

nanoparticles provides protein silencing in endothelial cells. *Nat Commun*, 8(1):191, 08 2017.

[142] M. K. Grun, A. Suberi, K. Shin, T. Lee, V. Gomerdinger, Z. M. Moscato, A. S. Piotrowski-Daspit, and W. M. Saltzman. PEGylation of poly(amine-co-ester) polyplexes for tunable gene delivery. *Biomaterials*, 272:120780, 05 2021.

[143] Y. Jiang, A. Gaudin, J. Zhang, T. Agarwal, E. Song, A. C. Kauffman, G. T. Tietjen, Y. Wang, Z. Jiang, C. J. Cheng, and W. M. Saltzman. A ”top-down” approach to actuate poly(amine-co-ester) terpolymers for potent and safe mRNA delivery. *Biomaterials*, 176:122–130, 09 2018.

[144] H. Petersen, P. M. Fechner, A. L. Martin, K. Kunath, S. Stolnik, C. J. Roberts, D. Fischer, M. C. Davies, and T. Kissel. Polyethylenimine-graft-poly(ethylene glycol) copolymers: influence of copolymer block structure on DNA complexation and biological activities as gene delivery system. *Bioconjug Chem*, 13(4):845–854, 2002.

[145] S. J. Sung, S. H. Min, K. Y. Cho, S. Lee, Y. J. Min, Y. I. Yeom, and J. K. Park. Effect of polyethylene glycol on gene delivery of polyethylenimine. *Biol Pharm Bull*, 26(4):492–500, Apr 2003.

[146] X. Zhang, W. Tang, Z. Yang, X. Luo, H. Luo, D. Gao, Y. Chen, Q. Jiang, J. Liu, and Z. Jiang. PEGylated poly(amine-co-ester) micelles as biodegradable non-viral gene vectors with enhanced stability, reduced toxicity and higher in vivo transfection efficacy. *J Mater Chem B*, 2(25):4034–4044, Jul 2014.

[147] A. Koide, J. Wojcik, R. N. Gilbreth, R. J. Hoey, and S. Koide. Teaching an old scaffold new tricks: monobodies constructed using alternative surfaces of the FN3 scaffold. *J Mol Biol*, 415(2):393–405, Jan 2012.

[148] F. Sha, E. B. Gencer, S. Georgeon, A. Koide, N. Yasui, S. Koide, and O. Hantschel. Dissection of the BCR-ABL signaling network using highly specific monobody inhibitors to the SHP2 SH2 domains. *Proc Natl Acad Sci U S A*, 110(37):14924–14929, Sep 2013.

[149] C. Albert, L. Bracaglia, A. Koide, J. DiRito, T. Lysyy, C. Edwards, J. Grundler, K. Zhou, E. Denbaum, G. Ketavarapu, T. Hattori, J. Langford, A. Feizi, D. Haakinson, J.S. Pober, W.M. Saltzman, S. Koide, and G.T. Tietjen. *Manuscript in review.*

[150] A. B. Farris, I. Moghe, S. Wu, J. Hogan, L. D. Cornell, M. P. Alexander, J. Kers, A. J. Demetris, R. M. Levenson, J. Tomaszewski, L. Barisoni, Y. Yagi, and K. Solez. Banff digital pathology working group: Going digital in transplant pathology. *Am J Transplant*, 20(9):2392–2399, 2020.

[151] H. Liapis, J. P. Gaut, C. Klein, S. Bagnasco, E. Kraus, 3rd Farris, A. B., E. Honsova, A. Perkowska-Ptasinska, D. David, J. Goldberg, M. Smith, M. Mengel, M. Haas, S. Seshan, K. L. Pegas, T. Horwedel, Y. Paliwa, X. Gao, D. Landsittel, P. Randhawa, and Group Banff Working. Banff histopathological consensus criteria for preimplantation kidney biopsies. *Am J Transplant*, 17(1):140–150, 2017.

[152] A. Loupy, M. Haas, K. Solez, L. Racusen, D. Glotz, D. Seron, B. J. Nankivell, R. B. Colvin, M. Afrouzian, E. Akalin, N. Alachkar, S. Bagnasco, J. U. Becker, L. Cornell, C. Drachenberg, D. Dragun, H. de Kort, I. W. Gibson, E. S. Kraus, C. Lefaucheur, C. Legendre, H. Liapis, T. Muthukumar, V. Nickeleit, B. Orandi, W. Park, M. Rabant, P. Randhawa, E. F. Reed, C. Roufosse, S. V. Seshan, B. Sis, H. K. Singh, C. Schinstock, A. Tambur, A. Zeevi, and M. Mengel. The banff 2015 kidney meeting report: Current challenges in rejection classification and prospects for adopting molecular pathology. *Am J Transplant*, 17(1):28–41, 2017.

[153] D. K. Meyerholz and A. P. Beck. Principles and approaches for reproducible scoring of tissue stains in research. *Lab Invest*, 98(7):844–855, 2018.

[154] C. R. Taylor and R. M. Levenson. Quantification of immunohistochemistry–issues concerning methods, utility and semiquantitative assessment ii. *Histopathology*, 49(4):411–24, 2006.

[155] A. M. El-Badry, S. Breitenstein, W. Jochum, K. Washington, V. Paradis, L. Rubbia-Brandt, M. A. Puhan, K. Slankamenac, R. Graf, and P. A. Clavien. Assessment of hepatic steatosis by expert pathologists: the end of a gold standard. *Ann Surg*, 250(5):691–7, 2009.

[156] H. Yersiz, C. Lee, F. M. Kaldas, J. C. Hong, A. Rana, G. T. Schnickel, J. A. Wertheim, A. Zarrinpar, V. G. Agopian, J. Gornbein, B. V. Naini, C. R. Lassman, R. W. Busuttil, and H. Petrowsky. Assessment of hepatic steatosis by transplant surgeon and expert pathologist: a prospective, double-blind evaluation of 201 donor livers. *Liver Transpl*, 19(4):437–49, 2013.

[157] John O. O. Ayorinde, Dominic M. Summers, Laura Pankhurst, Emma Laing, Alison J. Deary, Karla Hemming, Edward C. F. Wilson, Victoria Bardsley, Desley A. Neil, and Gavin J. Pettigrew. Preimplantation trial of histopathology in renal allografts (pithia): a stepped-wedge cluster randomised controlled trial protocol. *BMJ Open*, 9(1), 2019.

[158] J. H. Hong, D. H. Kim, I. J. Rhyu, Y. C. Kye, and H. H. Ahn. A simple morphometric analysis method for dermal microstructure using color thresholding and moments. *Skin Research and Technology*, 26(1):132–136, 2020.

[159] S. J. Johnson and F. R. Walker. Strategies to improve quantitative assessment of immunohistochemical and immunofluorescent labelling. *Sci Rep*, 5:10607, 2015.

[160] K. Prasad and G. K. Prabhu. Image analysis tools for evaluation of microscopic views of immunohistochemically stained specimen in medical research-a review. *J Med Syst*, 36(4):2621–31, 2012.

[161] F. Bukenya, C. Nerissa, S. Serres, M. C. Pardon, and L. Bai. An automated method for segmentation and quantification of blood vessels in histology images. *Microvasc Res*, 128:103928, 2020.

[162] R. Fu, X. Ma, Z. Bian, and J. Ma. Digital separation of diaminobenzidine-stained tissues via an automatic color-filtering for immunohistochemical quantification. *Biomed Opt Express*, 6(2):544–58, 2015.

[163] Y. Murakami, T. Abe, A. Hashiguchi, M. Yamaguchi, A. Saito, and M. Sakamoto. Color correction for automatic fibrosis quantification in liver biopsy specimens. *J Pathol Inform*, 4:36, 2013.

[164] S. A. Hosgood, E. Thompson, T. Moore, C. H. Wilson, and M. L. Nicholson. Normothermic machine perfusion for the assessment and transplantation of declined human kidneys from donation after circulatory death donors. *Br J Surg*, 105(4):388–394, 2018.

[165] P. Zhao, S. N. Han, S. Arumugam, M. N. Yousaf, Y. Qin, J. X. Jiang, N. J. Torok, Y. Chen, M. S. Mankash, J. Liu, J. Li, Y. Iwakiri, and X. Ouyang. Digoxin improves steatohepatitis with differential involvement of liver cell subsets in mice through inhibition of pkm2 transactivation. *Am J Physiol Gastrointest Liver Physiol*, 317(4):G387–G397, 2019.

[166] W. J. Youden. Index for rating diagnostic tests. *Cancer*, (3):32–35, 1950.

[167] Tom Fawcett. An introduction to roc analysis. *Pattern Recognition Letters*, 27(8):861–874, 2006.

[168] D. Chicco and G. Jurman. The advantages of the matthews correlation coefficient (mcc) over f1 score and accuracy in binary classification evaluation. *BMC Genomics*, 21(1):6, 2020.

[169] D. Chicco, N. Totsch, and G. Jurman. The matthews correlation coefficient (mcc) is more reliable than balanced accuracy, bookmaker informedness, and markedness in two-class confusion matrix evaluation. *BioData Min*, 14(1):13, 2021.

[170] B.W. Matthews. Comparison of the predicted and observed secondary structure of t4 phage lysozyme. *Biochimica et Biophysica Acta*, 405(2):442–451, 1975.

[171] P. A. Bautista, N. Hashimoto, and Y. Yagi. Color standardization in whole slide imaging using a color calibration slide. *J Pathol Inform*, 5(1):4, 2014.

[172] J. Schindelin, I. Arganda-Carreras, E. Frise, V. Kaynig, M. Longair, T. Pietzsch, S. Preibisch, C. Rueden, S. Saalfeld, B. Schmid, J. Y. Tinevez, D. J. White, V. Hartenstein, K. Eliceiri, P. Tomancak, and A. Cardona. Fiji: an open-source platform for biological-image analysis. *Nat Methods*, 9(7):676–82, 2012.

[173] J. Schindelin, C. T. Rueden, M. C. Hiner, and K. W. Eliceiri. The imagej ecosystem: An open platform for biomedical image analysis. *Mol Reprod Dev*, 82(7-8):518–29, 2015.

[174] C. A. Schneider, W. S. Rasband, and K. W. Eliceiri. Nih image to imagej: 25 years of image analysis. *Nat Methods*, 9(7):671–5, 2012.

[175] P. Bankhead, M. B. Loughrey, J. A. Fernandez, Y. Dombrowski, D. G. McArt, P. D. Dunne, S. McQuaid, R. T. Gray, L. J. Murray, H. G. Coleman, J. A. James, M. Salto-Tellez, and P. W. Hamilton. Qupath: Open source software for digital pathology image analysis. *Sci Rep*, 7(1):16878, 2017.

[176] P. Kankaanpaa, L. Paavolainen, S. Tiitta, M. Karjalainen, J. Paivarinne, J. Nieminen, V. Marjomaki, J. Heino, and D. J. White. Bioimagexd: an open, general-purpose and high-throughput image-processing platform. *Nat Methods*, 9(7):683–9, 2012.

[177] M. R. Lamprecht, D. M. Sabatini, and A. E. Carpenter. Cellprofiler: free, versatile software for automated biological image analysis. *Biotechniques*, 42(1):71–5, 2007.

[178] F. Piccinini, T. Balassa, A. Szkalisity, C. Molnar, L. Paavolainen, K. Kujala, K. Buzas, M. Sarazova, V. Pietiainen, U. Kutay, K. Smith, and P. Horvath. Advanced cell classifier: User-friendly machine-learning-based software for discovering phenotypes in high-content imaging data. *Cell Syst*, 4(6):651–655 e5, 2017.

[179] T. Mao, B. Israelow, A. Suberi, L. Zhou, M. Reschke, M.A. Peña Hernández, H. Dong, R.J. Homer, W.M. Saltzman, and A. Iwasaki. *Manuscript in review.*